University of Strathclyde
Department of Electronic and Electrical Engineering

Harvesting Energy from Electric Fields for Powering Wireless Sensors within Air-Insulated Substations

by
Minan Zhu

M.Eng. (Hons), MIET

A thesis presented in fulfillment of the requirements for the degree of Doctor of Philosophy

2018

Copyright Declaration

This thesis is the result of the author's original research. It has been composed by the author and has not been submitted for examination which has let to the award of a degree.

The copyright of this thesis belongs to the author under the terms of the United Kingdom Copyright Acts as qualified by University of Strathclyde Regulation 3.50. Due acknowledgement must always be made of the use of any material contained in, or derived from, this thesis.

Signed: Date:

Acknowledgements

The author would like to express his gratitude to National Grid (UK) plc for providing financial and technical support to this project. The patient guidance provided by Dr Martin Judd, former Professor of High Voltage Engineering at the University of Strathclyde, over the years is much appreciated. I would also like to express my gratitude to all the colleagues in the High Voltage Laboratory for their generous assistance.

Abstract

Aging equipment in the electricity grid requires close monitoring to ensure the safe operation of the network. The lack of reliable and cost effective ways for supplying power has hindered the large scale installation of wireless condition monitoring sensors in the electricity grid. Electric fields of elevated strength exist in high voltage plants, such as air-insulated substations. Advances in technology have been reducing the power consumption of wireless sensors. Harvesting energy from the electric fields could be a viable way of supplying power to the wireless sensors if the technical challenges can be overcome.

This study reports the progress in the field of energy harvesting, surveys the electric fields inside air-insulated substations, explains the physical phenomenon of charge induction inside electric fields in detail, investigates charge transfer techniques, proposes solutions to the technical challenges and presents the design and assembly of a demonstration unit. The successful operation of the demonstration unit shows that harvesting energy from the electric fields has the potential to enable large scale installation of wireless condition monitoring sensors in the electricity grid.

Research Outputs

- M. Zhu, M. D. Judd, P. J. Moore and R. Zhang, 'Energy Harvesting in Substations for Autonomous Sensing', poster and display at the Energy Harvesting Technologies Event organised by the Sensors and Instrumentation KTN, IET Savoy Place, London, UK, November 2008.

- M. Zhu, M. D. Judd, P. J. Moore, R. Zhang, 'Energy Harvesting Technique for Powering Autonomous Sensors within Substations', Proc. 1st International Conference on SUPERGEN, Nanjing, China, April 2009.

- M. Zhu, P. Baker, N. M. Roscoe, M. D. Judd and J. Fitch, 'Alternative Energy Sources for Autonomous Sensors in High Voltage Plant', Proc. 29th IEEE Electrical Insulation Conference, Montreal, Canada, June 2009.

- M. Zhu, P. Baker, N. M. Roscoe, M. D. Judd and J. Fitch, 'Energy Harvesting in Substations for Powering Autonomous Sensors', Proc. 3rd International Conference on Sensor Technologies and Applications, Athens, Greece, June 2009.

- M. Zhu and M. D. Judd, 'Energy Harvesting from Electric Fields in Substations for Powering Autonomous Sensors', Proc. 4th UHVnet Colloquium, Winchester, UK, January 2011.

- M. Zhu, N. M. Roscoe, M. D. Judd, 'Energy Harvesting from Electric and Magnetic Fields in Substations for Powering Autonomous Sensors', Winner of the Best Poster Award at EPSRC Energy Harvesting 2011, London, UK, February 2011.

List of Acronyms

EPSRC	Engineering and Physical Science Research Council
IEEE	Institute of Electrical and Electronics Engineers
IoP	Institute of Physics
PZT	Piezoelectric Lead Zirconate Titanate
PCB	Printed Circuit Board
TEG	Thermoelectric Generator
RF	Radio Frequency
RFID	Radio Frequency IDentification
FSPA	Folded Shorted Patch Antenna
MOS	Metal Oxide Semiconductor
MOSFET	Metal Oxide Semiconductor Field Effect Transistor
HV	High Voltage
ICP	Induced Charge Pulse
MEMS	Micro Electro Mechanical Systems
SCP	Switching Control Pulse
SSHI	Synchronised Switching Harvesting on Inductor
LED	Light Emitting Diode
MOSFET	Metal Oxide Semiconductor Field Effect Transistor
GDT	Gas Discharging Tube
LCD	Liquid Crystal Display

Contents

List of Figures

List of Tables

List of Equations

Chapter 1

Introduction

1.1 The field of energy harvesting

Interests in the field of energy harvesting, also known as energy scavenging, from both the academic community and industrial companies have been growing considerably. Energy harvesting, as described by an EPSRC-funded professional network, is a means of powering wireless electronic devices by scavenging low grade ambient energy sources and their conversion into useable electrical energy [1].

The term 'low grade' implies that the average output power from these ambient sources are substantially below the peak demand of a wireless sensor unless the harvesting device is impractically large. The gap between the peak demand of the load and the low average output of the energy source needs to be bridged in one way or another. These low grade energy sources are either a byproduct of the activity from a bigger system, such as vibrations from the rotating machinery, or simply a natural phenomenon, like the thermal gradient across an object due to temperature difference.

Maintaining the batteries of numerous wireless sensors that spread over a wide geographical area or are installed in difficult-to-access locations is very costly. The high cost associated with battery maintenance could make the use of wireless sensors uneconomical in many applications. In addition, the chemical composition of the battery also makes it undesirable to be used in certain circumstances.

Advances in technology have substantially decreased the power consumption of wireless sensors. Modern wireless sensors can be configured to enter into sleep

Table 1.1: Power consumption of modern wireless sensors at sleep mode [2].

Technology Platform	Communication Protocol	Sleep Mode Consumption
Bluetooth Low Energy	IEEE 802.15.1	2.6 μW
ZigBee	IEEE 802.15.4	13.8 μW
ANT	Proprietary	10.2 μW

mode, with little power being consumed, if they are neither processing nor transmitting data. Table 1.1 shows the sleep mode power consumptions of three popular low power sensor platforms [2].

If low grade energy source exists in the immediate vicinity of a wireless sensor node, harnessing the energy to power the sensor directly or charge up the battery can help to eliminate the requirement for battery maintenance. It will open the way to a large number of potential sensing applications which are currently too costly or impractical to implement.

The technical and commercial benefits that energy harvesting technologies can bring are attractive. However, there are a few challenges that need to be overcome. Commercially available sensing device, such as MICAz, uses the ZigBee standard. It has a maximum data transmission rate of 250 kB per second. The transmission time for small amount of data maybe very short. But its peak power consumption is in the region of a few tens of milliwatt [3]. As mentioned earlier in this section, the average power output from these ambient sources are substantially below the peak demand of commercially available wireless sensors. Finding a way to bridge this gap would require a lot of effort.

Furthermore, these energy sources are heavily influenced by the ambient environment and each one of them has its own characteristics. For example, the oscillating direction of one vibration source could be different from another. A mechanism that is designed to harvest energy from a particular source may not be suitable for another source.

1.2 Battery vs energy harvesting

It is generally agreed that primary battery is the most convenient and cost-effective solution for supplying power to a wireless sensor. An AA-size alkaline

battery has a volume of about 8.26 cm^3 and contains up to 3000 mAh (1.08×10^4 C) of electric charge. Despite the fact that its effective capacity at high current drain is much smaller than the theoretical limit, it is still able to supply a few tens of milliamperes of current for at least a few hours.

On the other hand, it has been anticipated that the lifespan of a wireless electronic device is only limited by the reliability of its components [4]. Energy harvesting devices have an average output power density in the region of a few microwatt per cubic centimeter (μW/cm^3). They are unable to meet the demand of power-intensive activities, but they could operate over a period of several years or even decades, lasting as long as the lifespan of the assets they are embedded into.

If a wireless sensor node is required to operate over a long period and/or in a location where the cost of battery maintenance is prohibitively high, energy harvesting device could help to meet, at least part of, the energy demand of the sensor. Energy harvesting devices and primary batteries are not in direct competition. On the contrary, they complement each other in many potential applications.

1.3 Motivation of the project

One of the major concerns for the electricity network operators is the aging infrastructure and equipments. Replacing these assets is not only expensive but also time consuming. It is widely anticipated that electricity consumption will increase over time as fossil fuels like gas and petrol are being replaced gradually by electrical power. In addition, more and more installed capacity from the distributed generation plants are being connected to the grid. Existing equipment in the electricity grid are likely to face more challenging operating conditions in the future.

Equipment failure can lead to power outage, which is very costly in many aspects. Monitoring the state of the aging equipment continuously will help the network operators to have a more accurate picture of the health of their assets. Extensive and accurate condition monitoring on the equipment requires more sensors to be installed.

There are currently two ways to supply energy to condition monitoring sensors, one is installing cable and the other is using a battery. Batteries have limited lifetime. The locations where condition monitoring sensors will be installed are often inconvenient to gain access regularly. Maintaining batteries for a large number of sensors would incur high labour cost and cause plenty of inconvenience to the safe operation of the electricity network.

Supplying energy through a cable is highly reliable. However, the cost of installing cables to a large number of sensors could be very high. The high cost of cabling means that condition monitoring sensors tend to be installed only at a few sites that are most critical to the operation of the electricity network. In addition, finding a suitable low voltage power source in substations can also be challenging despite the fact that large amount of energy is being transferred on high voltage overhead lines just a few metres away.

A reliable and cost effective way to power wireless sensors could be very attractive to the utility companies and other potential users. It would pave the way for large scale installation of wireless sensors in the electricity network.

Equipment in substations are surrounded by electromagnetic fields. Electrical currents, together with the magnetic fields they produce, could go through a considerable change in strength within a short period of time because of the fluctuation in load demand. On the other hand, the voltage level is carefully controlled to keep variation to minimum. This means the strength of the electric fields at a specific location is stable under normal operating conditions. The focus of this study is to investigate how to harvest the energy contained inside electric fields.

1.4 Overview of the thesis

This thesis presents the investigative work that has been carried out for the project. The major areas of research were concerned with how to efficiently harvest the energy that exists in the electric fields and bridge the gap between the demand of the application load and the output of the harvesting device. Here is a brief summary of each chapter:

Chapter 2 reviews the technologies and the progress that have been made in the

most active areas of energy harvesting.

Chapter 3 describes the work on characterising electric fields. It explores the physical phenomenon associated with the creation of electric fields and presents the field surveys that have been carried out in two separate air-insulated substations.

Chapter 4 is devoted to the topic of charge induction. It explains the fundamental science of electrification by electrostatic induction as well as investigates the relationship between the amount of charge that can be induced and the physical characteristics of the harvesting electrode.

Chapter 5 describes the work on how to mitigate the loading effect of a high impedance energy source. The objective is to maximise the amount of induced charge that can be transferred from the harvesting electrode to an energy storage device.

Chapter 6 describes the work on developing an energy buffer. The energy buffer manages the accumulation and discharging of energy on the energy storage device.

Chapter 7 shows the assembly and testing of a demonstration unit. Harvesting energy from the electric fields inside an air-insulated substation has been successfully demonstrated.

Chapter 8 summaries the major findings discovered from this study.

Chapter 9 discusses the improvement opportunities that are worthwhile to be pursued.

1.5 Summary of novel contributions

A few discoveries were made during the course of this study. To the best knowledge of the author, they have not been presented in any publicly available scientific publications prior to this thesis. The contributions are listed below:

- Measurements of the strength of the electric fields were taken at several

easy-to-access locations inside air-insulated substations with the objective of harvesting energy from the electric fields in mind. Those locations which are most suitable for installing energy harvesting devices have been identified.

- The preferred physical characteristics of the harvesting electrode have been identified. These characteristics do not compromise the safety of the electricity network while helping the harvesting electrode to induce the maximum amount of charge.

- The synchronised switching harvesting on inductor technique is found to be able to mitigate the loading effect of a high impedance source. This technique is particularly effective when the output waveform of the energy source has identifiable peaks and troughes.

- A generic energy buffer prototype, which could be configured to suit different applications, has been built and tested.

- Harvesting energy from the electric fields has been demonstrated in a 50 Hz high voltage air-insulated substation. The harvested energy has successfully powered a temperature sensor.

Bibliography

[1] The Energy Harvesting Network, Engineering and Physical Science Research Council (UK).

[2] A. Dementyev, S. Hodges, S. Taylor and J. Smith, Power Consumption Analysis of Bluetooth Low Energy, ZigBee and ANT Sensor Nodes in a Cyclic Sleep Scenario, *Proc. of IEEE International Wireless Symposium (IWS)*, Electronic ISBN: 978-1-4673-2141-9, April 2013, Beijing, China.

[3] MICAz datasheet, Wireless Sensor Network, ACEINNA Inc, Massachusetts, USA.

[4] J. Paradiso and T. Starner, Energy Scavenging for Mobile and Wireless Electronics, *IEEE Pervasive Computing*, pp. 18-27, January-March 2005.

Chapter 2

Energy harvesting technologies

2.1 Introduction

Advances in technology have drastically reduced the power consumption of modern wireless sensors. Wireless sensor platforms consume a few microwatt (μW), a few tens of microwatt and a few tens of milliwatt (mW) when it is in 'sleep', 'idle' and 'transmission' mode respectively [1].

One of the features of modern wireless sensors is that the duty cycle can be configured according to the amount of data that needs to be transmitted. Once the data has been transmitted, the sensor can stay in 'sleep' or 'idle' mode until the next energy intensive task. This feature helps to reduce the energy consumption. Energy harvesting technologies have the potential to meet the energy demand of a low power consumption wireless sensor [2, 3, 4, 5].

Renewable energy sources, such as wind and solar, have much higher energy density and/or longevity than the low grade ambient sources that associated with energy harvesting. They don't fit the energy harvesting definition and belong to a different field of research [6].

This chapter summaries the developments in the most active areas of energy harvesting, such as low level vibration, thermal gradient and radio frequency signals. Different publications often give different names, like transducer, generator and scavenger etc, to a device that is able to harvest energy from ambient sources. To avoid confusion, the term 'energy harvesting device' will be used throughout this thesis. In some passages, a shorter term 'harvesting device' is also used to

make the wording less cumbersome.

2.2 Low level vibration

Low level vibration is commonplace in daily life. When a person is walking, a few tens of milliwatt of energy will dissipate into the sole of the shoe with each step [7, 8]. Another example is the vibration from rotating machinery. The kinetic energy from low level vibration could be converted into electrical energy for practical use. There are three common transduction mechanisms: piezoelectric, electromagnetic and electrostatic motions [9, 10]. The energy density of these three types of harvesting devices is presented in Table 2.1.

Table 2.1: Summary of maximum energy density of three types of vibration harvesting devices [12].

Type	Energy Density (mJ/cm^3)	Test Condition
Piezoelectric	35.4	Resonant frequency vibration
Electromagnetic	24.8	Magnetic flux = 0.25 T
Electrostatic	4.0	Electric field = 3×10^4 kV/m

2.2.1 Piezoelectric transduction

Crystalline substances with asymmetric unit cells have the ability to convert mechanical energy into electrical energy [11]. Once external force is applied onto the piezoelectric element, the polarised unit cells will align into a pattern which generates an electrostatic potential between the two opposite surfaces on the same piece of piezoelectric element. This phenomenon is called the piezoelectric effect. One study reported that piezoelectric element can achieve maximum output density of 35.4 mJ/cm^3 when it is vibrating at its resonant frequency [12].

The most efficient piezoelectric material that has been discovered is lead zirconate titanate (PZT) [13]. However, material that contains lead is not suitable to be used in many products. The research work for producing lead-free piezoelectric materials with comparable efficiency is underway [14].

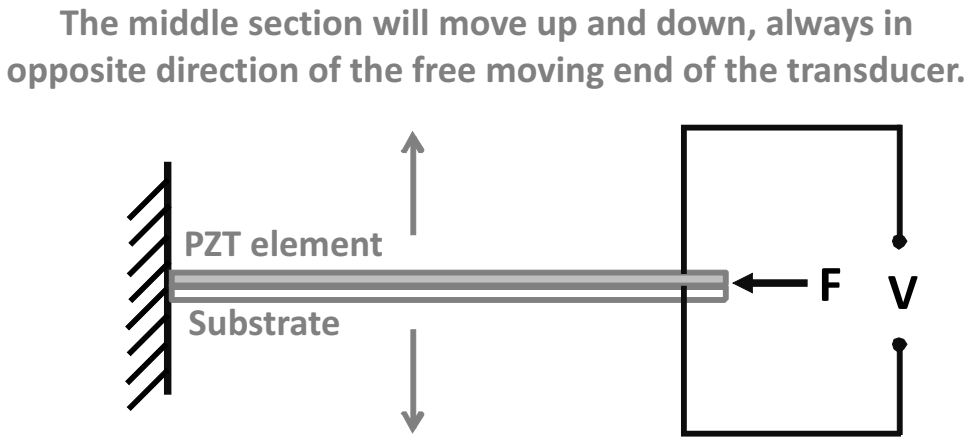

Figure 2.1: Cross section view of a unimorph piezoelectric material.

Piezoelectric film with only a single layer of active piezoelectric element is known as the unimorph form. Figure 2.1 shows a piece of unimorph piezoelectric film. A potential difference would be generated across the two different layers when this film experiences external force.

Piezoelectric film that have two layers of active piezoelectric element are known as the bimorph form. The composition of a piece of bimorph piezoelectric film is shown in Figure 2.2. It is approximately 0.5 mm thick. An insulation layer, labelled as the 'Neutral axis', is sandwiched between two piezoelectric elements. When the bimorph piezoelectric film is being bent, each piezoelectric element generates a potential difference between two opposite surfaces. Connecting the surfaces that have the same polarity across two piezoelectric elements could produce a higher output voltage than unimorph piezoelectric film.

There are two common modes of operation for piezoelectric films, commonly referred to as 31 mode and 33 mode. The first digit indicates the direction of movement of the piezoelectric film. The second digit indicates the direction of the mechanical force that is being applied onto the piezoelectric film. The grey rectangular block represents a piece of piezoelectric film in both Figure 2.3 and Figure 2.4. Figure 2.3 shows the 33 mode operation. Both the movement of the piezoelectric film and the mechanical force that is applying onto the film are along the vertical axis. The 31 mode operation is shown in Figure 2.4. The mechanical force is applied in a horizontally axial direction on the long side of the piezoelectric film while middle section/part of the film moves vertically.

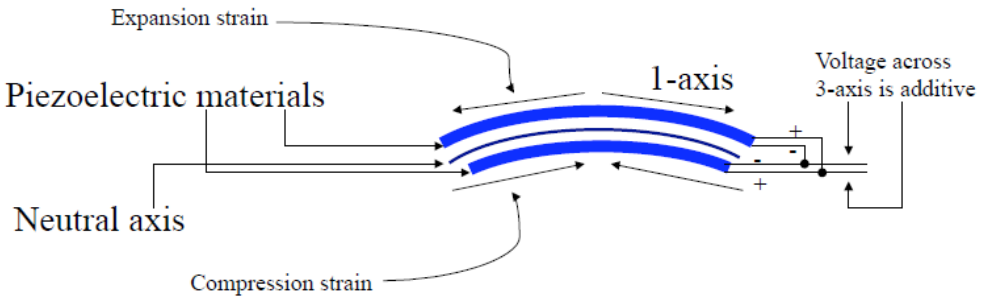

Figure 2.2: The potential difference generated by a piece of bimorph piezoelectric film when it is experiencing external force [7] © IEEE 2001.

When a piece of bimorph piezoelectric film, such as the one shown in Figure 2.2, was embedded into the heel of a trainer, it is capable of supplying 1.3 mW of power continuously if the person that wears the trainer is walking at a pace of 0.8 Hz (equivalent to 1.25 second per step) [7].

Piezoelectric materials can also been embedded into the floor to harness the energy from foot steps. One project installed floor pads that have been embedded with piezoelectric materials around several ticket gates in a busy commuter railway station. The total installation area is 6 m^2. All these floor pads are able to produce up to 10 kJ of energy, equivalent to an average power output of 115 mW, in one day [15]. Another project laid down 47 m^2 of piezoelectric-embedded floor tiles on the running path of a marathon event. 17 kJ ($\approx$ 4.7 kilowatt-hour) of energy was generated after the marathon finished [16, 17]. These studies prove that decent amount of energy can be generated if piezoelectric materials are placed in locations where there are plenty of vibration. Larger amount of energy could be harvested by increasing the density of the piezoelectric materials and/or expanding the installation area.

Many components within a large piece of electrical/mechanical equipment that vibrate frequently are vulnerable to degrading or even outright failure. The best practice in asset management is to monitor these components continuously. The energy released by the vibration could be harnessed to power sensors that are intended for monitoring the condition of the same piece of equipment.

Commercially available piezoelectric material has a thickness of less than one

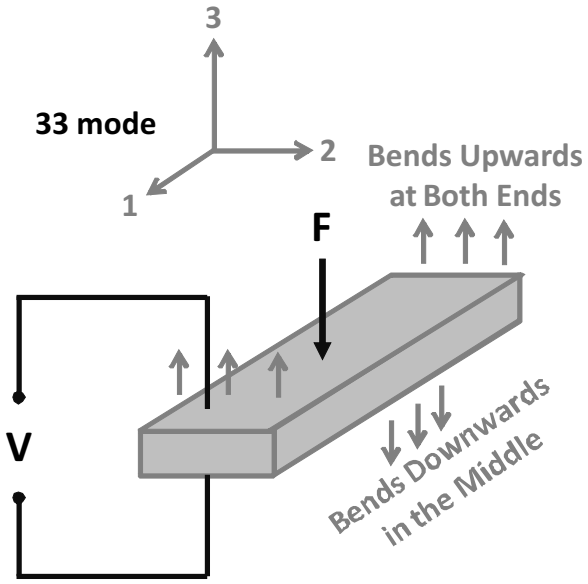

Figure 2.3: Piezoelectric film operates in 33 mode.

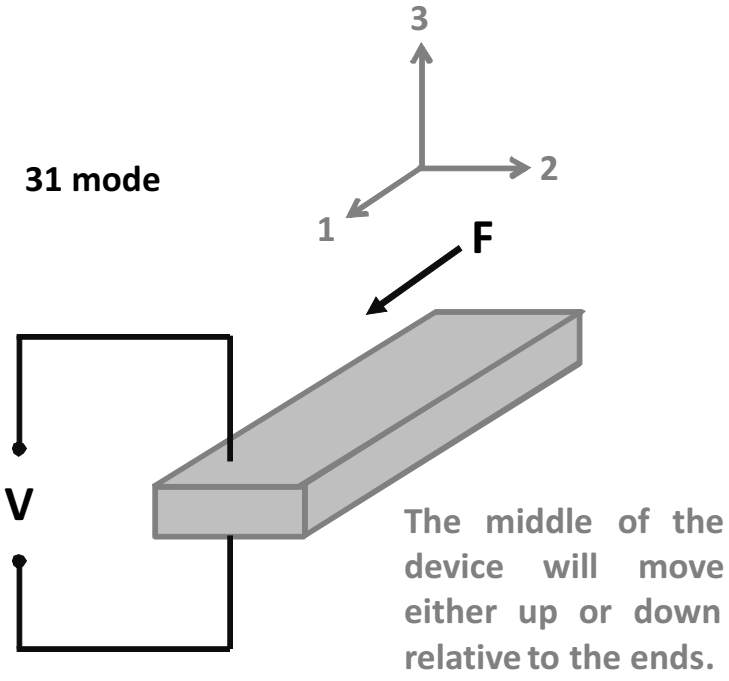

Figure 2.4: Piezoelectric film operates in 31 mode.

millimeter [18]. Piezoelectric material with a thickness of a few tens of nanometer has been reported [19]. They can be easily embedded into or layered onto a structure or a piece of garment without significantly altering the dimension(s) of the structure itself. This is specially beneficial to be used in applications which aerodynamic property is of particular concern, such as aircraft structure monitoring [20]. The range of applications for piezoelectric material is likely to keep expanding as manufacturers are continue to improve their products and reduce the production cost.

2.2.2 Electromagnetic oscillation

The Faraday's law of induction states that electric current would be generated on conductors positioned inside oscillating magnetic fields. Oscillating magnetic fields could be generated by the relative movement of a coil and permanent magnet(s). Figure 2.5 shows a computer generated image of an energy harvesting device based on the electromagnetic principle. A static wound copper coil is sandwiched between two permanent magnets. The cantilever beam connects with two permanent magnets in one end and a proof mass on the other. By adjusting the length, thickness and material of the cantilever beam, the resonant frequency of the harvesting device could be fine tuned to match the vibration frequency that appeared in the application environment [21]. An experimental prototype is shown in Figure 2.6.

Optimising the power processing/conditioning circuitry of the harvesting device, in general, can reduce the power loss and increase the overall efficiency of the device [23, 24, 25]. Employing innovative magnet layout design to increase the field strength is a more targeted approach to improve the efficiency of electromagnetic harvesting device [26].

The strength of the magnetic field is measured by its flux density, symbol 'B', unit 'Tesla (T)'. According to (2.1), the output voltage is proportional to the magnetic flux gradient, which is the rate of change of the magnetic flux. The strength of the magnetic field will rise if the flux gradient increases.

$$V = -N \times \frac{d\psi_m}{dt} \quad [4] \tag{2.1}$$

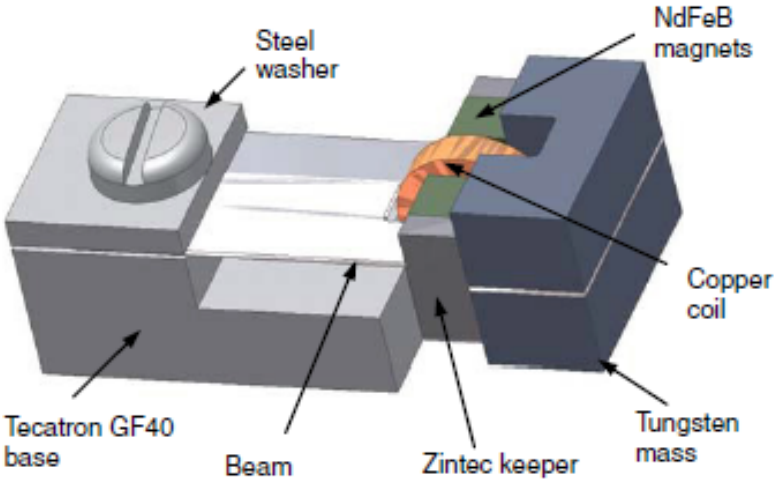

Figure 2.5: Computer generated image of an energy harvesting device based on electromagnetic principle [21] © IoP 2007.

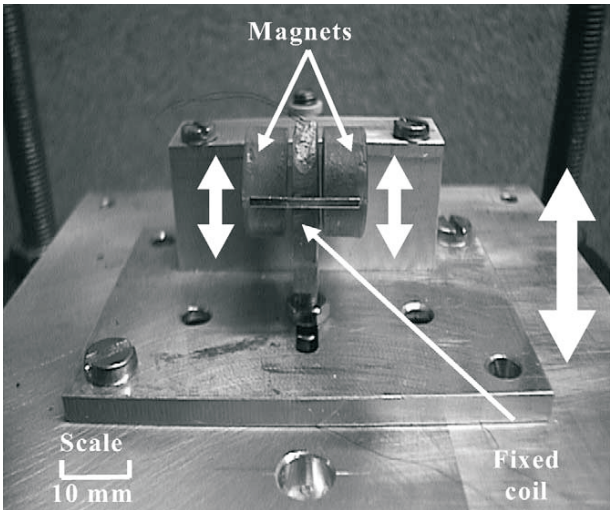

Figure 2.6: Experimental prototype of an electromagnetic vibration harvesting device [22] © Elsevier 2004.

where

V is the induced output voltage on the coil, V

N is number of turns of the wound copper coil

ψ_m is the magnetic flux, Wb, $\psi_m = BA$ in a uniform field

(A is the surface area that the magnetic flux passes through.)

$\frac{d\psi_m}{dt}$ is the magnetic flux rate of change against time

The most straight forward way to increase the flux gradient is to increase the flux density. The flux density in one side of the array will be doubled while negligible field is observed on the other side if several magnets are configured into a Halbach array. The side which the flux density has doubled is known as the 'active side'. The other side, where the field is negligible, is known as the 'quiet side' [28]. In Figure 2.7(a), those magnets with either '$\otimes$' or '$\odot$' signs on them are the main magnets. The transit magnets have either '$\leftarrow$' or '$\rightarrow$' signs on them. Either side of the x-axis is a single Halbach array.

Configuring the magnets into Halbach array has the potential to increase the output without substantially increase size of the device. However, one study found that the amount of energy harvested with a single Halbach array layout is actually less than the normal magnet layout configuration despite the elevated magnetic field strength [29]. In fact, the magnetic flux density decreases due to the lengthened flux path.

In order to shorten the flux path, two single Halbach arrays have been put together. The main magnets were made considerably wider than the transit magnets. This kind of configuration substantially shortens the flux path between the main magnets of opposite polarities and helps to increase the flux gradient. A double Halbach array set and a normal 4-magnet set are shown in Figure 2.7(a) and Figure 2.7(b) respectively. Both of them have identical dimensions ($28\times16\times1$ mm^3). The double Halbach array set has two pairs of main magnets and six pieces of transit magnets.

The active side of the double Halbach array in this case is underneath the structure, on the negative part of the z-axis. This is the best location, from the energy harvesting prospective, to put the coil. During the energy harvesting operation, the direction of movement of the magnet is along the y-axis. One study discovered that the output power of an electromagnetic harvesting device

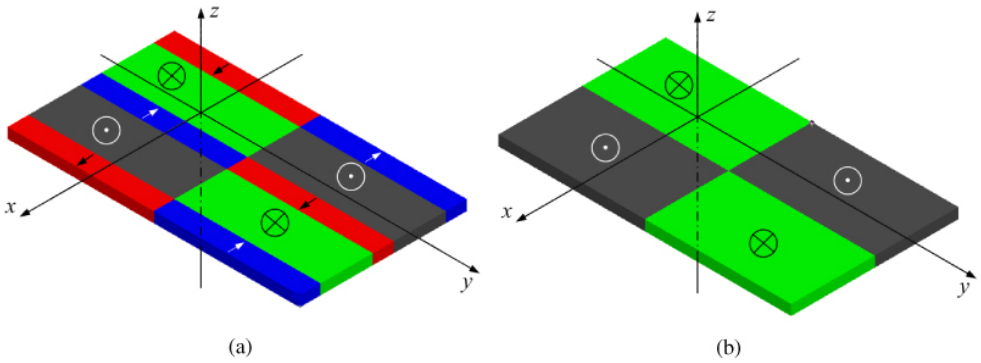

Figure 2.7: (a) Magnets arranged in a double Halbach array configuration, (b) Normal 4-magnet layout configuration [26] © PowerMEMS 2012.

equipped with the proposed double Halbach array layout magnets is about 50% higher than a similar size device with with normal layout magnets [26].

Commercially available electromagnetic vibration harvesting device has a volume of just over 130 cm^3 [30]. It is able to produce 3 mW of output power when the equivalent of a 50 mg proof mass is vibrating at its resonant frequency.

Electromagnetic harvesting device typically contains components like magnets, coils and weighted masses. The miniaturisation effort has been pursued in two directions. One kind of miniaturisation is to drastically reduce the size of all the components, similar to produce a miniature model of a conventional harvesting device. But the miniature size comes with the price of reduced power output. If the volume of the harvesting device, such as the one shown in Figure 2.5, is reduced to 0.15 cm^3, the output power drops down to a few tens of microwatts (μW).

The other kind of miniaturisation is to make the main components, as shown in Figure 2.8, in planar shape. Energy is generated by the out-of-plane horizontal motion between the magnet and coils [31]. The planar shape device has a thickness of only a few millimeter. It can easily be fitted onto a printed circuit board (PCB). The PCB itself acts as the proof mass. The horizontal displacement that can be achieved between the magnet and coil is restricted to only a few millimeter. It is difficult to obtain a high rate of change for the magnetic flux density with such a small misalignment. The output power is comparable to the first type of miniaturised device, which is in the regions of a few tens of microwatts.

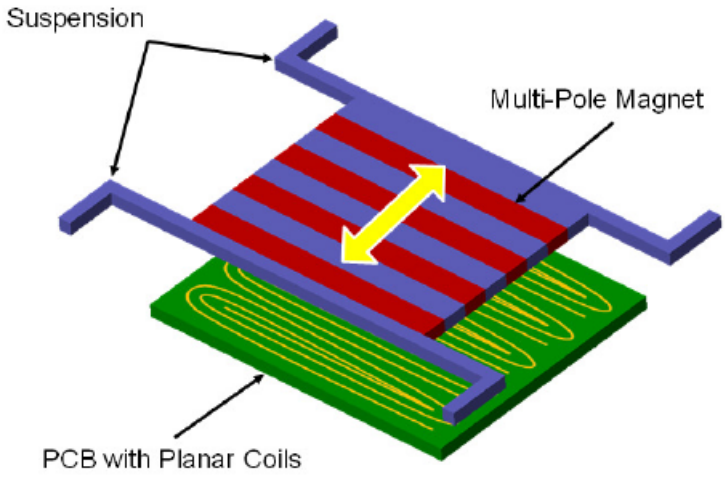

Figure 2.8: A conceptual planar electromagnetic harvesting device [31] © Power-MEMS 2012.

The planar shape, because of its physical characteristics, is more suitable for those harvesting devices that are making use of electrostatic movement to harness energy. This will be discussed in the next section.

2.2.3 Electrostatic movement

Energy can be stored in a capacitor. A capacitor could be made by putting two flat conducting plates parallel to each other and separated them by an insulation. The capacitance depends on the surface area of the parallel conducting plates, the distance and the permittivity of the medium between the plates. These relationships are represented by (2.2). Once the capacitor has been charged up, its electrical behaviour is represented by (2.3).

$$C = \frac{\varepsilon A}{d} \tag{2.2}$$

$$C = \frac{Q}{V} \tag{2.3}$$

where

C is the capacitance of the capacitor, F

ε is the permittivity of the medium, $\varepsilon = \varepsilon_0 = 8.85 \times 10^{-12}\ F/m$ at free space
A is the overlapping area of the two parallel plates, m^2
d is the distance between the two parallel plates, m
Q is the amount of electric charge the capacitor holds, C
V is the potential difference between the two parallel plates of the capacitor, V

The relationship between the electric charge, the voltage, and the physical attributes of a capacitor can be further derived from (2.2) and (2.3) into (2.4).

$$\frac{\varepsilon A}{d} = \frac{Q}{V} \Rightarrow\ Q = \frac{\varepsilon A V}{d}\ or\ V = \frac{Qd}{\varepsilon A} \tag{2.4}$$

Electric charge, as shown in (2.4), is proportional to the overlapping area of the parallel conducting plates ($Q \propto A$) and inversely proportional to the distance between the these plates ($Q \propto \frac{1}{d}$). On the other hand, the voltage is proportional to the distance between the parallel conducting plates ($V \propto d$) and inversely proportional to the overlapping area of these plates ($V \propto \frac{1}{A}$). The amount of energy stored on a capacitor can be obtained from:

$$W = \frac{1}{2}\ CV^2 = \frac{1}{2}\ C(\frac{Qd}{\varepsilon A})^2 \tag{2.5}$$

where
W is the energy that has been stored on the capacitor, J

The energy stored on a capacitor, as shown in (2.5), is proportional to the square of the voltage across the capacitor ($W \propto V^2$), and the amount of charge on the capacitor ($W \propto Q$). The physical dimensions of the conducting plates are fixed once they have been made. The most practical and efficient way to increase the energy on a capacitor is to increase the voltage.

The voltage on a capacitor, according to (2.4), is proportional to the separation distance between the parallel plates ($V \propto d$) and inversely proportional to the overlapping area of the parallel plates ($V \propto \frac{1}{A}$). One way to increase the voltage on the capacitor is to increase the distance between the two parallel plates. This can be achieved by moving the parallel plates further apart, commonly known as

'in-plane' movement. Another method is to decrease the overlapping area of the two parallel plates, which can be implemented by creating misalignment between the parallel plates. This is often being referred to as 'out-of-plane' movement. External force, such as the kinetic energy from vibration, is required to initiate and maintain both types of movement.

In-plane movement electrostatic harvesting device

A vibration harvesting device that is designed for harnessing energy from in-plane movement is shown in Figure 2.9. This device has three layers. The plate at the base layer and the discharging contacts on the top layer remain stationary. The middle layer is a plate that is capable to move between the base and top layers, in the directions indicated by the arrows. Each plate has a surface area of 2.25 cm^2 (15×15 mm) and a thickness of just over 1 mm [32].

The moving plate in the middle layer and the stationary plate at the base layer, in effect, form a capacitor with its capacitance determined by the distance between the the moving plate and the stationary plate.

Besides the stationary plate, the base layer also has a pair of charging contacts. The charging contacts are slightly thicker than the stationary plate. The charging contacts and the stationary plate are electrically isolated. The moving plate, at its resting position, would still has a small separation from the station plate and is electrically connected with the charging contacts.

This device needs to be charged up to a few volts in order to initiate the energy harvesting operation. Charge can be transferred onto the moving plate via the charging contacts. The device can be separated from the charging circuit after the initial charging has completed.

The moving plate will break free from its resting position and starts to travel away from the stationary plate when the momentum (= mass × velocity) experienced by the harvesting device exceeds the bond between the moving and stationary plates. The amount of charge on the harvesting device remains the same when the moving plate is drifting away from the stationary plate. This is because the harvesting device is electrically isolated. According to (2.2), capacitance is inversely proportional to the distance between the two conducting plates ($C \propto \frac{1}{d}$). The capacitance of the harvesting device will continue to decrease as

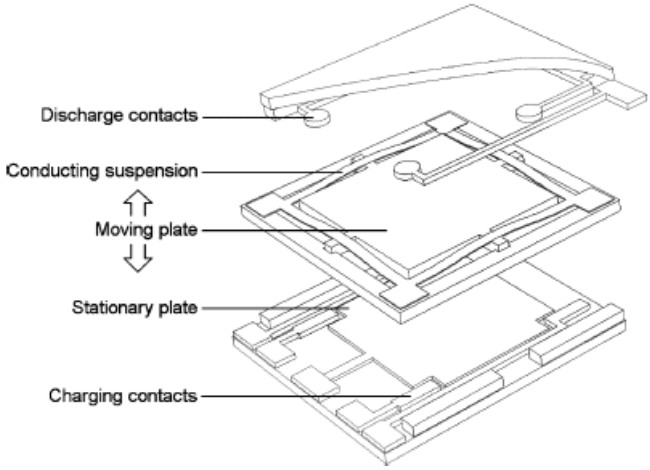

Figure 2.9: Dissected view of an electrostatic vibration energy harvesting device based on in-plane movement [32] © IEEE 2006.

long as the moving plate is travelling further away from the stationary plate.

Voltage across a capacitor is inversely proportional to the capacitance of a capacitor ($V \propto \frac{1}{C}$), therefore the voltage between the moving and stationary plates continue to increase. The total amount of energy stored on the capacitor, as shown in (2.5), is proportional to the square of the voltage across the capacitor and the capacitance of the capacitor ($W \propto V^2$ and $W \propto C$). The increase in voltage has a bigger positive impact on energy than the negative influence caused by the decrease in capacitance. The harvesting device would be able to accumulate more energy as the moving plate gets further away from the stationary plate.

The amount of energy accumulated on the harvesting device will continue to increase until the moving plate touches the discharging contacts on the top layer. The amount of energy that has been accumulated on the in-plane movement harvesting device is given by:

$$W_o = \frac{1}{2}(C_2V_2^2 - C_1V_1^2) = \frac{1}{2}Q(V_2 - V_1) \tag{2.6}$$

where

W_o is the amount energy that has been harnessed by the harvesting device, J

C_1 is the capacitance value when moving plate is at its resting position on, F

Table 2.2: Parameters of a electrostatic vibration harvesting device at key transitional moments of its operation [32].

Parameters	Initial Position	Maximum Separation
Charge	4.2 nC	4.2 nC
Voltage	30 V	250 V
Capacitance	140 pF	10 pF
Energy	63 nJ	525 nJ

C_2 is the capacitance value immediately before the moving plate touches the discharge contacts, F

V_1 is the voltage between the moving and stationary plates when the moving plate is at its resting position, V

V_2 is the voltage between the moving and stationary plates immediately before the moving plate touches the discharge contacts, V

Q is the amount of charge stored on the harvesting device, C

Parameters at key transitional moments of the operation of the in-plane harvesting device is shown in Table 2.2. The amount of energy harvested is approximately 462 nJ when the moving plate arrives at the maximum separation point.

The operation of the moving plate has two phases in each cycle. The moving plate is getting away from the stationary plate in the first phase. The voltage across the plates increases and additional charge is induced. Those charge induced during the first phase will be transferred out of the harvesting device once the moving plate touches the discharging contacts.

The moving plate travel towards to the stationary plate once the direction of external force changes. The gap between the two plates keeps decreasing in the second phase. Since $C \propto \frac{1}{d}$ and $C \propto \frac{1}{V}$, the capacitance will increase while the voltage continues to drop. The moving plate may even arrives back to the initial resting position. The second phase finishes, and the first phase starts, when external force pushes the moving plate away from the stationary plate again.

Out-of-plane movement electrostatic harvesting device

The implementation of the out-of-plane movement is realised by letting two parallel conducting plates to move horizontally with respect to each other. The disalignment of the two plates will reduce overlapping area between them and consequently reduce the capacitance of the harvesting device.

An example of utilising out-of-plane movement, although not being electrostatic, is shown in Figure 2.8. The moving plate is suspended in a way that it can only move in a direction which is parallel to the stationary plate in the base layer. The discharging contacts are on the sidewalls of the harvesting device.

Harvesting device that employs out-of-plane movement consists of only two layers and the gap between the plates remains unchanged throughout its operation. It generally has a lower height profile than the in-plane movement device. The overlapping area between the moving and stationary plates reduces during the first phase of operation. Since $V \propto \frac{1}{A}$, the potential difference across the two parallel conducting plates will increase. Consequently, the energy stored in the device will continue to increase until the moving plate touches the discharging contacts.

The moving plate will travel in a direction that causes the overlapping area between the plates to increase during the second phase. The capacitance of the harvesting device starts to recover. When both plates are fully aligned, the device is ready to accumulate the maximum possible amount of energy.

Optimisation and Possible Improvements

(a) Investigate the role of the initial voltage

The key for increasing the efficiency of the electrostatic harvesting device is to maximise the product of force-distance from the movable plate. If the initial voltage on the harvesting device, which is denoted as V_1 in (2.6), is too high, the bond between the plates could be too strong for the movable plate to either break free or travel the full distance that it is capable of. On other hand, the movable plate could break away 'prematurely' if V_1 is set too low. The momentum on the moving plate may not be as strong as it could be. The full capacity of the harvesting device is not being fully utilised.

The amount of charge stored on the harvesting device remains the same during the operation ($Q = C_1V_1 = C_2V_2$). Further derivation can be made by substituting $V_2 = \frac{C_1V_1}{C_2}$ into (2.6):

$$\begin{aligned} W_o &= \frac{1}{2}(C_2V_2^2 - C_1V_1^2) = \frac{1}{2}[C_2(\frac{C_1V_1}{C_2})^2 - C_1V_1^2] \\ &= \frac{1}{2}V_1^2(\frac{C_1^2}{C_2} - C_1) = \frac{1}{2}V_1^2\frac{C_1}{C_2}(C_1 - C_2) \end{aligned} \tag{2.7}$$

The maximum amount energy that could be harnessed by the harvesting device, as shown in (2.7), is heavily influenced by V_1. V_1 can be configured when the harvesting device undergoes the initial charging process. The optimal level of V_1 could allow the movable plate to break away just below the point of maximum acceleration. In other words, the movable plate becomes a moving plate when the momentum on the movable plate is very close to, if not exactly equals to, the theoretical maximum limit. The optimal level of V_1 depends on the dimension of the device.

It is a good practice to connect the harvesting device in parallel with another capacitor as a protection against excessively high voltage. The protection capacitor limits the maximum voltage that would appear across the harvesting device. The formula that takes the protection capacitor into account is:

$$W_o = \frac{1}{2}V_1^2\frac{C_1 - C_p}{C_2 - C_p}(C_1 - C_2) \tag{2.8}$$

where

C_p is the capacitance of the protection capacitor, F

(b) Increase the capacitance of the harvesting device

The distance which the movable plate can travel is constrained by the physical dimensions of the harvesting device. Altering the dimensions of a harvesting device may not be desirable in many cases. Another avenue for improving the harvesting device but without changing its dimensions, according to (2.2), is by increasing the permittivity (ε) of the medium in the space between the conducting plates.

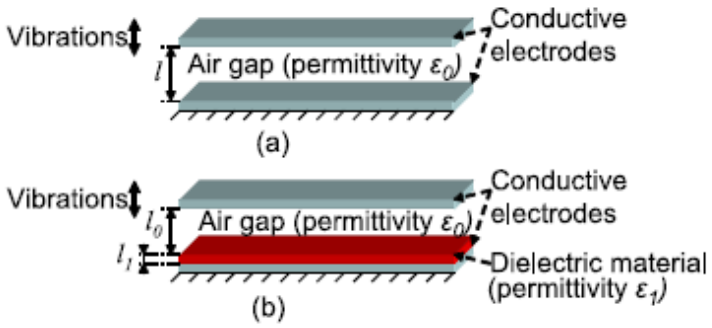

Figure 2.10: 'In-plane' motion electrostatic harvesting device: (a) free space between the conducting plates, separated by l. (b) dielectric material added on top of the stationary plate [33] © Elsevier 2011.

Filling the space up with dielectric material, which has a high permittivity, can increase the capacitance of the harvesting device substantially. However, this needs to be done in a way that doesn't reduce the distance which the movable plate can travel, especially for in-plane movement harvesting devices. A thin layer of dielectric material with high permittivity, as illustrated in Figure 2.10(b), is laid on top of the stationary plate while not reducing the distance that the moving plate can travel.

The permittivity of dielectric materials, such as rubber and porcelain, is 2 times and at least 4.5 times of the permittivity of free space respectively. An extra layer of dielectric material will make the space between the two plates will have variable permittivity. This phenomenon can be considered as two capacitors connecting in series. The overall capacitance of two capacitors connecting in series is slightly less than the capacitance of the smaller of the two capacitors.

The dielectric medium of the capacitor with a smaller capacitance is free space. The dielectric medium of the larger capacitor consists of a thin layer of solid insulation material. This means the value of C_2 changes very little while C_1 increases substantially. Larger amount of charge can be stored on the harvesting device when it is being charged up initially. According to (2.8), W_o will increase.

One study reported a 55 fold increase of the amount of energy harnessed after a layer of dielectric material has been installed on top of the stationary plate [33]. The presence of the solid dielectric layer not only helps to increase the amount

of energy the harvesting device can harness but also strengthened the electrical isolation of the two conducting plates within the device.

(c) Employ non-standard shape harvesting electrode

Electrostatic harvesting devices use planar-shaped harvesting electrodes. They are relatively simple to manufacture. However, as the analysis elaborated earlier in this section (Section 2.2.3), this type of harvesting electrode can only convert energy during the first phase of the operation. The harvesting device is in 're-covery' mode in the second phase. It is unable to convert the energy during this period. It is highly beneficial if the device is able to convert the energy at all times.

Improvement was made to the geometry of the harvesting electrode [34, 35]. An innovative geometry design is shown in Figure 2.11. Both the stationary and the movable electrodes are comb-shaped structures. Figure 2.12 is the close-up view of the stationary (fixed) and movable (mobile) electrodes. The overlapping length (L_f), width (w_f) and thickness (h_f) of each branch are 1970 μm, 30 μm and 380 μm respectively. The total overlapping area of each branch on the movable electrode is 0.76 mm^2.

Every branch on the movable electrode is sandwiched by two branches on the stationary electrode. Each branch on the movable electrode overlaps with the stationary electrode on three sides. Regardless of the direction of the movement, the harvesting device is converting kinetic energy from the vibration into electrical energy at all times.

The electrodes shown in Figure 2.12 has an air gap (d_o) of 43.5 μm running through the entire length of the overlapping area. As long as the movement of the movable electrode is not impeded, putting a layer of dielectric material to cover the overlapping surface on either electrode would enhance the electrostatic effect and help the harvesting device to achieve a higher power output.

Advantage(s) and disadvantage(s) of electrostatic harvesting device

Electrostatic harvesting device needs to be charged up first before it can start harvesting energy. This is an unavoidable inconvenience and needs to be taken into consideration when installing this type of device. Another challenge is that

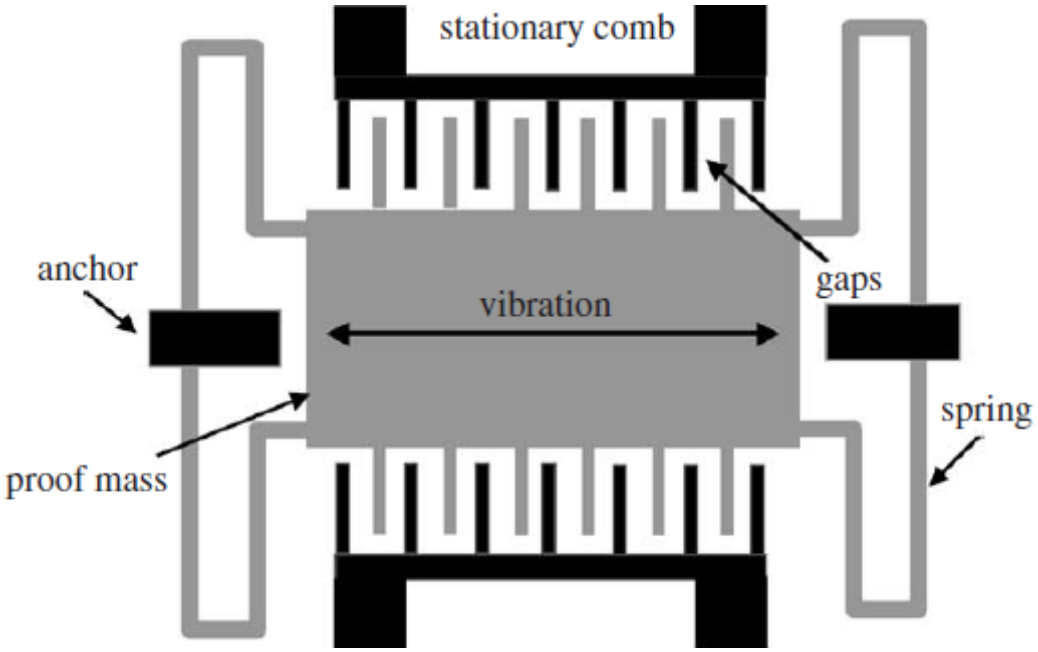

Figure 2.11: Electrostatic harvesting device with comb-shaped electrodes [34] © IoP 2016.

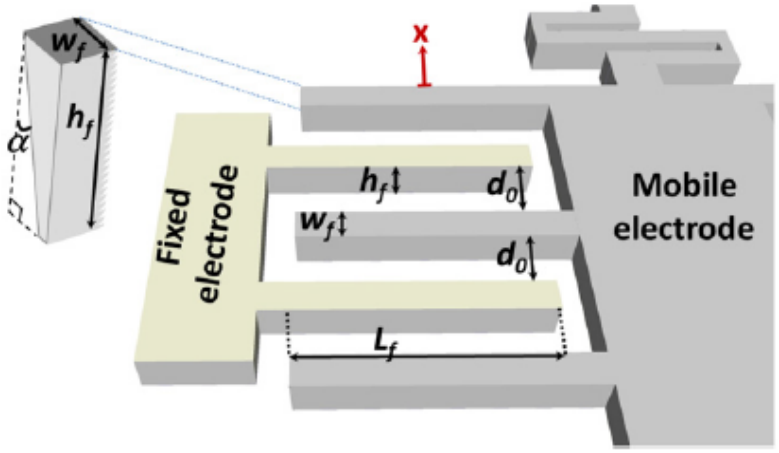

Figure 2.12: Close-up view of a short section of the comb-shaped stationary and movable electrodes [35] © IoP 2014.

the average power output of the harvesting device is proportional to its overall size. In other words, the power density is low.

Despite these disadvantages, electrostatic harvesting device possesses some features that make it attractive to be used in many applications. Electrostatic harvesting device can be housed inside a low profile package, which makes it relatively easy to be retrofitted onto a larger piece of equipment and doesn't significantly altering the external dimensions.

Power source with high output impedance can cause loading effect and significantly reduces the amount of energy that could be deliver to the load. Electrostatic harvesting device is electrically isolated from all the subsequent circuitry when it is harvesting energy. The nature of the operation mitigate the loading effect to a large extent.

2.2.4 Novel vibration conversion technique

Vibrations from different sources are likely to have different intensities and frequencies. It is very challenging to design a device that is able to efficiently convert the energy released by vibrations from multiple sources. One of the most promising methods is to use a hydraulic system to absorb the energy released by vibration in the first instance. It uses the flow of the hydraulic oil to power a motor-generator set. The electrical output can be adjusted by controlling the flow of the hydraulic oil. The highest conversion efficiency that has been reported is approximately 40% [36]. The dimensions of this kind of device make it more suitable for applications in the automotive, rail and large scale manufacture industries.

2.3 AC magnetic fields

Magnetic fields will be generated around a conductor when current is flowing through the conductor. The direction of the magnetic fields depends on the direction of the current flow while the strength of the magnetic fields is determined by the instantaneous amount of current flowing through the conductor. The strength of the magnetic fields within a few tens of centimeters of a 275 kV (AC) high voltage cable can well exceed 100 μT when the loading demand is heavy [37].

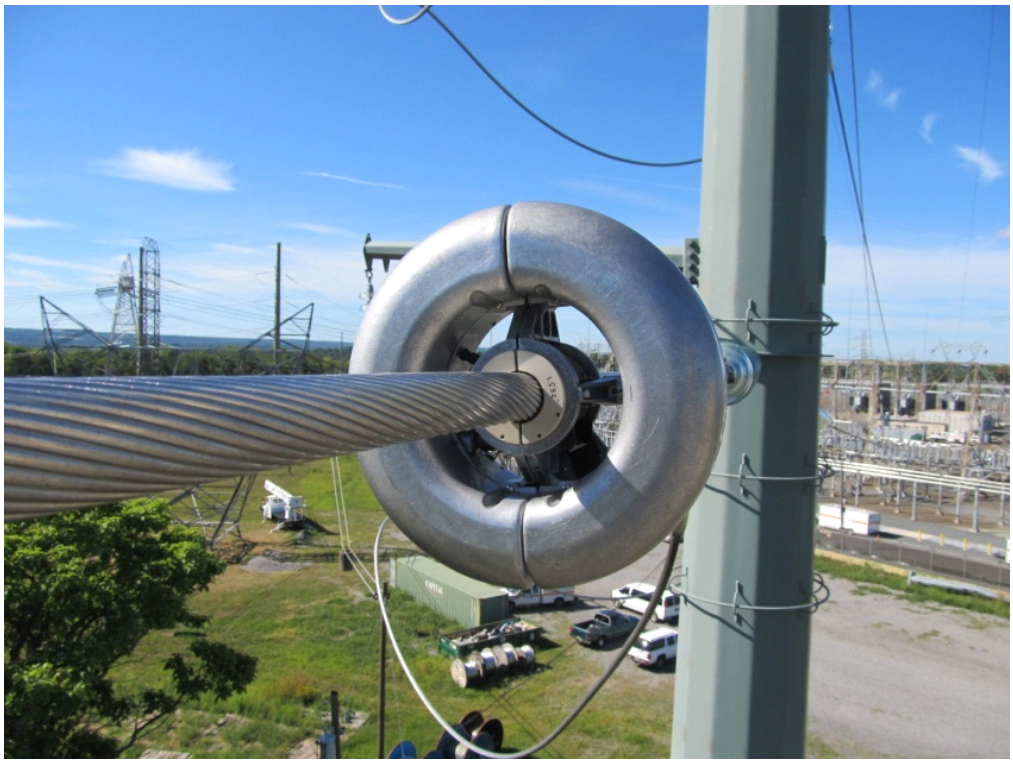

Figure 2.13: An installed power donut line monitor [38] © Underground Systems Inc 2016.

An overhead line with similar rating is expected to induce magnetic fields of comparable strength in its immediate vicinity. Condition monitoring device that incorporates magnetic fields harvesting, such as the overhead line monitoring instrument shown in Figure 2.13, is readily available on the market.

The volume of the device shown in Figure 2.13 is approximately 11260 cm^3 (32 cm in diameter and 14 cm in thickness/height). Its maximum output density is slightly above 2 muW/cm^3 [38]. It has been installed in arguably the most favourable location for harvesting energy from magnetic fields. The dimensions of the harvesting device could become unpractically large in order to achieve comparable power output (20 mW) in locations with much lower field strength [37]. This needs to be taken into account when considering any potential application for magnetic fields energy harvesting.

2.4 Thermal gradient

2.4.1 Thermoelectric effects

Seebeck effect is a thermomagnetic phenomenon discovered by German scientist Thomas Johann Seebeck in 1820. It states that magnetic field exists around a handful of metallic and semiconducting materials when there is a thermal gradient across the same piece of material [39]. A graphic illustration of the Seebeck effect is shown in Figure 2.14.

The Seebeck coefficient (S), as illustrated in Figure 2.14, is a proportionality constant of the open-circuit output voltage (ΔV and V_o) generated by the thermal gradient (T_h - T_c) across a particular piece of material.

Danish scientist Hans Christian Oersted reported that magnetic field can be generated by the flow of electrical current. He linked up his discovery with the Seebeck effect and gave a more clear explanation: For those materials with good thermoelectric properties, the presence of thermal gradient will generate an electric current to flow from the region with higher temperature to the part with lower temperature [39].

Besides the Seebeck effect, the Peltier effect and the Thomson effect are two other major discoveries that associate with the thermoelectrical phenomenon. Peltier effect states that, depends on the direction of the electric current, the junction

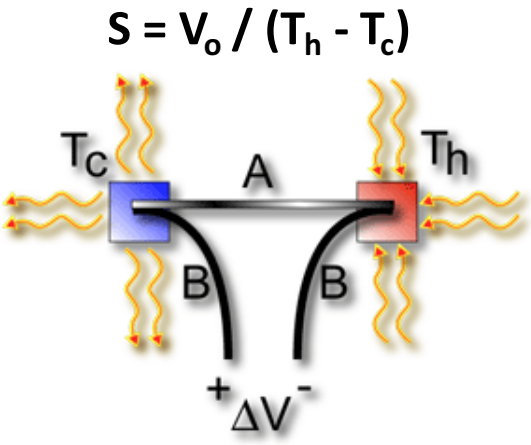

Figure 2.14: Illustration of the Seebeck effect [39] © Estonian Academy of Science and Engineering 2007.

of two dissimilar metals can either be heated up or cooled down [40]. Sir William Thomson, later Lord Kelvin, explained the relationship between the amount of heat, the electric current and the thermal gradient: Heat can be either absorbed or produced depends on the direction of current flow within a material that has thermal gradient [41].

Thermoelectric harvesting devices are designed to exploit these physical phenomenons. They convert heat flow into electrical power whenever thermal gradient appears.

2.4.2 Materials with outstanding thermoelectric properties

Compound materials consist of chemical elements from the nitrogen group and the oxygen/chalcogen group, such as Bismuth (Bi), Antimony (Sb), Tellurium (Te) and Selenium (SE), are essentially semiconductors with good thermoelectric properties. The most well known compound is Bismuth-Telluride (Bi_2Te_3). The positions of Bismuth and Tellurium in the periodic table of elements have been highlighted in Figure 2.15. Bismuth-Telluride is widely used in commercially available thermoelectric modules thanks to its outstanding efficiency when operates at room temperature (300 K or 27 °C) [42, 43].

A single thermoelectric conversion cell that consists of Bismuth, Antimony and Tellurium is shown in Figure 2.16. Each thermoelectric module would have multiple of these cells. Electric current will flow in the conversion cell, as indicated by the arrows shown in Figure 2.17, if thermal gradient exists between the rectangular blocks on the top and in the bottom of the doping areas.

The performance of the thermoelectric conversion cell is commonly represented by a dimensionless 'Figure of Merit', denoted as 'ZT'. The value of ZT, as derived in (2.9), is heavily influenced by the material(s) that make up the cell [40, 45]. In addition, the figure of merit can be enhanced by manipulating the crystal structure of the thermoelectric material, using techniques such as self-organised superlattices, quantum-dots and nano-crystalline inclusions [46].

$$ZT = \frac{S^2 \sigma T}{\kappa} \tag{2.9}$$

where

ZT is the dimensionless performance figure of merit of a thermoelectric cell

S is the Seebeck coefficient, V/K (volts per kelvin)

σ is the electrical conductivity, S/m (siemens per meter)

T is the absolute temperature of the ambient environment, K (Kelvin)

κ is the thermal conductivity, W/m*K (watts per meter Kelvin)

Power factor ($PF = S^2\sigma$) is another thermoelectric efficiency indicator. It suggests that, from the thermoelectric conversion point of view, the best material is simultaneously a good electrical conductor to minimise the joule heating, a poor thermal conductor to maintain the temperature difference and has a high Seebeck coefficient to increase the output voltage. Making a material that processes all these attributes is very challenging.

Besides the thermoelectric properties of the material, the conversion efficiency also depends on the geometric dimensions of the thermoelectric cell(s) [47, 48]. Graphene has a thickness of only one atom. It is the thinnest form of pure carbon known to man today and has attracted considerable attention in recent years thanks to its unique characteristics [49, 50]. Recent studies suggest that

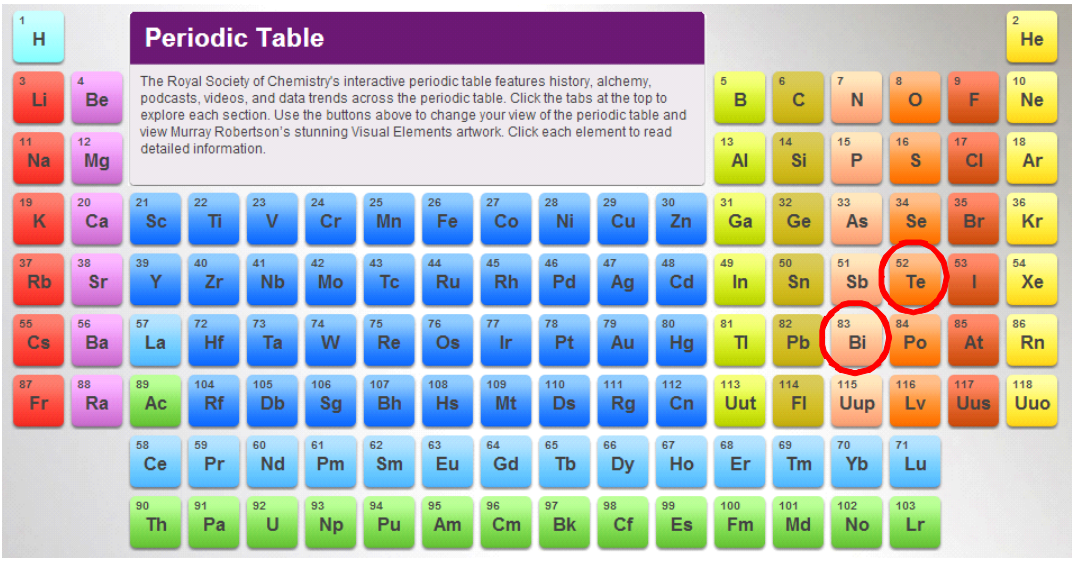

Figure 2.15: Periodic table of elements with bismuth and tellurium highlighted [44] © Royal Society of Chemistry.

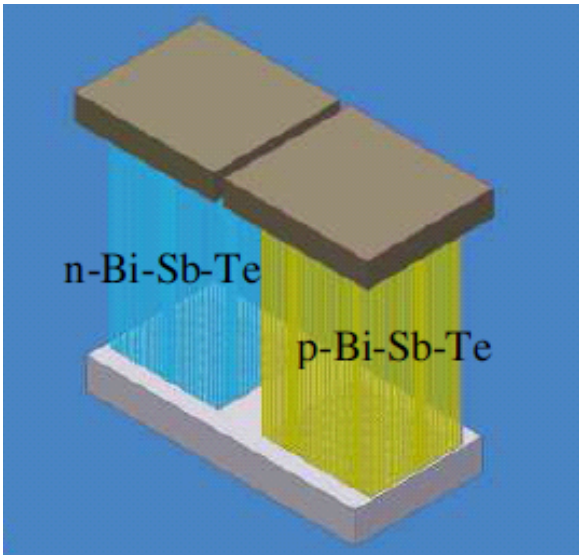

Figure 2.16: Generic thermoelectric conversion cell [51] © PowerMEMS 2007.

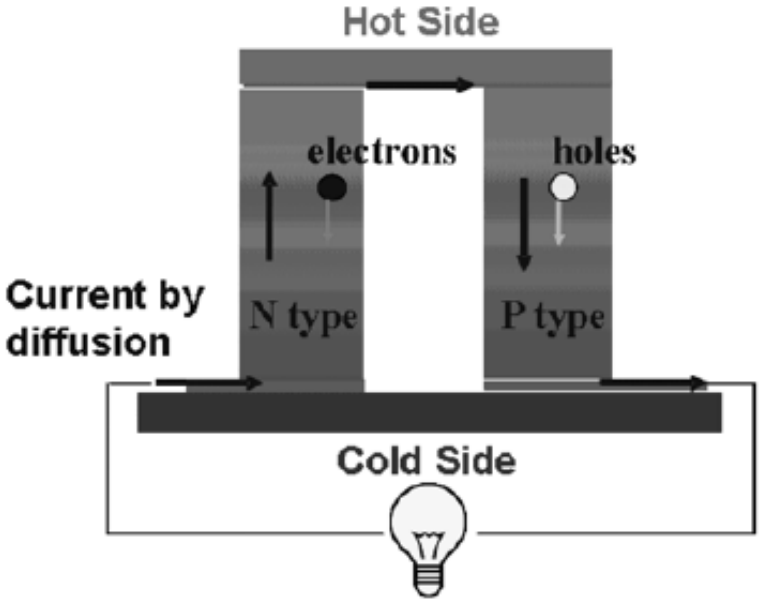

Figure 2.17: Cross-sectional view of thermoelectric coupling in action [45] © Springer 2009.

Table 2.3: Figure of merit of composite materials and graphene nanoribbons of optimised length at 300 K.

Thermoelectric Materials	Figure of Merit (ZT)
Bi_2Te_3	0.97 [53]
$Bi_{2-x}Sb_xTe_3$	1.2 [45]
Graphene nanoribbons	2.2 [52]

graphene nanoribbons have excellent thermoelectric conversion capability [51, 52]. The thermoelectric figure of merit of graphene nanoribbons, as shown in Table 2.3, is substantially higher than those composite materials that consist of Bismuth, Tellurium and/or Antimony.

The relationships between the figure of merit of the graphene-based conversion cell, its length and ambient temperature have been plotted in Figure 2.18. The optimal length of the graphene nanoribbon for operating under room temperature is approximately 0.4 μm. It can achieve a figure of merit of 2.2. A rise in ambient temperature reduces the thermal conductivity. The maximum value of the figure of merit which an optimised graphene nanoribbon can achieve also increases. Graphene-based material demonstrates better thermoelectric conversion performance than other traditional thermoelectric materials. It is expected that graphene-based material will play an important role in the future development of thermoelectric harvesting devices.

2.4.3 The structure of thermoelectric harvesting device

The energy source of a thermoelectric harvesting device is the thermal gradient across the device itself. Higher conversion efficiency is achieved by creating a larger potential difference from the same thermal gradient. Higher output voltage can be obtained by connecting more conversion cells in series. Figure 2.19 shows the equivalent circuit of connecting multiple conversion cells in series. Cells in each column could share a common substrate to increase the thermal exchange contact area. A larger thermal exchange contact area facilitates more thermal coupling to take place [47, 53, 54].

An actual section of the thermoelectric module is shown in Figure 2.20. Con-

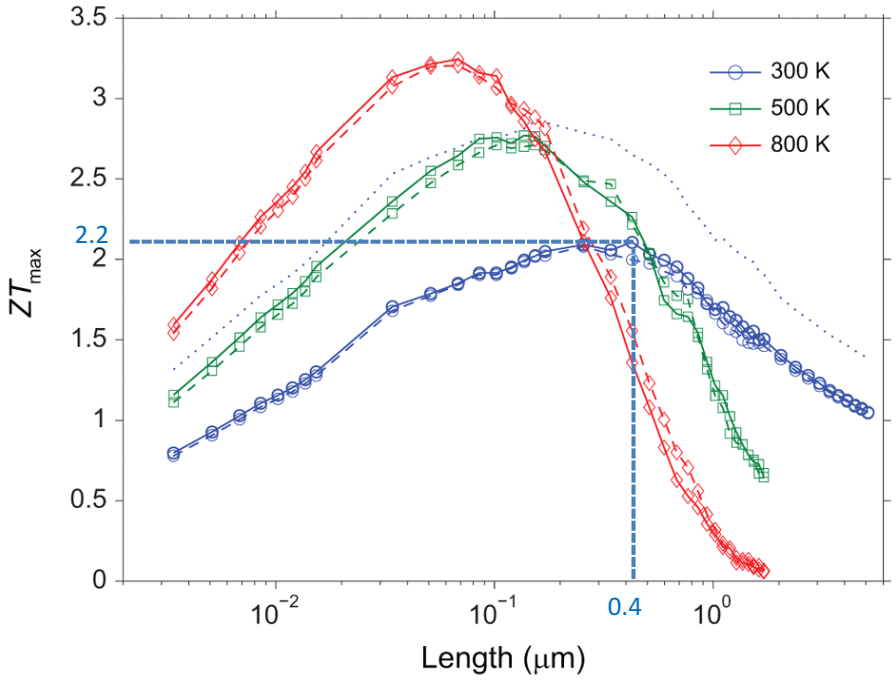

Figure 2.18: Figure of merit of the graphene-based thermoelectric conversion cell with respect to its length and the ambient temperature [52] © Nature 2013.

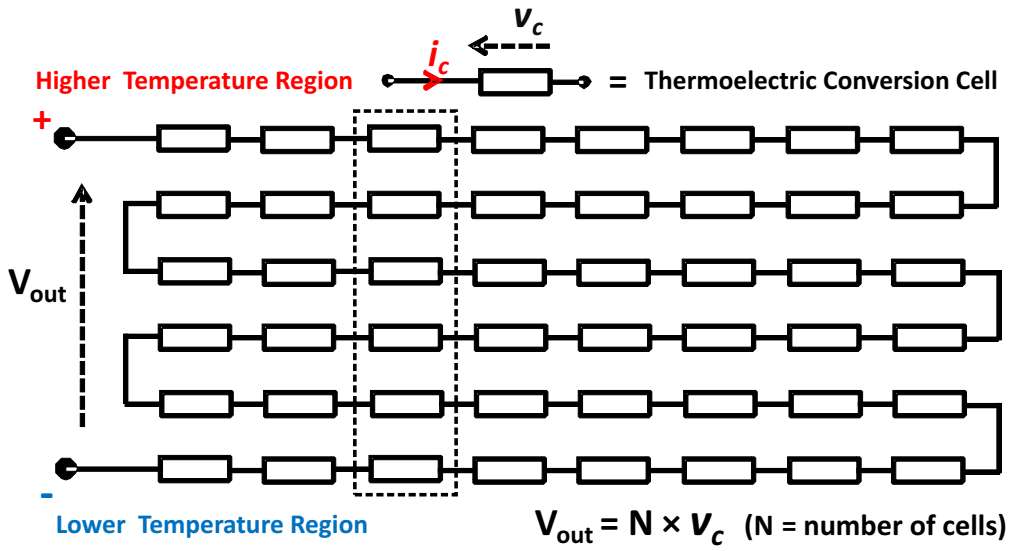

Figure 2.19: Thermoelectric conversion cells connected electrically in series to facilitates more thermal coupling.

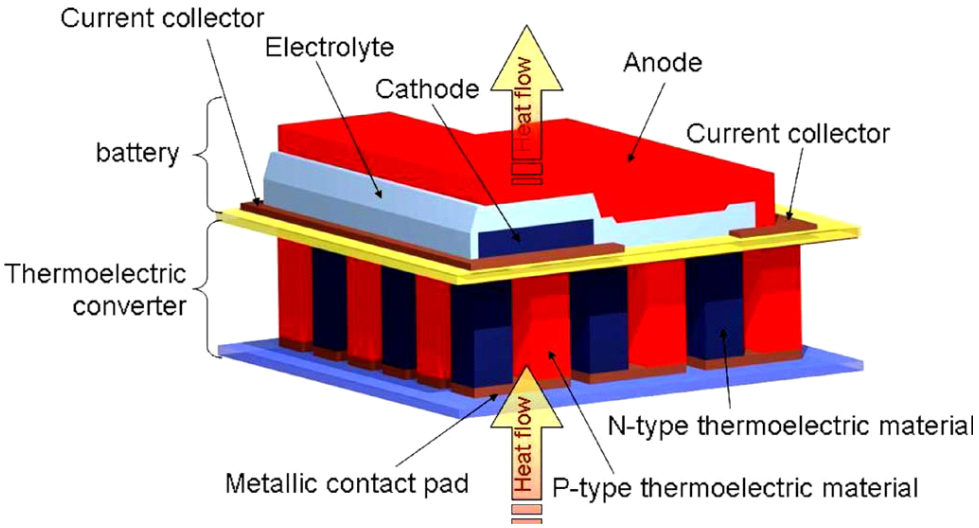

Figure 2.20: Components of a thermoelectric device [53] © IEEE 2010.

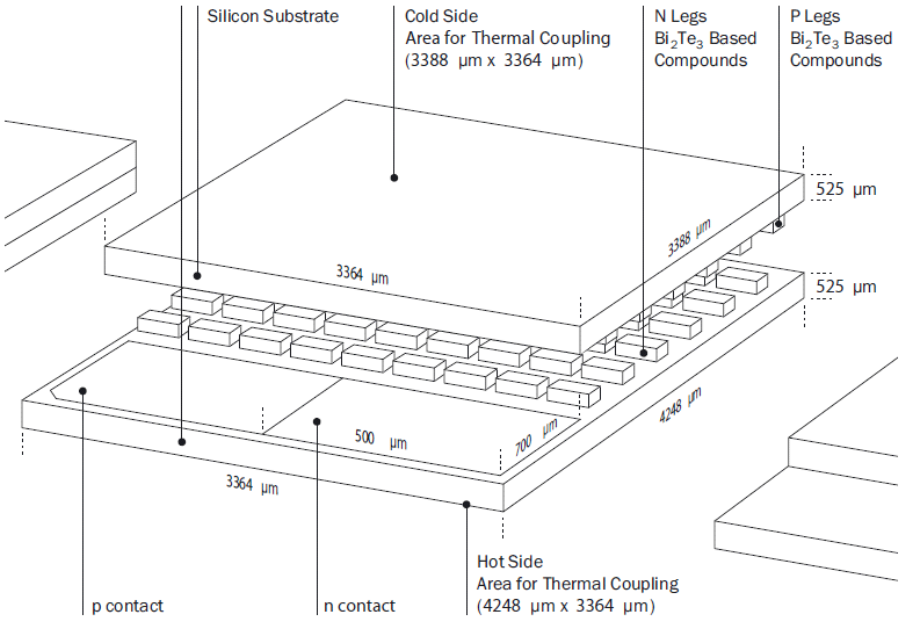

Figure 2.21: Schematic of a commercially available thermoelectric device [55] © Micropelt.

ventional thin-film semiconductor fabrication techniques have been used to produce cross-plane heat flow thermoelectric conversion cells [53]. The metallic contact pads act as the thermal conductors and ensure the heat flow path is perpendicular to the module surface. Multiple columns of cells share the same substrate to maximise the thermal exchange contact area.

The schematic of a commercially available Bismuth-Telluride based thermoelectric device is shown in Figure 2.21. It can accommodate up to 100 conversion cells, or 'leg pairs' as the manufacturer called them, per square millimeter (mm^2). It is less than 1.1 mm thick. The thin substrate ensures a fast response time. The manufacturer claims it take less than 3 ms from the presence of a thermal gradient across the device to the appearance of an output voltage. The Seebeck coefficient at room temperature is 140 mV/K. This means the device is able to produce an output voltage of 700 mV when the thermal gradient is as low as 5 K [55].

2.4.4 Energy management

The most power intensive activity of a wireless sensor is to transmit or relay data. The average output of an energy harvesting device is definitely insufficient to satisfy the demand of power intensive activities of a wireless sensor. If the amount of data that needs to be handled is small, power intensive activities only last up to a few seconds. It takes the harvesting device a long period, i.e. a few tens of minutes or even longer, to harness sufficient amount of energy for the wireless sensor to carry out a few seconds of power intensive activity. This problem applies to almost all types of energy harvesting device but not exclusively to thermoelectric harvest device.

An energy buffer is needed to accumulate, store and release energy in a manner that could bridge the mismatch. Figure 2.22 shows the block diagram of an energy buffer.

The output voltage of commercially available thermoelectric harvesting devices is in the order of a few hundreds of millivolts [55]. Modern wireless sensors operates at at a few volts. It is necessary to include a step-up converter in the energy buffer.

Off-the-shelf converter has a minimum start-up voltage, which is determ-

ined by the threshold voltage of its internal switching transistors. If the output voltage from the thermoelectric harvesting device is expected to be lower than this threshold voltage, placing a charge pump in front of the step-up converter could solve this problem.

The function of the charge pump is to accumulate sufficient amount of charge onto a dedicated capacitor so that the voltage across it can reach the start-up voltage of the step-up converter. The charge capacitor should be large enough to provide the necessary power to initiate the step-up converter while not too large to make sure the start-up time is not excessively long. Once the step-up converter starts to operate, its output is fed back to the input. It will keep the step-up converter in stand-alone mode and continue to perform its function.

An energy buffer circuit is shown in Figure 2.23. The charge pump is able to charge up C_2 even if the output voltage of the thermoelectric harvesting device, denoted as 'TEG', is as low as 250 mV [56]. The charge pump will send out a signal to switch on the step-up converter once the voltage on C_2 reaches the threshold voltage of the step-up converter.

The output of the step-up converter is fed back to the input through an internal diode D_2. The step-up converter is able to produce a regulated output even if the input drops down to 150 mV [56]. Energy buffer that is able to produce a consistent 1 V output from input voltage as low as 20 mV has been reported [57].

Figure 2.24 shows the voltage and current waveforms of the energy buffer.

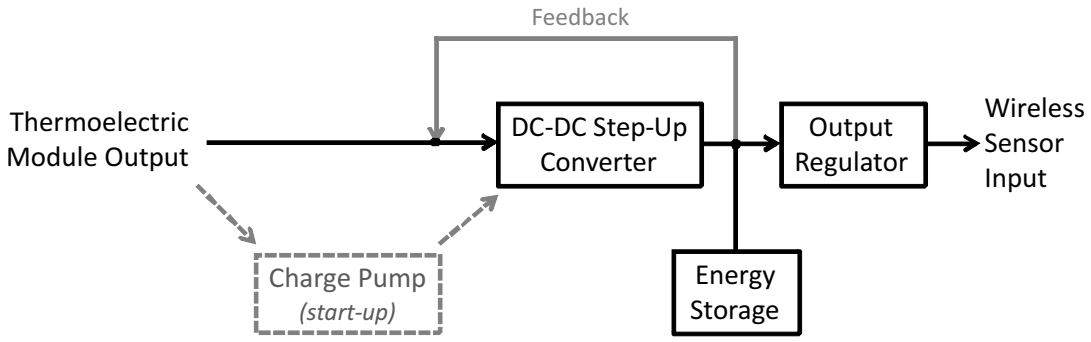

Figure 2.22: Constituent parts of an energy buffer.

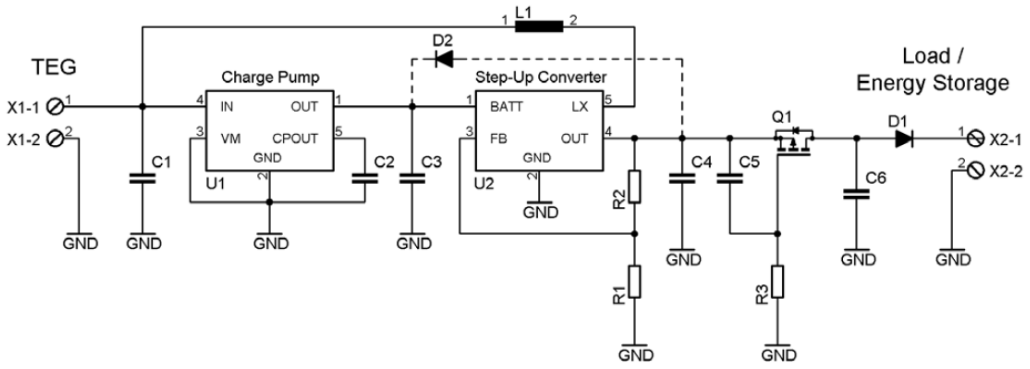

Figure 2.23: An energy buffer circuit [56] © DCIS 2006.

Assuming the thermoelectric harvesting device is supplying power to the energy buffer in a continuous manner, the voltage across the storage capacitor ('C_4' in Figure 2.23) keeps rising whenever the load is 'sleeping' or inactive. It means the storage capacitor accumulates more and more energy.

Energy could be supplied to the load once the voltage on the storage capacitor is above the output target voltage. As long as the voltage on the storage capacitor is above the target output level, the output voltage of the energy buffer is able to stay constant at the target output level even the load is drawing a considerable amount of current. Output from the energy buffer will be cut off once the voltage on the storage capacitor drops down to the target output level. This is to preserve the energy on the storage capacitor and keep the step-up converter in stand-alone mode.

The design and operation of the energy buffer will be discussed in greater detail in Chapter 6.

2.4.5 Applications

Thermoelectric harvesting devices, in theory, can be used in any applications where thermal gradient exists. For example, human skin of a live person emits around 100 W/m^2 (10 mW/cm^2) even if this person is not doing any physical activity [13]. Japanese watch manufacturer Seiko has successfully produced a wristwatch that is powered by an thermoelectric power module embedded inside

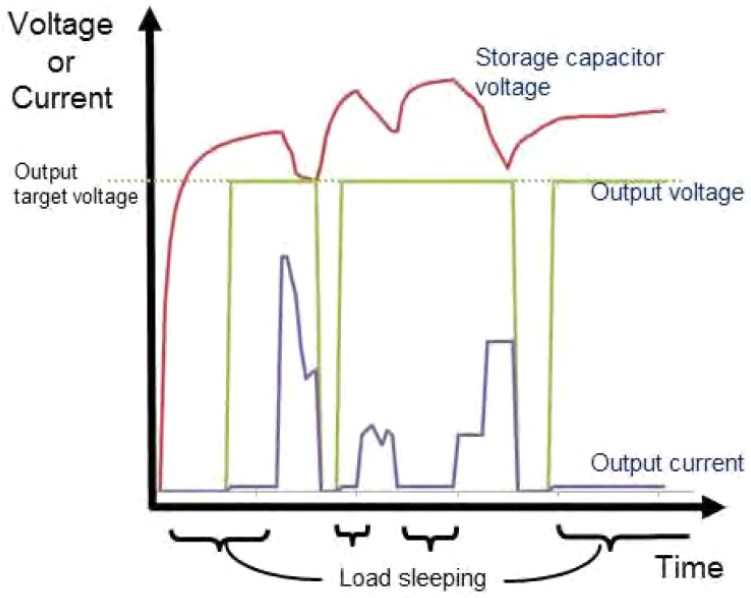

Figure 2.24: Voltage and current output waveforms of an energy buffer [58] © Micropelt.

the watch [42].

The key for increasing the power output is to maximise thermal exchange area between the harvesting device and the human skin. Research is underway to develop thermoelectric fabrics that are flexible enough to be worn as clothing and being able to carry out the energy conversion at the same time. It has been reported that 4 mW/m^2 could be produced by one type of thermoelectric fabric when the temperature difference between two sides of the fabric is 10 K. The output voltage could reach 3 mV if a person wearing 0.025 m^2 clothes made from the fabric is standing outdoors (at 19 °C or 292 K) [59, 60].

Commercially available thermoelectric harvesting devices are fabricated on a piece of thin film substrate [55]. Besides light in weight, thin film also has the advantages of flexibility and low profile. These features are highly desirable for retro-fitting and for use in weight/space sensitive applications.

One such application is to power sensors that monitor the structural health of an aircraft. The fuselage of a modern commercial airliner experiences rapid temperature change during both take-off and landing. These are excellent op-

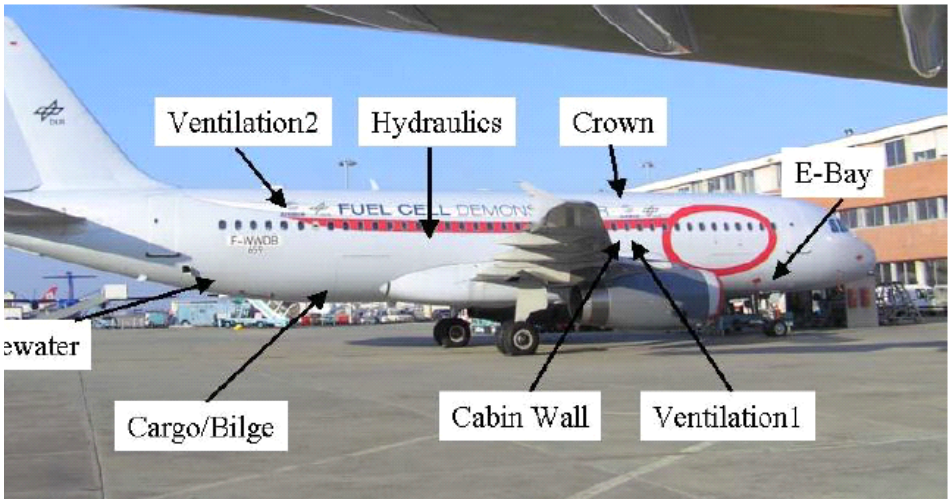

Figure 2.25: Positions on the fuselage of a commercial airliner where thermoelectric harvesting devices have been installed [62] © IoP 2012.

portunities for thermoelectric harvesting devices to convert energy. One study has installed several thermoelectric harvesting devices on the fuselage of an airliner in order to test their effectiveness [62]. The positions of the thermoelectric harvesting devices on the airliner's fuselage is shown in Figure 2.25.

The thermal gradient, in this case, is generated by connecting one side of the harvesting device with a thermal reservoir and establish direct contact of the fuselage with the other side. The thermal reservoir a few grams of water. The temperature of the water is hotter than the the fuselage when the aircraft is in the air and colder than the fuselage when the plane is on the ground [61]. The biggest temperature difference that has been discovered is around the cargo door. A differential as high as 40 °K has been observed. State-of-the-art thermoelectric device is able to produce a peak output power of almost 35 mW [62]. Research effort is underway to produce an energy buffer that is able to handle the dynamic change in temperature and provide a stable output to the monitoring sensor [63].

The most apparent advantage of thermoelectric harvesting device is that it has no mechanical moving parts. The energy conversion process occurs at molecular level. It can produce an output in the presence of a thermal gradient.

Energy from different sources may be available simultaneously or appear at different times. For example, vibration from the aircraft could also be harnessed

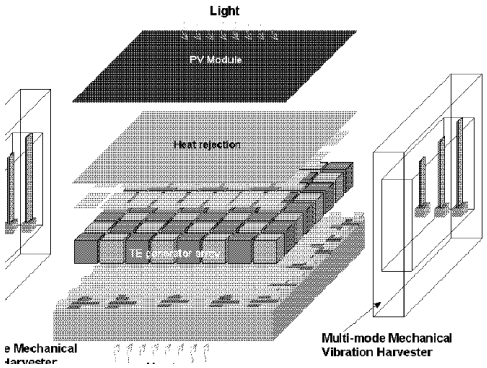

Figure 2.26: Schematic of a conceptual energy harvesting device which contains multiple harvesting components [46] © IEEE 2007.

to power monitoring sensors. It would be highly beneficial if one device is able to harvest energy from different sources concurrently. A conceptual energy harvesting device is shown in Figure 2.26. It contains multiple harvesting components. The type(s) of harvesting components contained in the device can be adjusted to suit any specific application. More energy can be harvested if multiple sources exist at the same time.

2.5 Radio frequency signals

Transmission signals from broadcasting, such as television and radio, and various means of wireless communication, like WiFi and mobile phone signals, are typical examples of radio frequency (RF) waves. The existence of radio frequency (RF) signals is a pervasive aspect of the modern society.

It has been envisaged, as shown in Figure 2.27, new generation of wireless sensor is not only able to transmit data but also capable of harvesting energy from RF waves. Application areas of RF energy harvesting can be categorised by the RF field density and total rectenna (= antenna + rectifier) output power [64]. Rectenna is discussed in greater detail in Section 2.5.3.

The relationship between the transmitted and received power of an isotropically radiated RF source in free space is governed by (2.10), which is the Friis

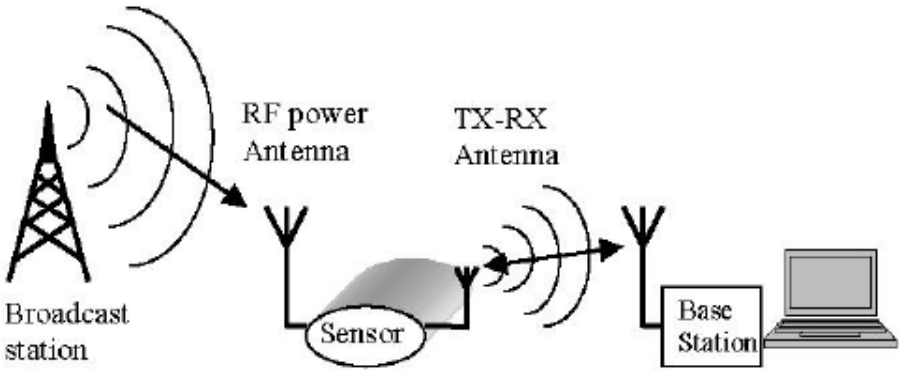

Figure 2.27: Desirable capabilities of new generation of wireless sensor [65] © IEEE 2008.

transmission formula [4]. The effective aperture/area of an antenna is a measure of how effective an antenna is at receiving power. It can be calculated by (2.11) if the gain of the antenna is known. The path loss between the transmission and receiving antennae is calculated by (2.12).

$$P_r = P_t \times \frac{A_{er} A_{et}}{r^2 \lambda^2} \tag{2.10}$$

$$A_e = \frac{c^2}{f^2} \times \frac{10^{\frac{G}{10}}}{4\pi} \tag{2.11}$$

$$P_L = 20log\frac{4\pi r}{\lambda} \tag{2.12}$$

where

P_r is the received power, W

P_t is the transmitted power, W

P_L is the path loss from the transmitting to the receiving antenna, dB

A_{er} is the effective aperture of the receiving antenna, m^2

A_{et} is the effective aperture of the transmitting antenna, m^2

G is the gain of the antenna, dB

r is the distance between the transmitting and receiving antenna, m
λ is the wavelength of the signal, m, $\lambda = \frac{c}{f}$ in free space
(c is the speed of light in free space and f is the frequency of the signal)

The received power, as shown in (2.10), is inversely proportional to the square of the wavelength of the signal. The wavelength is inversely proportional to frequency. Consequently, the received power is proportional to the square of the frequency ($P_r \propto f^2$). In addition, the available power to the receiving antenna will decrease by 6 dB (25% of the current starting value) if the distance between the transmitting and receiving antennae (r) is doubled. The overall effect of these factors need be taken into consideration when estimate is made on the amount of power available on the receiving end.

2.5.1 Radio Frequency IDentification (RFID)

RFID technology is arguably the most obvious application that involves data transmission using the energy harvested from a RF source. Passive RFID tags are gradually replacing bar codes for improved efficiency and security. However, the technical features associated with RFID differ from RF energy harvesting device in several ways [66].

The biggest difference is that the tag itself doesn't actively harvest any energy. Energy is sent to the tag by the reader/scanner. In contrast, a RF harvesting device is actively harnessing the energy from the ambient RF field. Further more, the difference in power level and operation range further distinguishes RFID technology from RF harvesting device. The RFID reader is usually a few centimeters, at most up to a few tens of centimeters, away from the tag. The frequency of the signal remains constant at 13.56 MHz. Both the transmission and receiving circuits are designed to make them well-matched because the operating condition stays the same. The power sent by the reader to the tag is in the region of a few tens of milliwatts. By contrast, a RF harvesting device could be at least a few tens of metres away from the energy source(s). Signals from different sources are likely to have different frequencies. The power density is much lower than the RFID operating environment.

RFID technology may share some similarities with RF energy harvesting, such

as transfer RF energy wirelessly through free space. But RFID technology has its own distinct features and its technical characteristics doesn't fit with the definition of energy harvesting. Therefore it has not be further investigated in this study.

2.5.2 RF energy sources

An overview of the RF signal strength in the general and work environment from 10 kHz to 30 GHz is presented in Mantiply *et al.* [67]. Some of the strongest signals have been detected are in locations adjacent to long distance navigational transmitters (frequency range 30 kHz to 300 kHz) and around the terrestrial microwave relay (frequency range 3 GHz to 30 GHz). However, few of these facilities are located in urban centres. Signals in these frequency bands attract little interest from the energy harvesting research community.

Urban space enjoys good coverage of commercial RF signals. In the UK, the transmission power of radio stations (AM - 180 kHz to 1.6 MHz, FM - 88 to 108 MHz) and TV channels (470 MHz to 854 MHz) starts from a few tens of kilo-watt and gets up to a few hundreds of kilo-watt [68]. Mobile phone towers, which are more densely 'populated' in a urban environment, transmit mobile signals (900 MHz and/or 1.8 GHz) at up to 20 W per carrier. Each tower could radiate close to 100 W when transmitting signals for a few carriers simultaneously [69, 70]. All of these signals, from the RF energy sources prospective, have the benefits of good geographical coverage and continuous stable transmission in metropolitan areas. Energy from these sources could be harvested to power wireless devices. Harvesting energy from these sources has attracted considerable interests [71, 72, 73].

RF power density at a particular location depends on the distance to the energy source and the frequency of the signal if the transmission strength is consistent. The measurement result presented in Figure 2.28 was taken in a city centre location that is a few hundred metres away from any transmission antenna. Power density above -20 dBm/m^2 (10.0 μW/m^2) could be seen in several frequency bands: 900 MHz - 1 GHz, 1.8 GHz - 1.9 GHZ, 2.3 GHz - 2.4 GHz and 2.8 GHz - 2.9 GHz.

The maximum power density, which is -14.5 dBm/m^2 (35.5 μW/m^2), is detected in the 1.8 GHz - 1.9 GHz band. This band coincides with the frequency

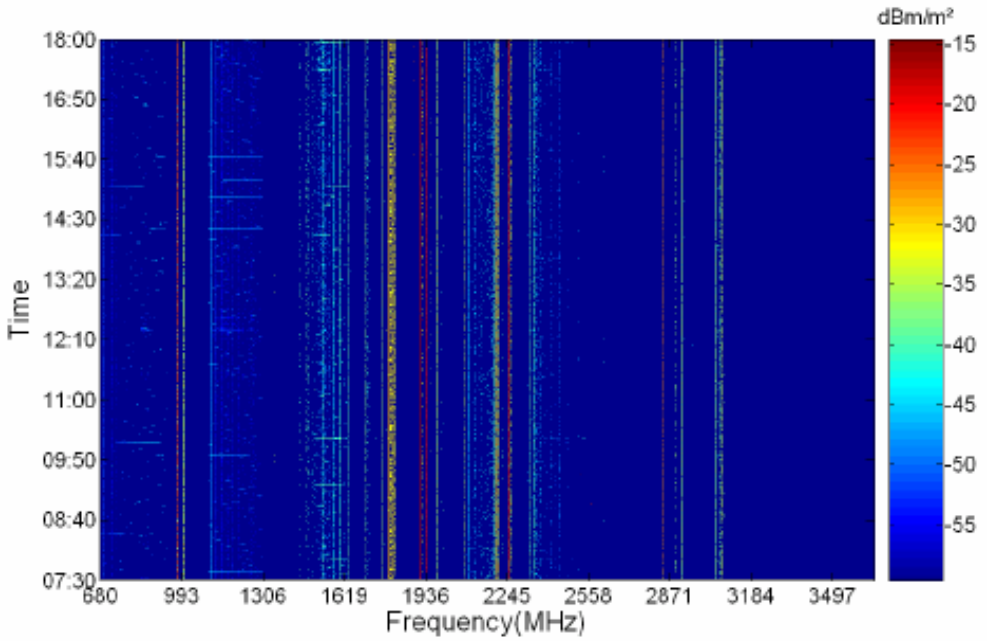

Figure 2.28: Measured RF power density (in a negative number scale) between 680 MHz and 3.5 GHz [71] © ICREPQ 2010.

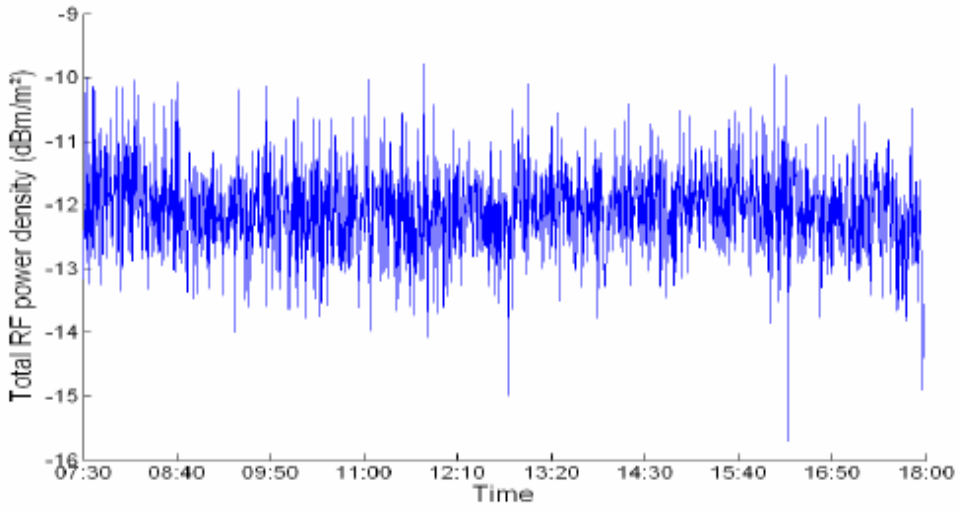

Figure 2.29: Variation of the combined RF power density from 680 MHz to 3.5 GHz in an 11-hour period [71] © ICREPQ 2010.

spectrum used by the GSM-1800 based mobile network. Figure 2.29 shows the

combined power density from 680 MHz to 3.5 GHz. The average combined power density at the measurement point is approximately -12 dBm/m^2 (63.1 μW/m^2). Other studies also obtained similar results [66, 73, 74].

In summary, the transmission power and the dimension of the transmitting antenna are tightly regulated. The distance between the receiving and transmitting antennae depends on individual application. These are factors beyond the control of the engineers who are interested in designing RF energy harvesting devices.

2.5.3 RF energy harvesting devices

Measurement result presented in Figure 2.28 shows that a signal with the highest frequency doesn't necessarily have the the highest power density. From the harvesting efficiency points of view, it is beneficial to identify frequency band(s) with the highest power density and design harvesting devices that could closely matched the prospective frequency band(s). The building blocks of a RF energy harvesting device are shown in Figure 2.30. The most important part of the harvesting device is the rectenna.

Rectenna

The constituent parts of a rectenna is shown in Figure 2.31. The antenna is used for coupling with the targeted RF signal. The impedance matching network is to ensure maximum power transfer. The reactance of the antenna and rectific-

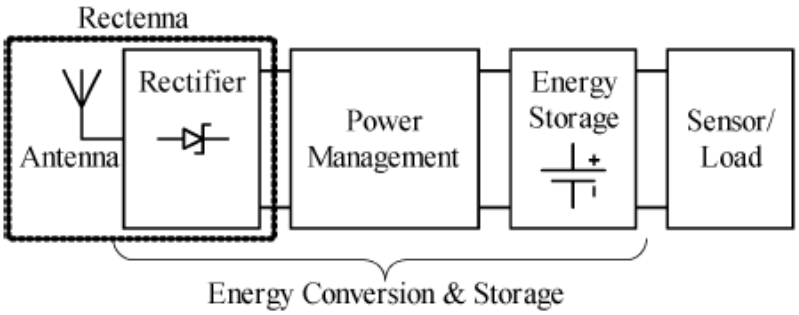

Figure 2.30: Constituent parts of a RF energy harvesting device [64] © IEEE 2010.

ation circuit is inductive and capacitive respectively. The impedance matching network ensures the resistive components of the antenna and rectification circuit are matched while the reactive components are the complex conjugates of each other [72][75].

The perfect rectenna, from the energy harvesting prospective, should have high voltage gain across a wide resonance bandwidth. Matching the impedance of the receiving antenna and the rectification circuit helps to increase the voltage gain. The level of resonance is measured by a dimensionless quantity called the quality factor:

$$Q = \frac{f_c}{\Delta f} \tag{2.13}$$

where

Q is the quality factor that measures the level of resonation of a rectenna

f_c is the resonant frequency or the centre frequency of operation, Hz

Δf is the 3 dB resonance bandwidth, Hz

The relationship between the quality factor, the voltage gain and bandwidth of a rectenna is shown in Figure 2.32. Together with the mathematical relationship demonstrated in (2.13), it is apparent that high voltage gain and wide resonance bandwidth cannot be achieved simultaneously by a rectenna. The decision on how to configure the system should be made according to the requirements of individual application.

Antenna design

Different types of antennae have their own characteristics. There are many parameters, such as the voltage gain, bandwidth and dimension that need to be considered. The choice of a particular type of antenna could also be influenced by the constraint(s) and requirement(s) of a specific application. Several common types of antennae are discussed in this section.

(a) Microstrip antenna

Microstrip antenna uses meandering lines, either in regular shapes or in fractal

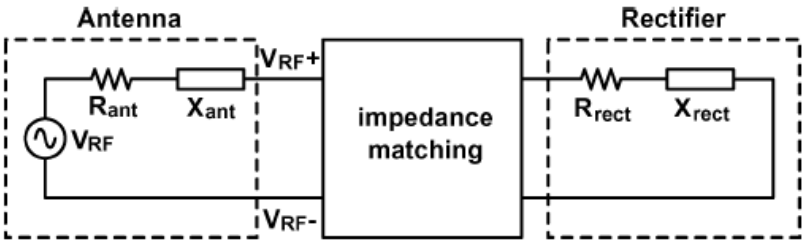

Figure 2.31: Constituent parts of a rectenna [75] © IEEE 2008.

V_{RF} is the voltage (AC) of the input signal to the antenna
R_{ant} represents the resistive element of the antenna impedance
X_{ant} represents the reactive element of the antenna impedance
R_{rect} represents the resistive element of the rectifier impedance
X_{rect} represents the reactive element of the rectifier impedance

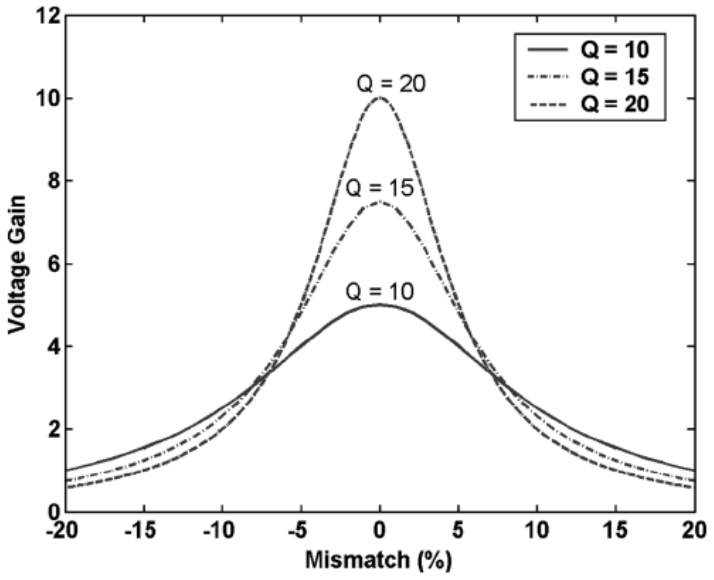

Figure 2.32: Relationship between the quality factor, the gain and bandwidth of a rectenna [75] © IEEE 2008.

patterns, to run up its active length to the half wavelength of the RF signal it wants to couple with [76]. It can be fit onto a small piece of printed circuit board (PCB).

The exposed tracks makes the adjustment of resonance frequency very convenient as the impedance matching network can be connected to any point on the meandering lines easily. The height of a microstrip antenna is identical to the thickness of the PCB that the antenna has been printed on. Microstrip antenna would be a good choice if the overall volume occupied by the device is the predominant concern. Besides in energy harvesting, this type of antenna is also widely used in RFID applications [77, 78].

A microstrip antenna that only occupies a surface area of about 150×20 mm^2 (6×0.8 square inches) is shown in Figure 2.33. This antenna is designed to couple with 900 MHz signal. The output characteristics of the rectenna, which consists of the microstrip antenna shown in Figure 2.33 and a well-matched rectification circuit, is shown in Figure 2.34. The waveform in Figure 2.34 shows that the highest voltage gain this rectenna can achieve is 6.5. However, it also confirms that microstrip antenna has a narrow bandwidth and can only have one resonant frequency at any given time.

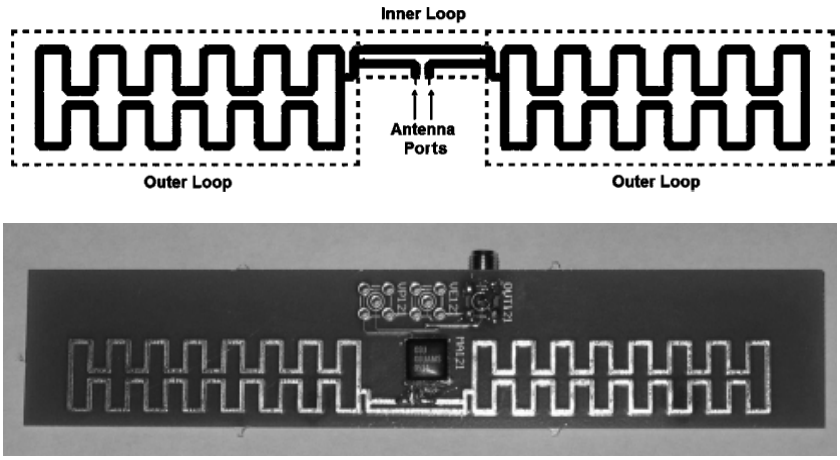

Figure 2.33: A microstrip antenna made of exposed meander lines on a PCB [75] © IEEE 2008.

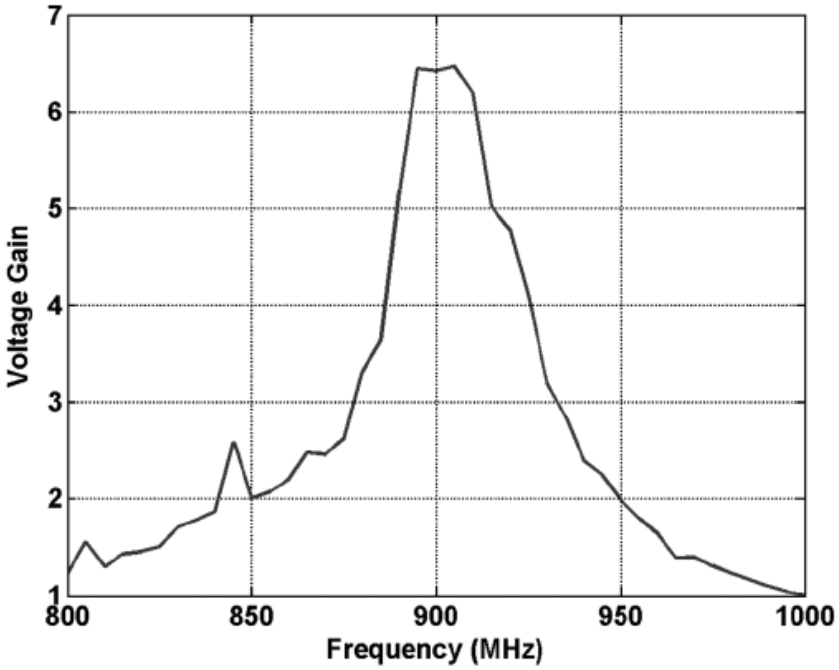

Figure 2.34: Voltage gain of a rectenna consists of a microstrip antenna and a well-matched rectifier [75] © IEEE 2008.

(b) Folded shorted patch antenna

The simplest form of folded shorted patch antenna (FSPA) consists of a patch plane in parallel with a ground plane. The patch plane can be further folded, as shown in Figure 2.35, into a vertically meandering structure. The overall height is less than 20 mm. The dimension parameters of this FSPA are specified in Table 2.4.

A shorting post connects the original patch in the middle level to the ground plane. The shorting post is used for fine tuning the resonant frequency of the FSPA. This is realised by changing the position of the connecting point of the shorting post on the patch plane [80]. The return loss between 600 MHz and 1.2 GHz is shown in Figure 2.36. The voltage gain of the antenna is the mirror image of the return loss along the x-axis.

The FSPA shown in Figure 2.35 has two folded patches of different sizes. Both the simulation and measurement results show this antenna has two resonant frequencies. According to the measurement result, the peak gains are 3.9 dBi[1] and 6.3 dBi at 867 MHz and 953 MHz respectively. The response curves of these two resonant frequencies superimpose on each other. It helps the FSPA to maintain the low profile characteristic while achieve a wider bandwidth than microstrip antenna [79].

Another advantage of FSPA is flexibility. Besides changing the position of the shorting post, the resonant frequency (or frequencies if appropriate) can also be modified by altering the direction of the opening slot(s) of the folded patch plane(s) or reducing the surface area(s) on the patch plane(s) by introducing air gap(s) [81]. These modifications could be made without altering the overall dimensions of a FSPA.

[1] 'dBi' is the forward gain of an antenna in comparison with a hypothetical isotropic antenna, which receives/distributes energy uniformly in all direction, that has the same resonant frequency.

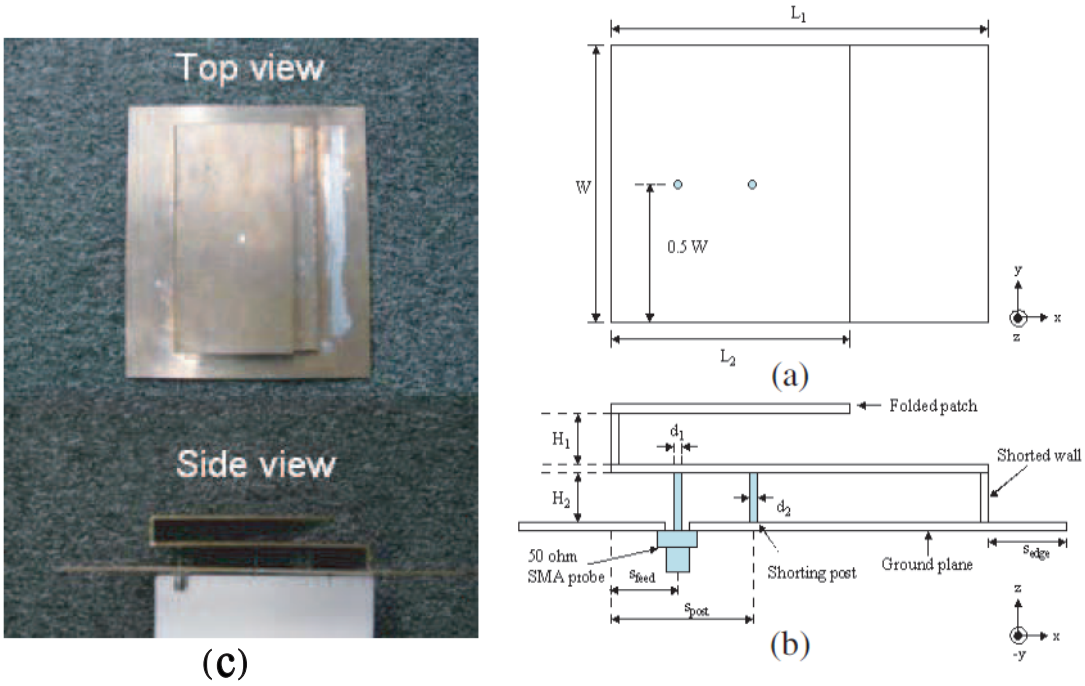

Figure 2.35: Folded shorted patch antenna (a) top view drawing, (b) side view drawing, (c) top view and side view of the FSPA [79] © EMP 2010.

Table 2.4: Dimensions of the FSPA [79].

Parameter	Dimension (mm)
H_1	8.0
H_2	8.0
d_1	1.3
d_2	1.3
W	125.0
L_1	90.0
L_2	73.0
S_{post}	7.5
S_{feed}	47.5
S_{edge}	35.0

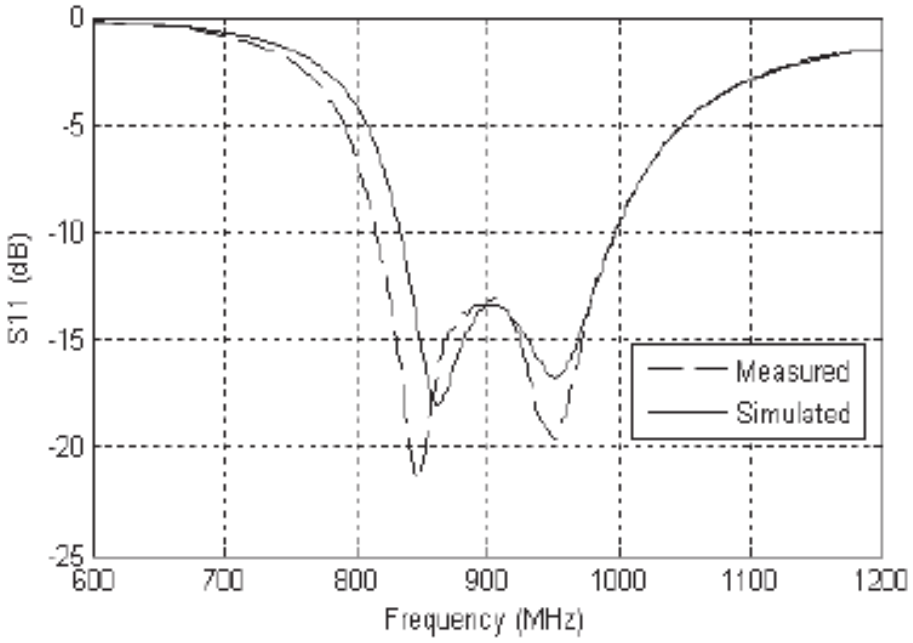

Figure 2.36: Return loss of the FSPA [79] © EMP 2010.

(c) Spiral antenna

FSPA could have a wider (high gain) bandwidth than mircostrip antenna, but its spectrum is still too narrow to couple with multiple high power density RF signals simultaneously. It is highly desirable for an antenna to be able to couple with several high power density RF signals.

Spiral antenna is capable of coupling with RF signals than span across several hundred mega-hertz (MHz) [71]. A typical spiral antenna is shown in Figure 2.37. It is housed on a 72 cm^2 PCB. The spectrum response from 600 MHz to 3.0 GHz is presented in Figure 2.38. This antenna is able to couple with multiple high power density RF signals simultaneously.

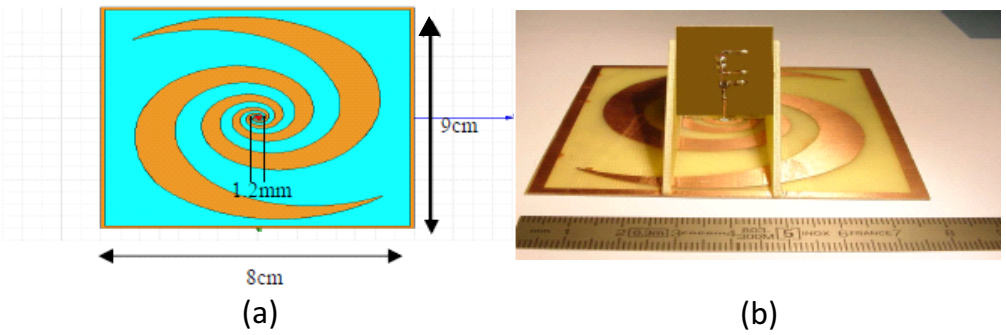

Figure 2.37: Spiral antenna: (a) dimensions, (b) connects to a rectification circuit [71] © ICREPQ 2010.

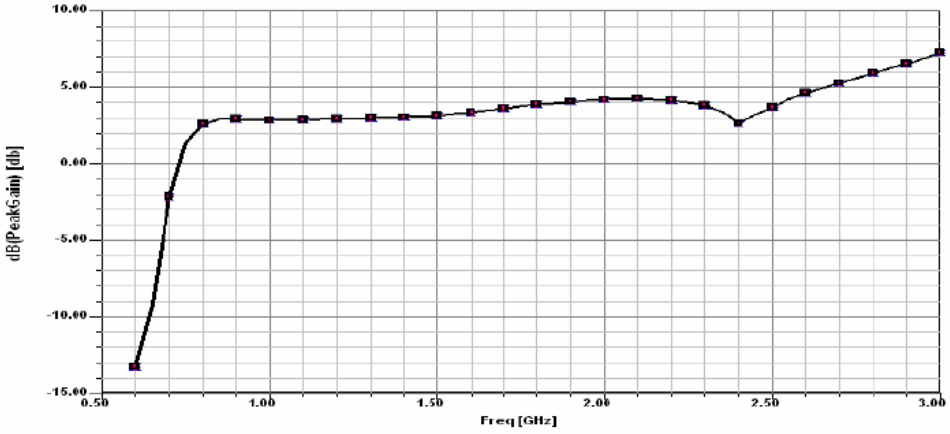

Figure 2.38: Spectrum response of the spiral antenna from 600 MHz to 3.0 GHz [71] © ICREPQ 2010.

(d) Multi-retennae array

Spiral antenna, as shown in Figure 2.38, has a wide bandwidth. But each passively operated match network can only be tuned to one frequency at a time. This problem is mitigated by the creation of a multi-rectennae array. A multi-rectennae array is shown in Figure 2.39. Every matching network is tuned to a particular frequency.

This kind of arrangement occupies a larger space but it increases the effective aperture of the receiving antenna [74, 82]. Any type and any number of retenna can be put into the array as long as it is practical to do so. Larger amount of energy could be harvested if more retennae are allowed to form an array.

Rectification circuit

The primary function of the rectification circuit to convert the energy harnessed by the harvesting device into DC output. The minimum level of the output voltage should be the same as the operation voltage of the application load. The

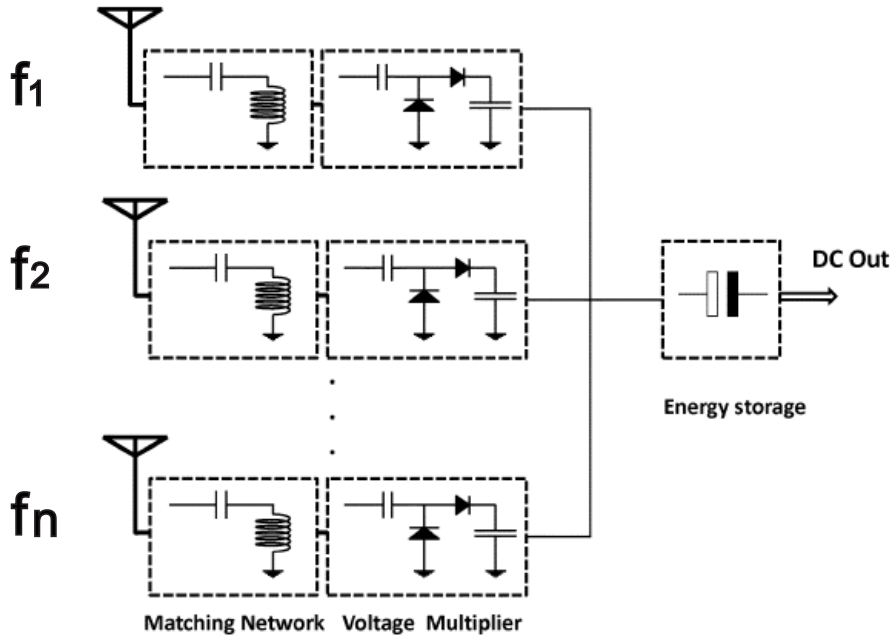

Figure 2.39: A multi-rectennae array with each matching circuit tuned to a particular frequency [82] © IEEE 2012.

DC output can be used to power the application load or charge up the energy storage capacitor.

The input voltage is typically in AC and its level is usually much lower than the operation voltage of the application load. Besides the AC to DC conversion, the rectification circuit is often required to boost the voltage level of the DC output. The circuit diagram of a voltage doubler is shown in Figure 2.40. V_{RF} is the input from the antenna. V_{DCout} is the output of the voltage doubler. V_{DCin} connects to the ground if the voltage multiplier has only one stage. When V_{DCin} is connecting to the ground, current will flow through diode D_2 during the negative half cycle V_{RF}. The voltage across C_1 at the negative peak equals to V_{RF-} + V_{th2} (V_{th2} is the threshold voltage of diode D_2). The voltage across C_1 at the positive peak equals to V_{RF+} - V_{RF-} - V_{th2}. Assuming V_{RF+} and V_{RF-} are equal in amplitude but opposite in polarity, the voltage across C_2 would equal to $2|V_{RF}|$ - V_{th2} - V_{th1} (V_{th1} is the threshold voltage of diode D_1). The increase in voltage, V_{DCout} - V_{DCin}, is likely to be more than the total forward voltage drop of the two diodes.

Voltage multiplier usually consists of several voltage doublers. Figure 2.41 shows how multiple voltage doublers are cascaded together to form a multi-stage voltage multiplier. At the first stage, V_{DCin} connects to the ground. In all subsequent stages, V_{DCin} connects to the voltage doubler output from the previous stage.

Higher output voltage could be obtained by connecting more stages together. However, every voltage doubler has two capacitors. The reactive component of the total impedance, X_{rect}, will rise if the number of stages increases. It will lead to a bigger impedance mismatch the antenna and the rectification circuit. The quality factor will decrease. Therefore, the number of stages in a voltage multiplier is a compromise between producing a sufficiently high output voltage and maintaining the value of the quality factor at a desirable level.

Diodes, or diode-like components, are used to convert the input into DC output. The threshold voltage, also known as the forward voltage, is the minimum potential difference required to create a conducting path between the anode and cathode of a diode. The conversion efficiency can be improved by reducing the threshold voltage (V_{th}) of the diodes. Zero bias Schottky diodes and floating gate transistors have the lowest forward bias among diode-like components [74]. A

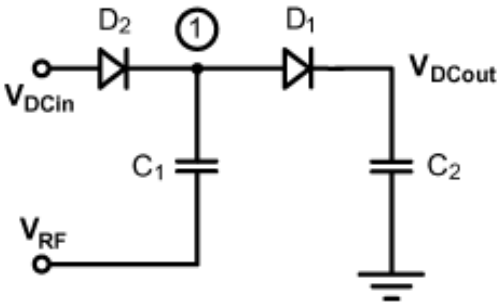

Figure 2.40: Diagram of a voltage doubler circuit [75] © IEEE 2008.

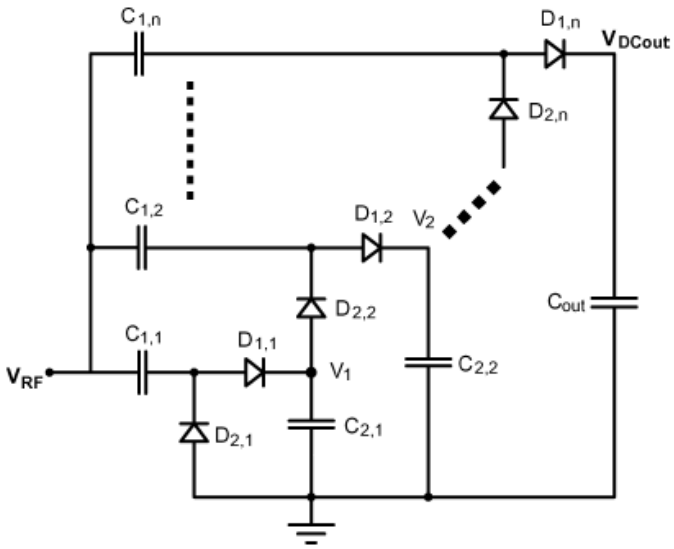

Figure 2.41: Diagram of a multi-stage voltage multiplier circuit [75] © IEEE 2008.

typical zero bias Schottky diode has a forward voltage drop of 50 mV, 100 mV and 200 mV if the forward current is 0.01 mA, 0.1 mA and 1 mA respectively [83]. The threshold voltage of floating gate transistor can be reduced to a few tens of millivolts [75].

MOSFETs[2] are used to substitute the diodes and capacitors. The circuit diagram of a floating gate transistor pack is shown in Figure 2.42(a). The gate of a PMOS transistor, M_1, connects to the gate of a diode-tied transistor, C_{g1}. The

[2]MOSFET = Metal Oxide Semiconductor Field Effect Transistor

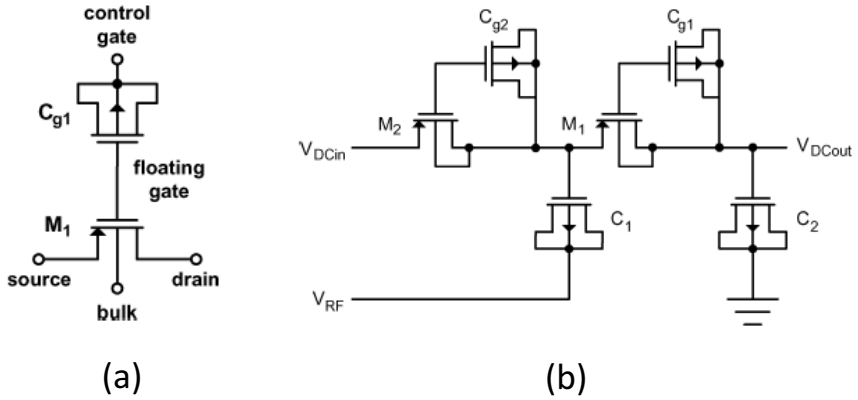

Figure 2.42: (a) A floating gate transistor pack (b) A voltage doubler with each stage consists of a floating gate transistor pack and a MOS capacitor [75].

threshold voltage of the gate-source junction of M_1 is determined by the amount of charge trapped in the floating gate. Injecting more charges into the floating gate will reduce the gate-source junction forward voltage of M_1.

The circuit diagram of a voltage doubler is shown in Figure 2.42(b). The diodes are replaced by floating gate transistor packs while the traditional capacitors are substituted by MOS capacitors. A MOSFET-based voltage multiplier can be made by cascading several MOSFET-based voltage doubler together. MOSFET-based voltage multiplier can be fabricated as an integrated circuit. It helps to minimise the power consumed during the conversion process and deliver more energy to the load [84].

2.6 Summary

This chapter outlines the fundamental theory and recent advancement of various topics in the field of energy harvesting. Each type of energy harvesting device is designed, in general, to be suited to harness energy from a particular energy source. Therefore, the energy source(s) presented in the ambient environment would determine what type(s) of harvesting device(s) should be used in the particular location.

The primary objective of this study is to harvest energy in high voltage AC air-insulated substations. The voltage level and operation frequency of an electricity

grid are carefully maintained. Both the strength and behavioural characteristics of the electric fields are stable. These advantageous features make harvesting energy from electric fields particularly attractive. The next few chapters will investigate the electric fields in air-insulated substations and explore how to harvest energy efficiently from the electric fields.

Bibliography

[1] MICAz datasheet, Wireless Sensor Network, ACEINNA Inc, Massachusetts, USA.

[2] E. Yeatman, Advances In Power Sources For Wireless Sensor Nodes, *Proc. Internationl Workshop on Wearable and Implantable Body Sensor*, 2004.

[3] S. Rogerson, Unleash Your Inner Energy, *IEE Power Engineer*, pp. 40-41, April/May 2005.

[4] L. Collins, Harvest For The World, *IEE Power Engineer*, pp. 34-37, February/March 2006.

[5] B. Holmes, The Power Within, *New Scientist*, pp. 30-34, 25th August 2007.

[6] R. Morais, S. Matos, M. Fernandes, A. Valente, S. Soares, P. Ferreira, M. Reis, Sun, Wind and Water Flow as Energy Supply for Small Stationary Data Acquisition Platforms, *Journal of Computers and Electronics in Agriculture*, Vol. 64, pp. 120-132, April 2008. ScienceDirect, Elsevier.

[7] N. Shenck and J. Paradiso, Energy Scavenging with Shoe-Mounted Piezoelectrics, *IEEE Micro*, pp. 30-42, May-June 2001. IEEE Computing Society.

[8] J. Rocha, L. Goncalves, P. Rocha, M. Silva and S. Lanceros-Mendez. Energy Harvesting From Piezoelectric Materials Fully Integrated in Footwear, *IEEE Transaction on Industrial Electronics*, Vol. 57, No. 3, pp. 813-819, March 2010.

[9] S. Roundy, P. Wright and J. Rabaey, A Study of Low Level Vibrations as A Power Source for Wireless Sensor Nodes, *Journal of Computer Communications*, Vol. 26, pp. 1131-1144, 2003. ScienceDirect, Elsevier.

[10] P. Mitcheson, E. Yeatman, G. Rao, A. Holmes and T. Green, Energy Harvesting From Human and Machine Motion for Wireless Electronic Devices, *Proceedings of IEEE*, Vol. 96, No. 9, September 2008.

[11] History of Piezoelectricity, Piezo System Inc, Massachusetts, USA.

[12] S. Roundy and P. Wright, A Piezoelectric Vibration Based Generator for Wireless Electronics, *Journal of Smart Materials and Structures*, Vol. 13, pp. 1131-1142, 2004. Institute of Physics (UK) Publising.

[13] T. Starner, Human-powered wearable computing, *IBM Systems Journal*, Vol, 35, Nos. 3 and 4, pp. 618-629, 1996.

[14] S. Priya and S. Nahm, Lead-Free Piezoelectrics, ISBN: 978-1-4419-9597-1, 2012. Springer

[15] Power-Generating Floor, East Japan Railway, Tokyo, Japan.

[16] Pavegen LIVE, Pavegen Systems Ltd, London, UK.

[17] D. Khadilkar, Energy-Harvesting Street Tiles Generate Power from Pavement Pounder, *Scientific American*, April, 2013.

[18] Piezoelectric Products & Evaluation Kits, Mide Technology, Massachusetts, USA.

[19] N. Muralidharan, M. Li, R. E. Carter, N. Galioto and C. L. Pin, Ultralow Frequency Electrochemical-Mechanical Strain Energy Harvester Using 2D Black Phosphorus Nanosheets, *ACS Energy Letters*, pp. 1797-1803, Vol.2, July 2017. American Chemical Society.

[20] C. Featherston, K. Holford and B. Greaves, Harvesting Vibration Energy for Structural Health Monitoring in Aircraft, *Key Engineering Materials*, Vol. 413-414, pp. 439-446, June 2009. Trans Tech Publications, Switzerland.

[21] S. P. Beeby, R. N. Torah, M. J. Tudor, P. Glynne-Jones, T. O'Donnell, C. R. Saha and S. Roy, A Mirco Electromagnetic Generator for Vibration Energy Harvesting, *Journal of Micromechancics and Microengineering*, Vol. 17, pp. 1257-1265, June 2007. Institute of Physics (UK) Publising.

[22] E. P. James, M. J. Tudor, S. P. Beeby, N. R. Harris, P. Glynne-Jones, J. N. Ross and N. M. White, An Investigation of Self-Powered Systems for Condition Monitoring Applications, *Sensors and Actuators A*, Vol. 110, pp. 171-176, 2004. Elsevier Science Direct

[23] R. Dayal, S. Dwari and L. Parsa, A New Design for Vibration-Based Electromagnetic Energy Harvesting Systems Using Coil Inductance of Microgenerator, *IEEE Trans. on Industry Applications*, Vol. 47, No. 2, pp. 820-830, March/April 2011.

[24] D. Maurath, P. Becker, D Spreemann and Y. Manolis, Efficient Energy Harvesting with Electromagnetic Energy Transducers Using Active Low-Voltage Rectification and Maximum Power Point Tracking, *IEEE Journal of Solid-State Circuits*, Vol. 47, No. 6, June 2012.

[25] A. Rahimi, Ö. Zorlu, A. Muhtaroglu and H. Külah, Fully Self-Powered Electromagnetic Energy Harvesting System With Highly Efficient Dual Rail Output, *IEEE Sensors Journal*, Vol. 12, No. 6, June 2012.

[26] D. Zhu, S. Beeby, M. Tudor and N. Harris, Electromagnetic Vibration Energy Harvesting Using An Improved Halbach Array, *Proc. of International Conference on Micro and Nanotechnology for Power Generation and Energy Conversion Applications (PowerMEMS)*, pp. 251-254, Atlanta, US, Dec 2012.

[27] J. Kraus and D. Fleisch, Electromagnetics with Applications, 5th edition, ISBN: 0-07-116429-4, 1999, McGraw-Hill.

[28] J. C. Mallinson, One-Sided Fluxes - A Magnetic Curiosity?, *IEEE Trans. on Magnetics*, Vol. 9, Issue 4, pp. 678-682, Dec 1973. Digitised version published on Jan 2003.

[29] D. Zhu, S. Beeby, M. Tudor and N. Harris, Vibration Energy Harvesting Using the Halbach Array, *Smart Materials and Structures*, Vol. 21, No. 7, pp 20-31, June 2012.

[30] VEH Vibration Energy Harvester Datasheet, Perpetumm Ltd, Southampton, UK.

[31] S. Roundy and E. Takahashi, A Cost-Effective Planar Electromagnetic Energy Harvesting Transducer, *Proc. of International Conference on Micro and Nanotechnology for Power Generation and Energy Conversion Applications (PowerMEMS)*, pp. 10-13, Atlanta, US, Dec 2012.

[32] B. Stark, P. Mitcheson, P. Miao, T. Green, M. Yeatman and A. Holmes, Converter Circuit Design, Semiconductor Device Selection and Analysis of Parasitics for Micropower Electrostatic Generators, *IEEE Trans. on Power Electronics*, Vol. 21, No. 1, Jan 2006.

[33] M. Lallart, S. Pruvost and D. Guyomar, Electrostatic energy harvesting enhancement using vaiable equivalent permittivity, *Physics Letter A*, Vol. 375, pp. 3921-3924, Sep 2011. Elsevier Science Direct.

[34] E. Cantatore and M. Ouwerkerk, Energy Scavenging and Power Management in Networks of Autonomous Microsensors, *Journal of Microelectronics*, Vol. 37, pp. 1584-1590, Aug 2006. Elsevier Science Direct.

[35] P. Basset, D. Galayko, F. Cottone, R. Guillemet, E. Blokhina, F. Marty and T. Bourouina, Electrostatic Vibration Energy Harvester with Combined Effect of Electrical Nonlinearities and Mechanical Impact, *Journal of Micromechanics and Microengineering*, Vol. 24, pp. 1-14, Feb 2014. Institute of Physics (UK) Publising.

[36] R. Wang, F. Gu, R. Cattley and A. D. Ball, Modelling, Testing and Analysis of a Regenerative Hydraulic Shock Absorber System, *Energies*, Article No. 386, Vol. 9, May 2016. MDPI AG.

[37] N. Roscoe and M. Judd, Harvesting Energy From Magnetic Fields to Power Condition Monitoring Sensors, *IEEE Sensors Journal*, Vol. 13, Issue 6, pp. 2263-2270, June 2013.

[38] Power Donut 3 Instrumentation Platform Brochure, Underground Systems Inc., Connecticut, USA.

[39] E. Velmre, Thomas Johann Seebeck (1770-1831), *Proc. of Estonian Academy of Science and Engineering*, Vol. 13, Issue 4, pp. 276-282, Oct 2007.

[40] Brief History of Thermoelectrics, CalTech Material Science, California Institute of Technology, USA.

[41] Sir William Thomson Baron Kelvin of Largs, University of Glasgow Story, Glasgow, UK.

[42] M. Kishi, H. Nemoto, T. Hamao, M. Yamamoto, S. Sudou, M. Mandai and S. Yamamoto, Micro-thermoelectric modules and their application to wristwatches as an energy source, *Proc. 18th International Conference on Thermoelectrics*, pp. 301-307, IEEE, Baltimore, USA, Aug-Sep 1999.

[43] Why Use Bi_2Te_3, Micropelt GmbH, Frieburg, Germany.

[44] Perodic Table of Elements, Royal Society of Chemistry, UK.

[45] M. Dresselhaus, G. Chen, Z. F. Ren, G. Dresselhaus, A. Henry and J. P. Fleurial, New composite thermoelectric materials for energy harvesting applications, *JOM*, Vol. 61, No. 4, pp. 86-90, Apr 2009. Springer.

[46] R. Venkatasubramanian, C. Watkins, D. Stokes, J. Posthill and C. Caylor, Energy harvesting for electronics with thermoelectric devices using nanoscale materials, *Proc. Electronic Device Meeting IEDM 2007*, pp. 367-370, IEEE International, Washington DC, USA, Dec 2007.

[47] T. Huesgen, P. Woias and N. Kockmann, Design and fabrication of MEMS thermoelectric generators with high temperature efficiency, *Sensor and Actuators A*, pp. 423-429, Vol. 145-146, Dec 2007. Elsevier Science Direct.

[48] G. Nolas, J. Sharp and H. Goldsmid, Thermoelectrics: Basic Principles and New Material Developments, *Springer Series in Materials Science*, ISBN-13: 978-3540412458, Aug 2001. Springer.

[49] The Top Graphene Facts, University of Manchester, Manchester, UK.

[50] GRAPHENE: Graphene-Based Revolutions in ICT and Beyond, The Graphene Flagship, Chalmers University of Technology, Gothenburg, Sweden.

[51] E. Koukharenko, X. Li, I. Nandhakumar and M. J. Tudor, Towards nano-structured thermoelectric generator for energy harvesting, *Proc. PowerMEMS 2007*, pp. 145-148, Frieburg, Germany, Nov 2007.

[52] H. Sevinçli, C. Sevik, T. Çagin and G. Cuniberti, A bottom-up route to enhance thermoelectric figures of merit in graphene nanoribbons, *Scientific Reports 3*, Article Number 1228, Feb 2013. Nature Publishing Group.

[53] J. Carmo, L. Gonçalves and J. Correia, Thermoelectric microconverter for energy harvesting systems, *IEEE Trans. on Industrial Electronics*, pp. 861-867, Vol. 57, No. 3, Mar 2010.

[54] L. Mateu, C. Codrea, N. Lucas, M. Pollak and P. Spies, Human body energy harvesting thermogenerator for sensing applications, *Prco. International Conference on Sensor Technologies and Applications*, pp. 366-372, Valencia, Spain, Oct 2007.

[55] Thin Film Thermogenerators and Sensing Devices, Micropelt GmbH, Frieburg, Germany.

[56] L. Mateu, C. Codrea, N. Lucas, M. Pollak and P. Spies, Energy harvesting for wireless communication systems using thermogenerators, *Proc. 21st Conference on Design of Circuits and Integrated Systems (DCIS)*, Barcelona, Spain, Nov 2006.

[57] E. Carlson, K. Strunz and B. Otis, A 20 mV input boost converter with efficient digital control for thermoelectric energy harvesting, *IEEE Journal of Solid-State Circuits*, pp. 741-750, Vol. 45, No. 4, Apr 2010.

[58] TE-CORE6 and TE-CORE7 Thermoharvesting Power Module, Micropelt GmbH, Frieburg, Germany.

[59] G. C. Navone, M. Plissonier, C. Salvi, I. Chartier, T. Lanier and Y. Breton, Electrical power generation from knitted textile using the body heat, *Proc. PowerMEMS Conference*, pp. 311-314, Freiburg, Germany, Nov 2007.

[60] S. J. Kim, J. H. We and B. J. Cho, A wearable thermoelectric generator fabricated on a glass fabric, *Journal of Energy and Environmental Science*, pp. 1959-1965, Issue 6, Mar 2014. Royal Society of Chemistry.

[61] D.Samson, M. Kluge, Th. Becker and U. Schmid, Wireless sensor powered by aircraft specific thermoelectric energy harvesting, *Sensor and Actuators A*, pp. 240-244, Vol. 172, Dec 2010. Elsevier Science Direct.

[62] M. R. Pearson, M. J. Eaton, R. Pullin, C. A. Featherston and K. M. Holford, Energy harvesting for aerospace structural health monitoring systems, *Journal of Physics: Conference Series*, p. 012025, Vol. 382, No. 1, Aug 2012. Institute of Physics Publishing (UK).

[63] K. Thangaraj, A. Elefsiniots, Th. Becker, U. Schmid, J. Lees, C. A. Featherston and R. Pullin, Energy storage options for wireless sensors powered by aircraft specific thermoelectric energy harvester, *Research Journal of Microsystem Technologies*, pp. 701-707, Vol. 20, Issue 4-5, Apr 2014. Springer.

[64] A. Dolgov, R. Zane and Z. Popovic, Power Management system for Online Low Power RF Energy Harvesting Optimisation, *IEEE Trans. on Circuits and Systems - I: Regular Papers*, pp. 1802-1811, Vol 57, No. 7, Jul 2010.

[65] T. Sogorb, J. V. Llario, J. Pelegri, R. Lajara and J. Alberola, Studying the Feasibility of Energy Harvesting from Broadcast RF Station for WSN, *Proc. IEEE International Instrumentation and Measurement Technology Conference*, Victoria, Canada, May 2008.

[66] H. Nishimoto, Y. Kawahara and T. Asami, Prototype Implementation of Ambient RF Energy Harvesting Wireless Sensor Networks, *Proc. IEEE Sensors 2010 Conference*, pp. 1282-1287, Hawaii, USA, Nov 2010.

[67] E. D. Mantiply, K. R. Pohl, S. W. Poppell and J. A. Murphy, Summary of measured radiofrequency electric and magnetic fields (10 kHz to 30 GHz) in the general and work environment, *Journal of Bioelectromagnetics*, pp. 563-577, Vol. 18, Issue 8, May 1997. Wiley-Liss.

[68] UK Frequency Allocation Table 2017, The Office of Communications, London, UK.

[69] Mobile Phone Base Stations – How Mobile Phone Networks Work, The Office of Communications, London, UK.

[70] Mobile Infrastructure Sharing, Groupe Speciale Mobile Association, London, UK.

[71] D. Bouchouicha, F. Dupont, M. Latrach and L. Ventura, Ambient RF Energy Harvesting, *Proc. International Conference on Renewable Energies and Power Quality (ICREPQ) 2010*, pp. 1-5, Granada, Spain, Mar 2010.

[72] H. Jabbar, Y. S. Song and T. T. Jeong, RF Energy Harvesting System and Circuits for Charging of Mobile Devices, *IEEE Trans. on Consumer Electronics*, pp. 247-253, Vol. 56, No. 1, Feb 2010.

[73] M. Arrawatia, M. S. Baghini and G. Kumar, RF Energy Harvesting System from Cell Towers in 900 MHz Band, *Proc. National Conference on Communications (NCC) 2011*, Bangalore, India, Jan 2011. Published by IEEE.

[74] S. A. Bhalerao, Powering Wireless Sensor Nodes using Ambient RF Energy, *Proc. IEEE International Conference on Systems, Man and Cybernetics*, pp. 2695-2700, Taipei, Taiwan, Oct 2006.

[75] T. Le, K. Mayaram and T. Fiez, Efficient Far-Field Radio Frequency Energy Harvesting for Passively Powered Sensor Networks, *IEEE Journal of Solid-State Circuits*, Vol. 43, No. 5, May 2008.

[76] M. Zeng, A. S. Andrenko, X. Liu, Z. Li and H. Tan. A Compact Fractal Loop Rectenna for RF Energy Harvesting, *IEEE Antennas and Wireless Propagation Letters*, pp. 2424-2427, Vol. 16, July 2017.

[77] M. Mi, M. H. Mickle, C. Capelli and H. Swift, RF Energy Harvesting with Multiple Antennas in the Same Space, *IEEE Antennas and Propagation Magazine*, pp. 100-106, Vol. 47, No. 5, Oct 2005.

[78] N. C. Karmakar, Handbook of Smart Antennas for RFID Systems, ISBN: 1118074394, Feb 2011. John Wiley & Sons.

[79] Z. W. Sim, R. Shuttleworth, M. J. Alexander and B. D. Grieve, Compact Patch Antenna Design for Outdoor RF Energy Harvesting in Wireless Sensor Networks, *Progress In Electromagnetics Research*, pp. 273-294, Vol. 105, 2010. EMW Publishing.

[80] P. Li, K. L. Lau and K. M. Luk, Wideband folded shorted patch antenna with low profile, *IEEE Electronics Letters*, pp. 112-113, Vol. 41, No. 3, Feb 2005.

[81] A. Holub and M. Polivka, Vertically meander-folded shorted-patch antennas, *Microwave and Optical Technology Letters*, pp. 2938-2942, Vol. 51, No. 12, Dec 2009. Wiley Periodicals.

[82] P. Nintanavongsa, U. Muncuk, D. R. Lewis and K. R. Chowdhury, Design Optimisation and Implementation for RF Energy Harvesting Circuits, *IEEE Journal on Emerging and Selected Topics in Circuits and Systems*, Vol. 2, No. 1, Mar 2012.

[83] HSMS-2852 Surface Mounted Zero Bias Schottky Detector Diodes Datasheet, Broadcom Inc, California, USA.

[84] T. Paing, E. Falkenstein, R. Zane and Z. Popovic, Custom IC for Ultra-Low Power RF Energy Harvesting, *Proc. 24th Annual IEEE Applied Power Electronics Conference and Exposition (APEC) 2009*, pp. 1239-1245, Washington DC, USA, Feb 2009.

Chapter 3

Electric fields in air-insulated substations

3.1 A brief introduction of electric fields

The most elementary electrical quantity is the electron charge (q_e). Electron charge has a nominal value of -1.60×10^{-19} coulomb (C). Every object carries multiple units of electron charge. This relationship is represented by:

$$Q = N \times q_e \tag{3.1}$$

where

Q is the total amount of electric charge carried by an object, C

N is the number of electron carried by an object

q_e is the electron charge, $|q_e| = 1.60 \times 10^{-19}\ C$

Coulomb's law states that two point charges separated by a distance will exert a force on each other [4]. This relationship is represented by:

$$F = \frac{Q_1 Q_2}{4\pi\varepsilon r^2} \times r \tag{3.2}$$

where

F is the force exerted by both charges onto each other, N

Q_1 is one of the two point charges, C

Q_2 is the other point charge, C

ε is permittivity of the space between the two point charges, Fm^{-1}

r is the distance between the two point charges, m

According to the Coulomb's Law, the electric fields between the two point charges are defined as force per unit charge. The strength of the electric fields between the two point charges could be obtained by dividing (3.2) with one of the charges. Therefore, the strength of the electric fields is derived from (3.3).

Electric fields are the manifestation of the electrostatic force. The amount of work that could be done by the electrostatic force is the product of the distance travelled by the charge against the electric fields. This relationship is represented by (3.4). Since work can only be done if there is energy, it indicates that energy exists in electric fields. Measuring the electric fields in air-insulated substations helps to identify locations with the most potential for energy harvesting.

$$E = \frac{F}{Q_2} = \frac{Q_1}{4\pi\varepsilon_0 r^2} \times r \tag{3.3}$$

$$W = Q\Delta V = QE\Delta x = F\Delta x \tag{3.4}$$

where

E is the strength of the electric fields between the two charges, N/C or V/m

W is the amount of work that has done by moving the charge against the electric fields by a certain distance, J

ΔV is the potential difference between the starting point and the end point of the movement of charge Q, V

Δx is the distance where charge Q has moved, m

3.2 Measuring the strength of electric fields

3.2.1 Electric fields in the centre of a test rig/facility

There are three components (x, y and z) in the three-dimensional Cartesian system. The overall field strength at any given position is the orthogonal combination of all three components. An instrument that is capable of performing the orthogonal combination can be placed at any position to conduct the field strength measurement. If the overall field strength at a particular position is dominated by one component, it is justified to use an instrument that has been purposefully designed to measure the dominate component.

The IEEE 644-1994 standard establishes the procedure for measuring the electric and magnetic fields induced by power lines and specifies the accuracy requirement of the equipment. The nominal tolerance is $\pm 10\%$ [2].

The experimental setup for measuring the electric fields in the centre of the test rig is shown in Figure 3.1. The white circular block with smooth edge is the high voltage (HV) electrode. It is supported by four circular plastic posts. The HV electrode and the ground plane are 50 cm (0.5 m) apart. The HV electrode is connected to a HV transformer. This transformer has a maximum output voltage of 50 kV.

However, the HV probe that was used to measure the output voltage of the transformer has a rating of 20 kV AC. HV probe with higher rating was not available. Therefore the output voltage of the transformer was restricted to below the rating of the HV probe.

The HV probe divides the input by 1000. The output of the HV probe is displayed by a Fluke-73 digital multimeter. The cable that connects the output of the transformer to the HV electrode has a rating of 10 kV AC. If the transformer and the HV electrode is connected by an exposed conductor, the electric fields in the centre of the test rig could be influenced by the exposed conductor.

For safety purposes, the voltage supplied to the HV electrode was increased from 0 kV to 10 kV in 1 kV steps. To obtain the field strength, the readings on the multimeter are first multiplied by 1000 and then divided by the distance that separates the HV electrode and the ground plane. The results have been plotted on a graph shown in Figure 3.2. The vertical component (z) overwhelmingly

dominates the overall field strength.

Commercially available instrument, such as the Narda EFA-300 field analyser set, is designed to measure the strength of the electric and magnetic fields according to the requirements specified in the IEEE 644-1994 standard [3]. A dedicated electric fields sensor, as shown in Figure 3.1, is placed at the centre of the test rig.

The measurements obtained by the sensor is transmitted to the field analyser handset via a piece of optical fibre cable. It ensures the accuracy of the reading as the output signal of the sensor and the electric fields in the centre of the test rig will not distort each other. This set of results has been plotted on the same graph in Figure 3.2.

The sensor itself has a height of approximately 10 cm. The vertical component dominates but the horizontal components (x and y) also have some influences. Due to the converging effect, the readings from the Narda instrument are slightly higher than the field strength calculated from dividing the applied voltage by separation distance. However, as shown in Figure 3.2, the discrepancy between both sets of results is less than 10%. This is inside the tolerance range specified by the IEEE 644-1994 standard. It confirms the accuracy of the field strength calculated from dividing the applied voltage by separation distance. Quasi-uniform electric fields exist in the centre of the test rig.

3.2.2 A purposefully designed sensor for measuring field strength

Specialised instrument is not always available in short notice. In order to be able to carry out field survey without undue delay, a separate sensor has been made. It is shown in Figure 3.3. This purposefully designed field strength sensor, because of its shape, will be referred to as the circular field sensor.

The circular field sensor consists of two metallic plates of 10 cm in radius. They are 10 cm apart. The circuit diagram in Figure 3.3 shows an 100 kΩ resistor is placed between the plates. The central conductor of the coaxial cable connects to the upper terminal of the resistor while the shield of the coaxial cable connects to the lower terminal of the resistor. The voltage across the resistor can be measured by an oscilloscope or a multimeter.

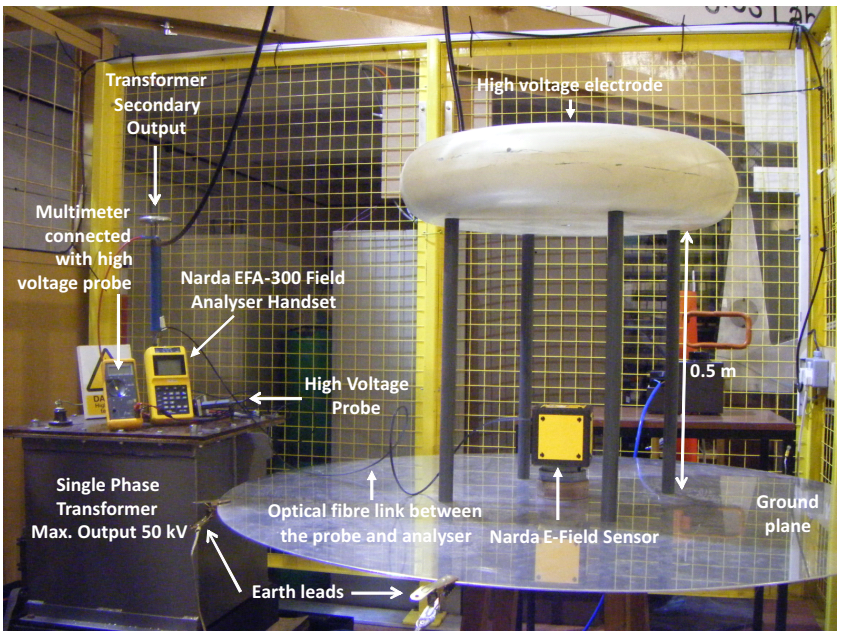

Figure 3.1: Experimental setup for measuring the strength of the electric fields in the centre of the test rig.

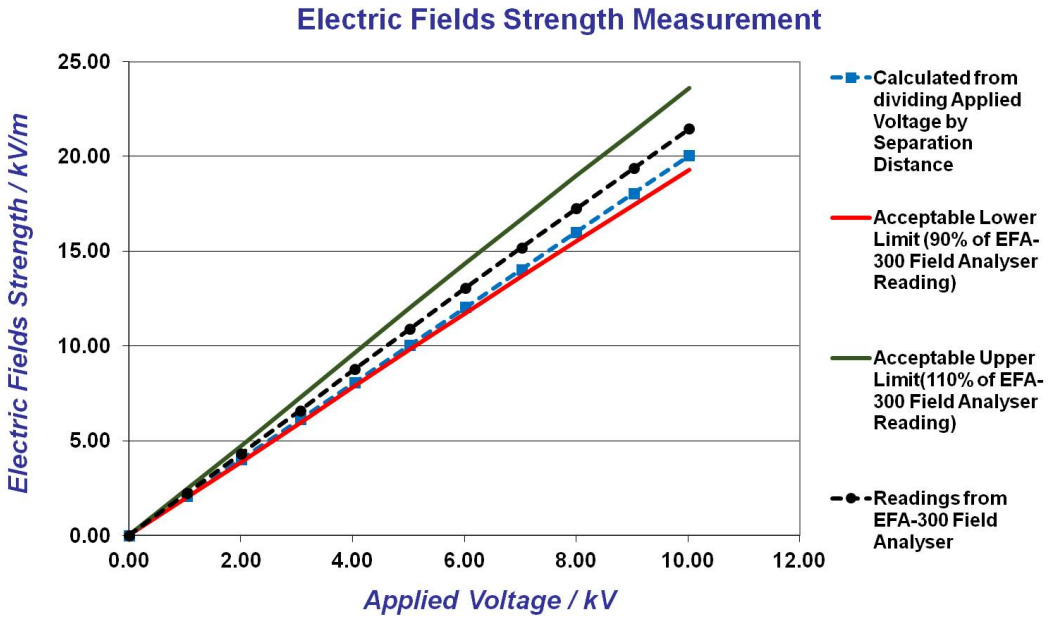

Figure 3.2: Field strength measurement result obtained by commercially available instrument in the centre of the test rig.

Putting in a large resistor between the two plates, such as 1 MΩ or above, would be equivalent to keep them in open circuit condition permanently. The voltage across the resistor would change very little if the field strength only alters by a few kilovolt per meter. Resistors in the order of a few kilo-ohm need to have unpractically high power rating if the instrument encounters electric fields in the region of a few tens of kilovolt per meter. Resistance from 1 kΩ to 1 MΩ have been tested. The 100 kΩ resistor with a power rating of 0.5 W was chosen because it is sensitive enough to respond to any modest change in field strength while doesn't easily get burned.

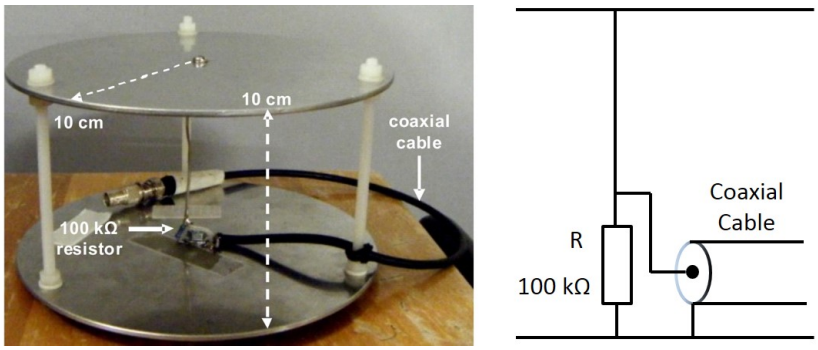

Figure 3.3: A purposefully designed field strength sensor and its schematic circuit diagram.

3.2.3 Theoretical analysis of the circular field sensor

The circular field sensor consists of two parallel circular plates. Figure 3.4 shows the open circuit and short circuit scenarios when two parallel plates are placed inside quasi-uniform electric fields. The open circuit voltage between the two plates can be calculated by:

$$V_{oc} = E \times d = \frac{V_0}{h} \times d \tag{3.5}$$

where

E is the strength of the electric fields, kV/m

V_{oc} is the open circuit voltage between the plates, kV

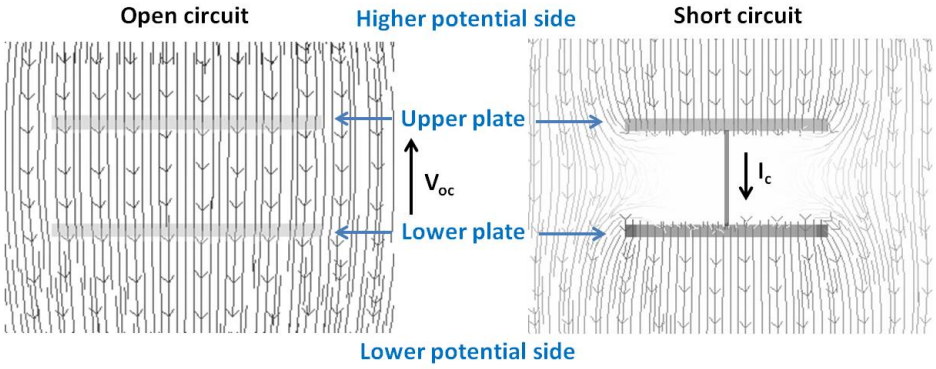

Figure 3.4: Two parallel plates inside quasi-uniform electric fields: left - under open circuit condition, right - under short circuit condition.

V_0 is the 50 Hz AC high voltage source, kV
d is the distance between the upper and lower plates, m
h is the distance between the high voltage electrode and the ground, m

Potential difference exists between the upper plate and the lower plate under open circuit condition. The induced charge will re-align immediately after both plates establish electrical contact. The movement of the induced charge generates a short current burst. This moment is illustrated in Figure 3.5. The electrostatic induction phenomenon and charge transfer arrangement will be discussed in greater detail in Chapter 4.

The circular field sensor is shown to be floating in mid-air in Figure 3.5. This is purely for illustration purpose. In reality, the circuit field sensor will be placed above a solid space. Therefore, the distance between the high voltage electrode and the upper plate is far greater than the distance between the lower plate and the ground plane ($h - d \gg d'$). The influence of the distance between the lower plate and the ground plane on the amount of induced charge can be omitted.

The amount of charge induced on the each plate is calculated by:

$$q = DA = \varepsilon_0 EA = \frac{\varepsilon_0 V_0 A}{h - d} \tag{3.6}$$

The polarity of the induced charge on the upper plate is opposite to the the

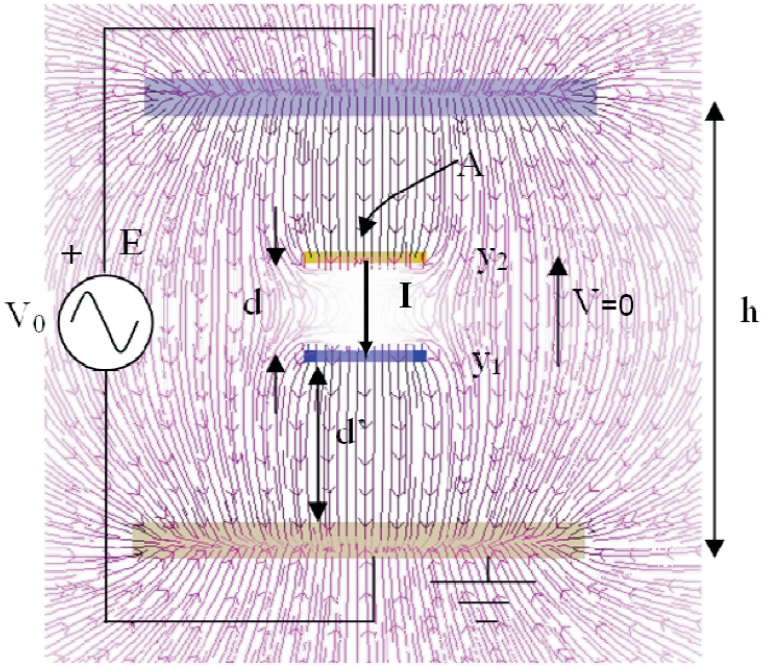

Figure 3.5: Illustration of the condition immediately after both plates have been short-circuited [4] © ISH 2007.

induced charge on the lower plate. Equal amount of induced charge will move in opposite direction when both plates establish electrical contact. The total amount of charge that could be exchanged between the upper and lower plates over half a mains frequency cycle is represented by:

$$2q = \int_0^{10ms} I_{max} sin(2\pi 50t)\ dt \tag{3.7}$$

The general formula for calculating the maximum short circuit current is obtained by further derived (3.7):

$$I_{max} = \frac{2q}{\int_0^{10ms} sin(2\pi 50t)\ dt} \tag{3.8}$$

The maximum short circuit current is obtained by executing the integration:

$$I_{max} = \frac{2q \times 100\pi}{2} = 100q\pi \tag{3.9}$$

The rms value of the short circuit current is calculated by substituting (3.6) into (3.9) and subsequently dividing the resultant equation with $\sqrt{2}$:

$$I_c = \frac{100\pi\varepsilon_0 V_0 A}{\sqrt{2}(h-d)} \quad [4] \tag{3.10}$$

The output voltage across the circular field sensor is obtained by:

$$V_c = I_c \times R_m = \frac{100\pi\varepsilon_0 V_0 A}{\sqrt{2}(h-d)} \times R_m = 0.626\pi^2 \times \frac{V_0}{(h-d)} \tag{3.11}$$

The strength of the electric fields between the high voltage electrode and the upper plate is calculated by (3.12) when both plates of the circular field sensors are connected together.

$$E = \frac{V_0}{(h-d)} \tag{3.12}$$

The relationship between the strength of the electric fields and the output voltage of the circular field sensor is represented by (3.13), which is derived by substituting (3.12) into (3.11).

$$V_c = 0.626\pi^2 E \iff E = \frac{V_c}{0.626\pi^2} \tag{3.13}$$

where

q is the amount of induced charge on either of circular plates, C

D is the flux density, C/m

A is the area of the circular plate, $A = \pi r^2$, m^2

π is the angle in radians

r is the radius of the circular plates, $r = 0.1\ m$ in this instance

ε_0 is the permittivity of vacuum, $8.85\ pF/m$

E is the strength of the electric fields, kV/m

V_0 is the 50 Hz AC high voltage source, kV

d is the distance between the upper and lower plates, m

h is the distance between the high voltage electrode and the ground, m

I_{max} is the maximum short circuit current, A

t is time, ms

I_c is the rms value of the short circuit current, A

R_m is the resistance between the two plates of the circular field sensor, Ω

V_c is the output voltage from the circular field sensor, mV

3.2.4 Calibrate the circular field sensor

The circular field sensor is tested, as shown in Figure 3.6, in the test rig. The output voltage of the circular field sensor is measured by a battery-powered voltmeter. The voltmeter is placed between the two circular plates to minimise interference. The theoretical output voltage of the circular field sensor is derived by (3.11).

Both sets of result are plotted in Figure 3.7. They both have a linear relationship with the strength of the electric fields but the measurement result is significantly and consistently larger than the theoretically derived result. The

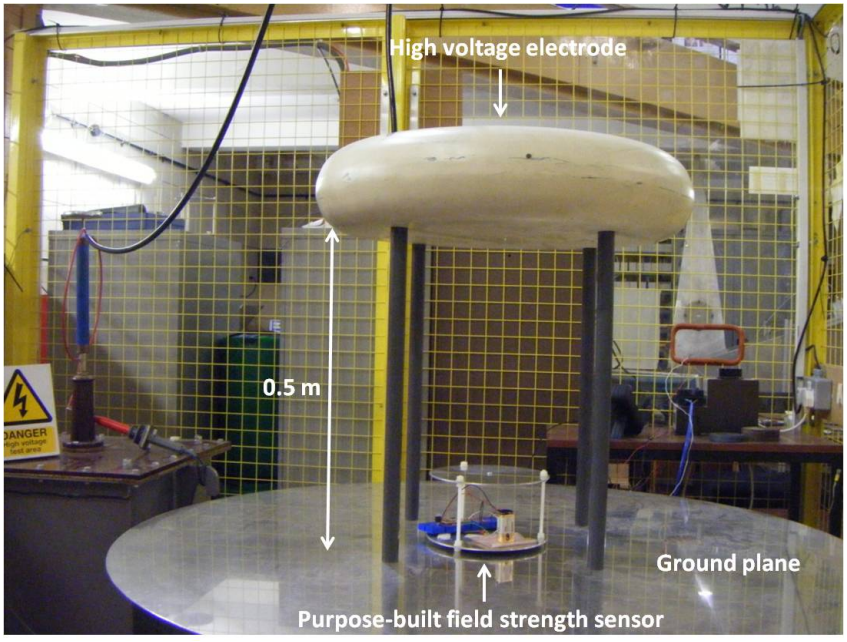

Figure 3.6: Circular field sensor sits in the centre of the test rig.

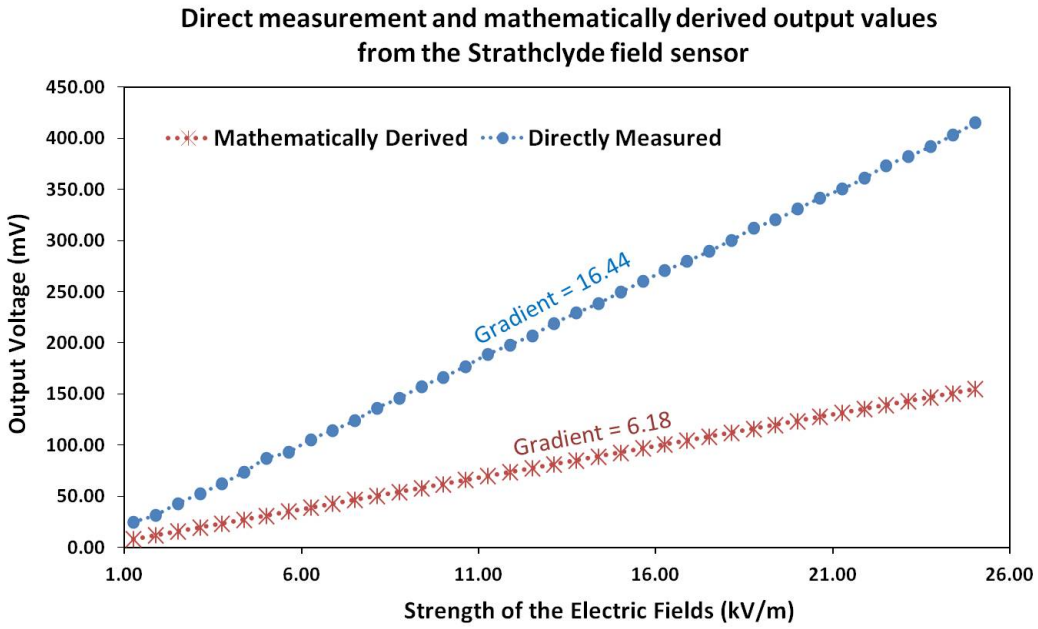

Figure 3.7: Directly measured and mathematically derived output voltage of the circular field sensor.

most likely cause is the converging effect in the immediate vicinity of the circular field sensor. The enlargement coefficient is calculated by:

$$K = \frac{\Delta V_m/\Delta E}{\Delta V_c/\Delta E} = \frac{V_m}{V_c} = \frac{16.44}{6.18} = 2.66 \implies V_c = \frac{V_m}{K} = \frac{V_m}{2.66} \tag{3.14}$$

The field strength is obtained by substituting (3.14) into (3.13):

$$E = \frac{V_m}{K \times 0.626\pi^2} = \frac{V_m}{1.67 \times \pi^2} \tag{3.15}$$

The height of the circular field sensor is one fifth of the distance between the HV electrode and the ground plane of the test rig. According to (3.12), the height of the circular field sensor would have a substantial impact to the result and should be taken into consideration:

$$E_s = 0.8 \times E = \frac{0.48 \times V_m}{\pi^2} \tag{3.16}$$

where

K is a dimensionless enlargement coefficient of the circular field sensor

V_m is the measurement reading of the output voltage from the circular field sensor, mV

V_c is the theoretical output voltage of the circular field sensor, mV

E is the field strength prediction obtained by the circular field sensor, kV/m

E_s is the field strength result adjusted to reflect the actual deployment condition, kV/m

3.2.5 Parametric study of the enlargement coefficient

A few pairs of metallic plates with different radii have been made to investigate the relationship between the dimension of the plates that make up the circular field sensor and the enlargement coefficient. They have been put into different positions. The experimental parameters are shown in Table 3.1.

The voltage applied onto the HV electrode increases from 0 V to 10 kV with an incremental step of 1 kV. The experimental setup is similar to what is shown in Figure 3.6. The output voltage of the circular field sensors have been measured. The results are shown in Figure 3.8 and Figure 3.9.

The graphs in Figure 3.8 show that, in general, smaller plate has bigger fringe effect than larger plate. The enlargement coefficient tends towards unity as the dimension of the plate gets bigger. The dimension of the plate has an inverse exponential relationship with the enlargement coefficient. The graphs in Figure 3.9 suggest that keeping the circular field sensor close to the ground plane helps to reduce the enlargement coefficient.

When the circular field sensor is being used inside an air-insulated substation, it can only be positioned in a place that satisfies the relevant minimum clearance

Table 3.1: Experimental parameters for investigating the enlargement effect.

Plate radius (cm)	min 2.5 - max 15.0, step size = 2.5
Distance to ground (cm)	min 2.5 - max 10.0, step size = 2.5

limit. The height of the circular field sensor is negligibly small in comparison to the clearance between the exposed high voltage apparatus and the upper plate of the circular field sensor. The height of the circular field sensor has little influence on the measurement result.

3.3 Field surveys in air-insulated substations

3.3.1 Review of field surveys conducted by other studies

Numerous studies have taken field strength measurements in and around high voltage overhead lines and electrical substations. The primary purpose of these surveys is to investigate health impact of exposure to power frequency electric fields. Some focus on the well beings of utility personnel [5, 6, 7], others pay more attention to the health concerns for residents living near high voltage electrical installations [8, 9].

Researchers in Finland use the Narda EFA-300 field analyser to carried out field surveys in eight 400 kV outdoor air-insulated substations [5, 6]. The field sensor was positioned at 1 meter above ground and supported by a wooden tripod. Measurements were taken at numerous locations such as underneath the over-cross of busbars, between the cophasal busbars and near the circuit breakers. Strong electric fields usually appear at 'a crossing of cophasal main and bay busabrs' [6]. Field strengths as high as 14.3 kV/m were recorded in one of the substations. This is higher than the human exposure limit recommended by the European Union, which is 10 kV/m [10].

Wireless sensors, of which the energy harvesting devices intend to power, are usually attached onto the surfaces of supporting structures or the exterior of the assets to be monitored. It is necessary to conduct surveys at locations where harvesting devices are likely to be installed.

3.3.2 Dedicated field surveys conducted in two air-insulated substations

Dedicated field surveys have been conducted in two air-insulated substations, one outdoor and one indoor. Two separate sets of measurement instruments, as shown

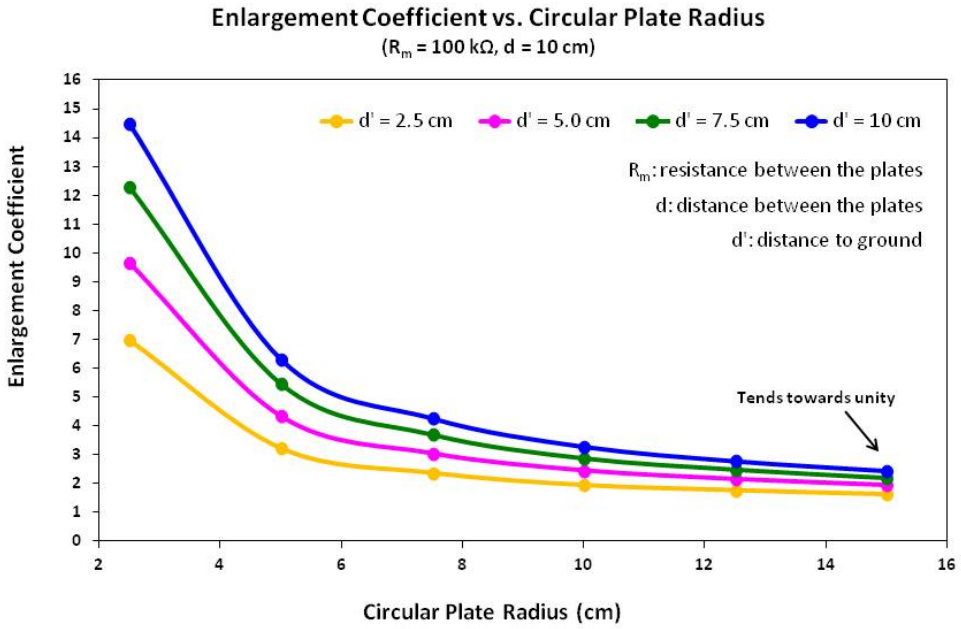

Figure 3.8: Relationship between the dimension of the plates and the enlargement coefficient.

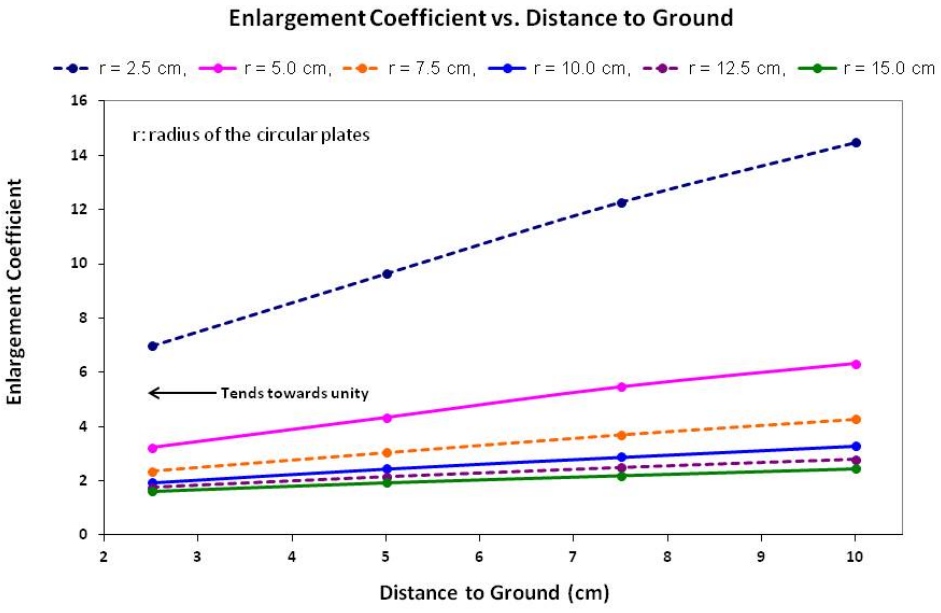

Figure 3.9: Relationship between the distance of the circular field sensor to ground and the enlargement coefficient.

in Figure 3.10, have been used to carry out the work. Measurements were taken at locations where harvesting devices can be installed while the substation remains online. The measurement results obtained in Bolney and Dungness are labelled as 'BE' and 'DE' respectively followed by a number.

(a) Bolney Substation

Bolney substation is located in West Sussex, approximately 16 miles south of London Gatwick Airport. It is a 400/132 kV air-insulated outdoor substation. It connects the 400 kV national transmission grid to the local 132 kV distribution network. The master plan of the substation is shown in Figure 3.11. Areas where measurements have been taken are:

- In one of the 132 kV sections of the substation that houses the capacitor bank 'MSC4'.
- Around the concrete support structure of the disconnectors and circuit breakers 'X410'.
- Around the concrete support posts along a section of the 400 kV busbar 'M1'.

Measurement points around the concrete support structure of the 400 kV disconnector 'X410' and the concrete support posts of the 400 kV busbar 'M1' are shown in Figure 3.12 and Figure 3.13 respectively. A selection of the measurement results obtained in this substation are shown in Table 3.2. They are taken by the Narda set.

Figure 3.10: Left - Narda EFA-300 field analyser set, Right - Circular field sensor. Both sets of instruments were used to measure the field strength at BE1 (please refer to Table 3.2 for the precise location).

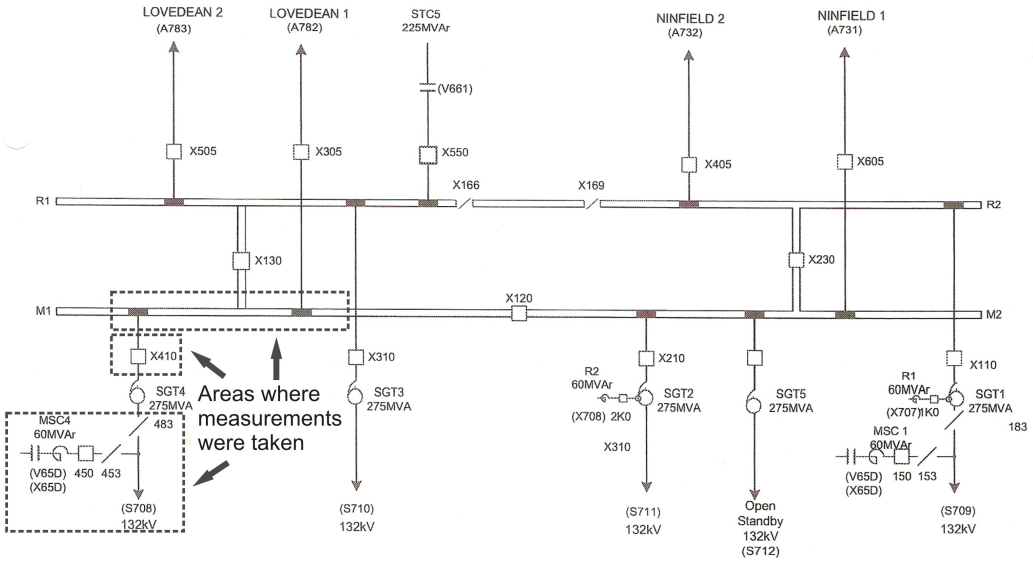

Figure 3.11: Master plan of the Bolney substation.

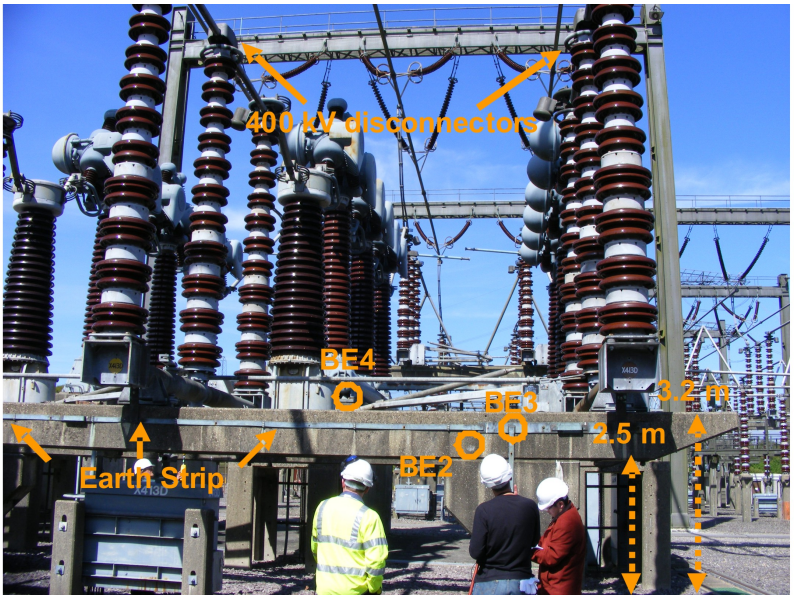

Figure 3.12: Measurement points around the concrete support structure of 400 kV disconnectors in Bolney substation.

Figure 3.13: Measurement points around the concrete support posts of 400 kV busbars in Bolney substation.

Table 3.2: A selection of the measurement results obtained in Bolney substation.

Measurement Locations	Field Strength (Unit: kV/m)	Label
The sensor sits on top of the static capacitor kiosk box in the 132 kV section.	12	BE1
The sensor touches the side surface of the concrete support structure of the 400 kV disconnectors.	11	BE2
The sensor is in the proximity of BE2 and in contact with the earthing strip.	30	BE3
The sensor sits on the concrete support structure of the 400 kV disconnectors.	25	BE4
The sensor touches the side surface of the concrete support structure of the 400 kV circuit breakers.	16	BE5
The sensor is in the proximity of BE5 and in contact with the earthing strip.	27	BE6
The sensor sits on the concrete support structure of a current transformer.	33	BE7
The sensor touches the side surface of the concrete support structure of a yellow phase 400 kV busbar, underneath the disconnector 'X506'.	57	BE8
The sensor is in the proximity of BE8 and in contact with the earthing strip.	≈100	BE9
The sensor is underneath the blue phase and in an equivalent position to BE9.	65	BE10

(b) Dungeness Substation

Dungeness substation is about 21 miles southeast of Ashford, on the coast of Kent. It is a 400/275 kV indoor air-insulated substation. The master plan of the substation is shown in Figure 3.14. Areas where measurements have been taken are:

- Around the concrete support structure of the 400 kV circuit breakers and disconnectors 'X2290'.
- In the vicinity of the underground cable entry points and the control box of the voltage transformer 'DUNGENESS B G22'.
- Along several concrete support posts on two different phases of the same section of the 400 kV busbar.

Measurement points around the concrete support structure of the circuit breakers 'X2290' and around the cable entry points of the substation are shown in Figure 3.15 and Figure 3.16 respectively. A selection of the measurement results obtained in this substation are listed in Table 3.3. They are also taken by the Narda set.

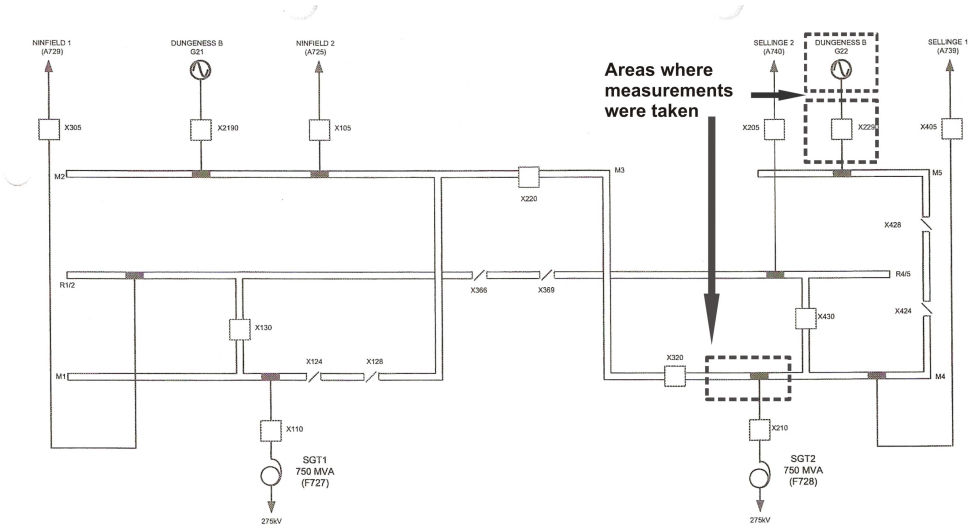

Figure 3.14: Master plan of the Dungeness substation.

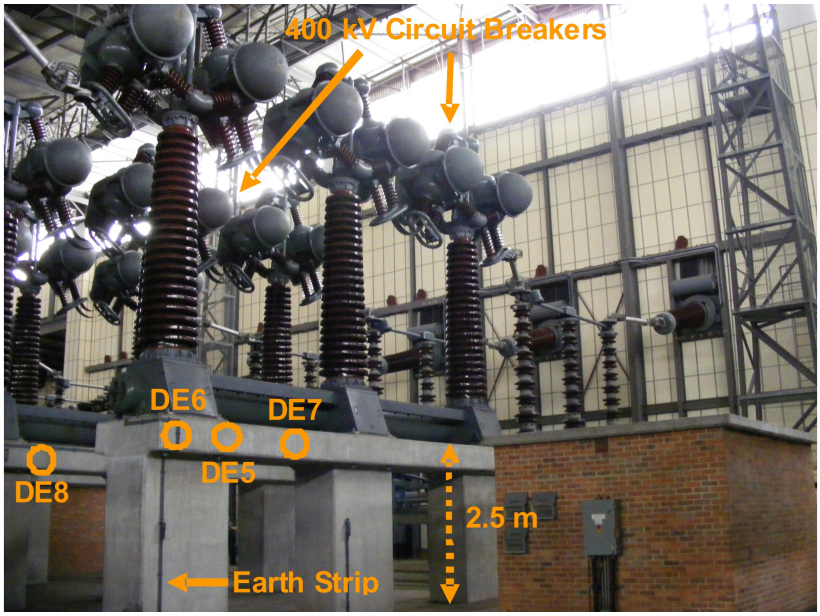

Figure 3.15: 400 kV circuit breakers and the concrete support structure in Dungeness with measurement positions DE5, DE6, DE7 and DE8 indicated.

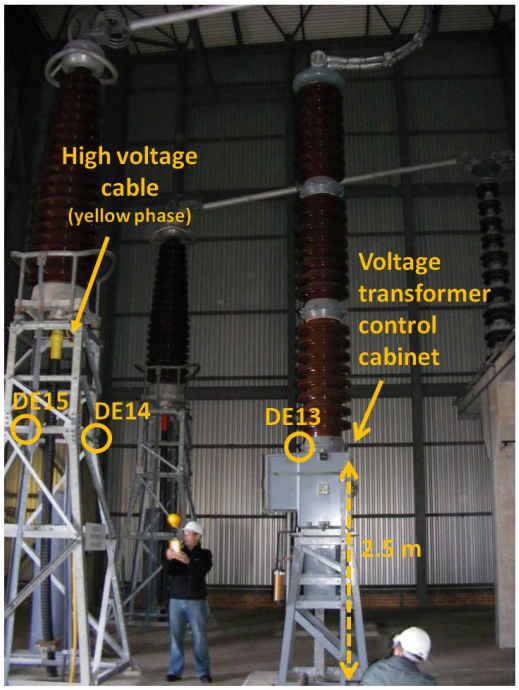

Figure 3.16: High voltage cable and voltage transformer control cabinet in Dungeness with measurement positions DE13, DE14 and DE15 indicated.

Table 3.3: A selection of the measurement results obtained in Dungeness substation.

Measurement Locations	Field Strength (Unit: kV/m)	Label
The sensor is underneath the yellow phase of a 400 kV busbar, close to the circuit breaker 'X210'.	63	DE1
The sensor is in the proximity of DE1 and in contact with the earthing strip.	97	DE2
The sensor is underneath the blue phase of a 400 kV busbar, close to the circuit breaker 'X210'.	56	DE3
The sensor is in the proximity of DE3 and in contact with the earthing strip.	90	DE4
The sensor is underneath a red phase 400 kV circuit breaker, it touches the side surface of the concrete support structure.	37	DE5
The sensor is in the proximity of DE5 and in contact with the earthing strip.	45	DE6
The sensor sits between two circuit breakers of the red phase.	31	DE7
The sensor is underneath the yellow phase and in an equivalent position to DE5.	23	DE8
The sensor is in the proximity of DE8 and in contact with the earthing strip.	30	DE9
The sensor is underneath a red phase 400 kV disconnector, it sits on the concrete support structure.	13	DE10
The sensor sits half way between the red and yellow phases on the concrete support structure of the 400 kV disconnectors.	22	DE11
The sensor is underneath the yellow phase and in an equivalent position to DE10.	15	DE12
The sensor sits on top of the voltage transformer control cabinet.	78	DE13
The sensor touches the structure that supports the high voltage cable.	9	DE14
The sensor is in the proximity of DE14 and in contact with the earthing strip.	30	DE15

(c) Compare the measurement results provided by two sets of instruments

The circular field sensor was also used to take measurements in both substations. The circular field sensor could be connected to either a digital multimeter, as shown in Figure 3.10, or a battery-powered oscilloscope, as seen in Figure 3.17.

An example of the output waveform of the circular field sensor is shown in Figure 3.18. The circular field sensor was at measurement point BE4. The rms value of the waveform is approximately 550 mV. The field strength of 26.2 kV/m is produced by substituting 550 mV as V_m into (3.16).

Besides field strength at BE4, results from several other measurement points are also presented in Table 3.4. The dominant component of the electric fields is perpendicular to the upper plate of the circular field sensor at all these locations. The difference between the corresponding results at each measurement point is less than ±10%. This is smaller than the maximum tolerance specified by the IEEE Standard 644-1994. Circular field sensor is able to provide a relatively accurate result in locations where the overall strength of the electric fields is dominated by the component that is perpendicular to its upper plate.

Table 3.4: A selection of measurement results obtained by two sets of instruments.

Location	Narda set (Unit: kV/m)	Circular field sensor (kV/m)	Within ±10% of each other? (Yes/No)
On the ground, underneath a 132 kV busbar.	2.0	2.2	Yes
BE1	12.0	13.1	Yes
BE4	25.0	26.2	Yes
DE11	22.0	20.1	Yes

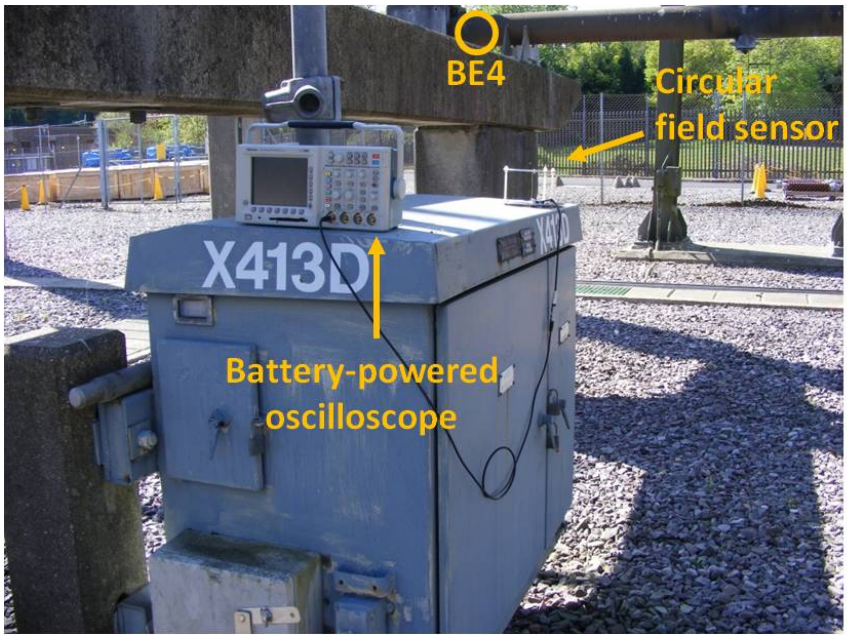

Figure 3.17: The circular field sensor connects to a battery-powered TDS 3054B oscilloscope.

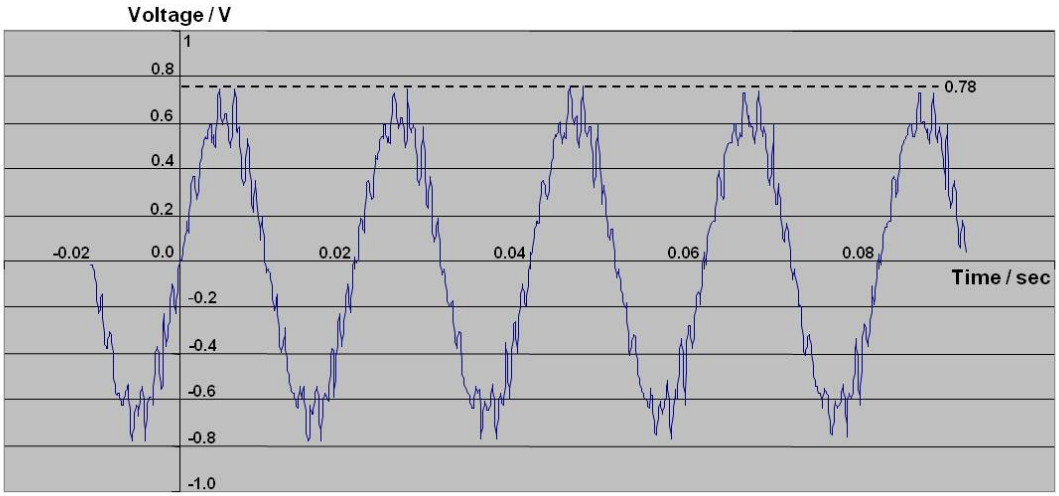

Figure 3.18: Output waveform of the circular field sensor captured by a battery-powered TDS 3054B oscilloscope at measurement point BE4.

(d) Interpretation of the survey results

The survey results obtained in Bolney and Dungeness substations suggest that strong electric fields can be found in locations directly underneath a long section of busbar, especially in the space immediately above the earthing strips/tapes. This is due to the converging effect of the field flux.

All the measurement locations are outside the statutory safety clearance and do not require an outage to gain access. Many of them have electric fields stronger than the highest field strength recorded in the Finnish study (14.3 kV/m). Locations with the best potential for energy harvesting are around the concrete support structures of the disconnectors and circuit breakers. These locations have higher than average electric fields and harvesting devices can be conveniently installed.

Bibliography

[1] J. Kraus and D. Fleisch. *Electromagnetics with Applications, 5th edition*, 1999, WCB/McGraw-Hill, ISBN 0-07-116429-4.

[2] IEEE Standards Association. *IEEE Standard 644-1994: Procedures for Measurement of Power Frequency Electric and Magnetic Fields From AC Power Lines*, 1995, E-ISBN: 0-7381-0362-4.

[3] EFA-300 Field Analyser Product Literature, Narda Safety Test Solutions GmbH, Pfullingen, Germany.

[4] A. Reid and M. Judd. A Novel Self-Powered Condition Monitoring Sensor for Harsh Environments - Feasibility Study, *Proc. 15th International Symposium on High Voltage Engineering - ISH 2007*, Ljubljana, Slovenia, August 2007.

[5] S. Kuusiluoma, T. Keikko, J. Hovila and L. Korpinen. Comparison of Electric and Magnetic Fields from Electric Power Systems with Exposure Recommendations of the European Union, *Proc. International Conference on Power System Technology - PowerCon 2000*, Vol. 2, Page 843 - 848, Perth, Australia, December 2000.

[6] J. Latva-Teikari, T. Karjanlahti, J. Kurikka-Oja, J. Elovaara, T. Långsjö and L. Korpinen. Measuring Occupational Exposure to Electric and Magnetic Fields at 400 kV Substations, *Proc. IEEE Transmission and Distribution Conference and Exposition*, Page 1 - 4, Chicago, USA, April 2008.

[7] D. Poljak, N. Kovac, C. Gonzalez, A. Peratta and S. Kraljevic. Assessment of Human Exposure to Power Substation Electric Field, *Proc. International Conference on Software in Telecommunications and Computer Networks - SoftCOM 2006*, Page 1 - 6, Split, Croatia, September 2006.

[8] H. Kirkham. Measuring Electric Fields from Power Lines: Part 1, *IEEE Instrumentation and Measurement Magazine*, Page 54 - 56, Vol. 9, Issue 3, June 2006.

[9] H. Kirkham. Measurment of Electric Fields Generated from Alternating Currnet, *IEEE Instrumentation and Measurement Magazine*, Page 58 - 61, Vol. 9, Issue 5, October 2006.

[10] Corrigendum to Directive 2004/40/EC of The European Parliament and of The Council of 29 April 2004 on the minimum health and safety requirements regarding the exposure of workers to the risks arising from physical agents (electromagnetic fields), *Official Journal of the European Union*, Vol. 47, L 184, ISSN 0378-6978, May 2004.

Chapter 4

Electric charge induction

4.1 Introduction

Electric current is the carrier of electrical energy. Electric current is produced by the movement of electrons. Each electron contains -1.60×10^{-19} C of electric charge. Therefore, the transfer of electrical energy is essentially the movement of electric charge.

More energy could be available if larger amount of charge is induced. A better understanding of the charge induction may help to increase the efficiency of the harvesting device. This chapter investigates the induction and transfer of electric charge in detail.

4.2 The process of charge induction

The surface potential of a metallic conductor, such as an aluminium plate, is zero in a field-free environment. Equal amount of positive and negative charges, as shown in Figure 4.1, is randomly distributed on the conductor. The conductor remains in electrical equilibrium state.

The bond between charges of opposite polarities will break down if the conductor is under the influence of electric fields. Charges will align, as illustrated in Figure 4.2, according to their polarities. The amount of charge on each conductor remains the same but the surface potential is no longer zero. The surface poten-

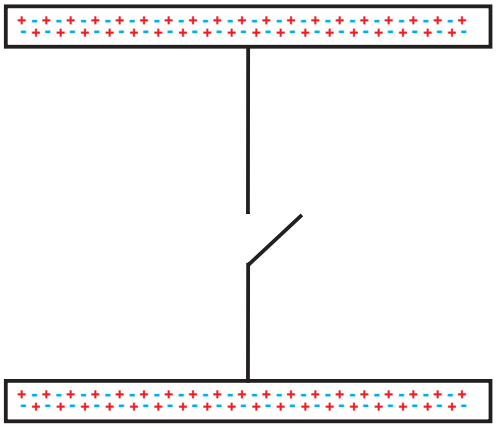

Figure 4.1: Charge alignment in a field-free environment.

tial of a conductor depends on its position in the relevant electric fields. This phenomenon is called electrification by electrostatic induction [1].

Charge transfer, as illustrated in Figure 4.3, takes place immediately after the switch between the two conductors closes. The short burst of current that flows between the two conductors is the manifestation of charge transfer. Figure 4.4 illustrates the charge induction and transfer during the positive half cycle of the AC supply.

The charge induction and transfer during the negative half cycle of the AC supply is very similar to the positive half cycle. The only difference, as shown in Figure 4.5, is the polarities of the corresponding induced charges. Both conductors become a single electrical entity when the switch is closed. Charges of opposite polarities will realign to reach a new electrical equilibrium. Surface potential reduces to zero. Surface potential will appear on the conductors again after the switch opens.

It is apparent that there are two segments of induced charge in every conductor. One segment stays on the conductor while the other can be transferred out of the conductor. One study makes use of these two terms: Poissonian induced charge and Laplacian induced charge. Poissonian induced charge is 'infrangibly linked' with the charge on an external body while Laplacian induced charge is 'associated with the change in conductor potential' [2, 3]. Current can only be generated when there is a potential difference between two conductors. Accordingly, the segment of induced charge that can be transferred out of the conductor is the Laplacian

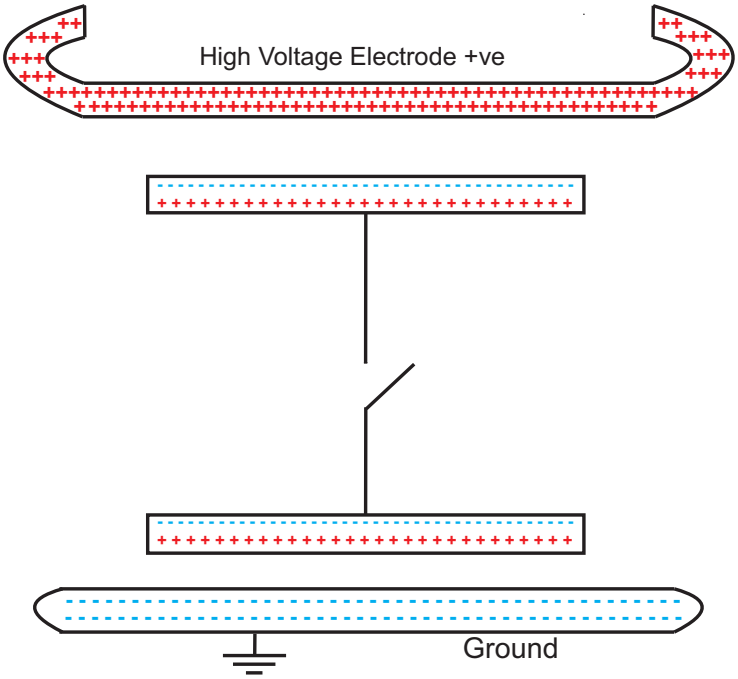

Figure 4.2: Charge alignment under open circuit condition during positive half cycles.

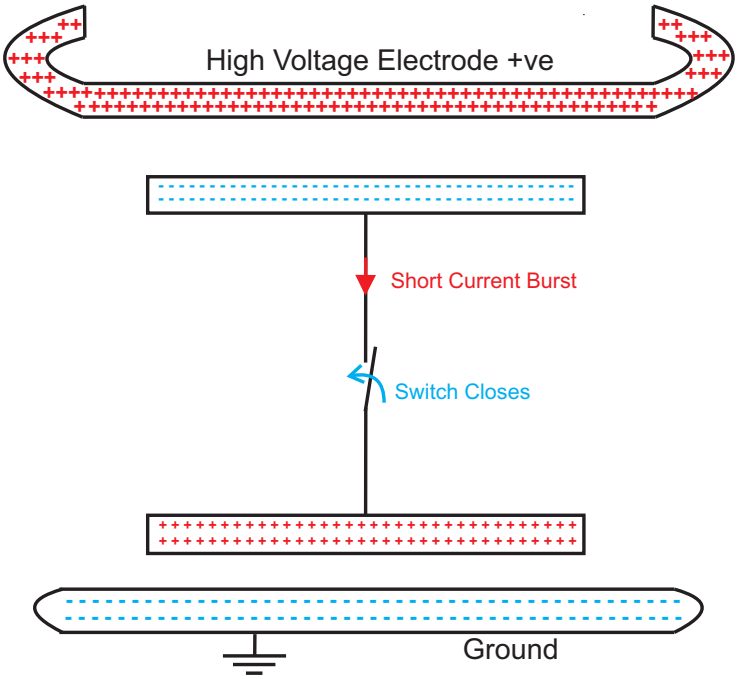

Figure 4.3: Charge alignment after the switch closes.

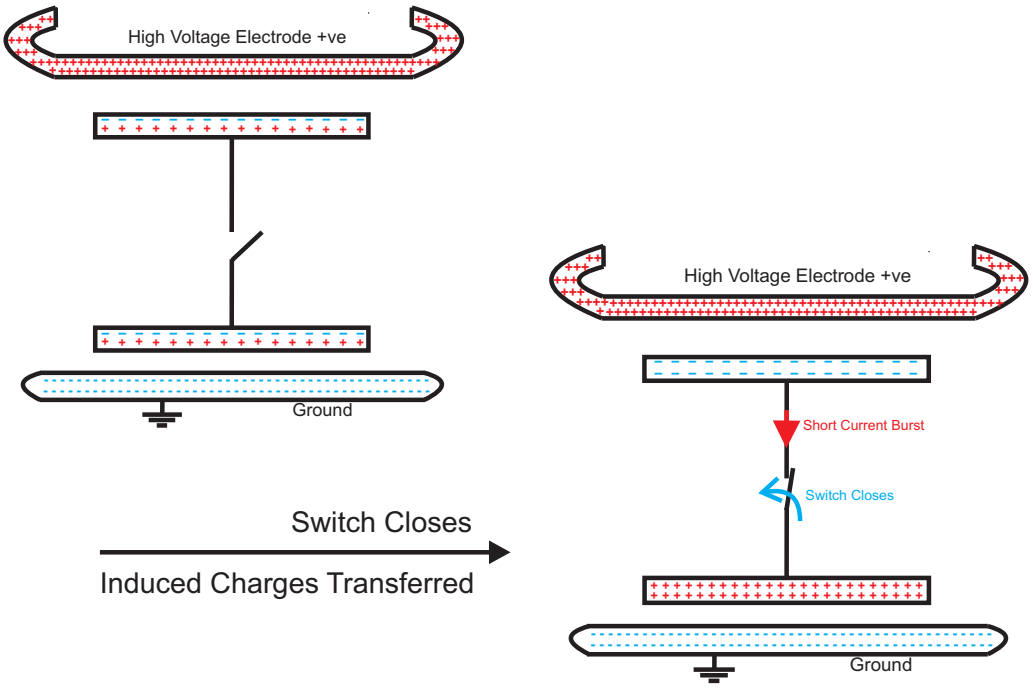

Figure 4.4: Charge induction and transfer during positive half cycles.

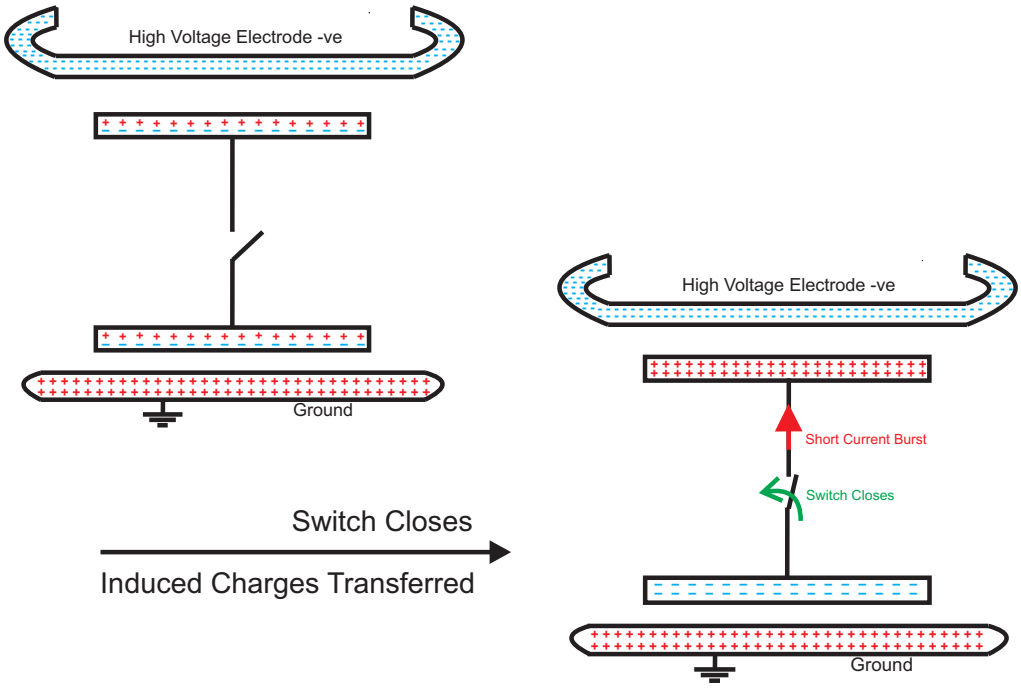

Figure 4.5: Charge induction and transfer during negative half cycles.

induced charge.

4.3 Estimate the amount of induced charge

4.3.1 Gauss's Law

Gauss's law states that the surface integral ($\oint$) of the flux density of the electric fields equals to the charge enclosed by that surface [4]. This is the amount of charge that can be extracted from the conductor. Assuming the immediate surrounding of the enclosed surface is air, the amount of charge on the enclosed surface is derived by:

$$Q = \oint_s D \bullet ds = \varepsilon_0 EA \tag{4.1}$$

where

Q is the amount of charge, C

D is the flux density, C/m^2, and $D = \varepsilon E$

ε_0 is permittivity of air, $8.85 \times 10^{-12}\ F/m$

E is the strength of the electric fields, V/m

A is the enclosed surface area, m^2, and $A = \oint_s \bullet\ ds$

4.3.2 Simulation setup

Computer simulation is a convenient way to quantify the amount of charge being induced on a conductor when it is 'immersed' in electric fields. Quickfield® is a finite element analysis software for electromagnetic, thermal and stress analysis. It has been used to conduct simulations in this study.

Simulation conducted by Quickfield can be set up under two different geometric models. One model is the three-dimensional Cartesian coordinate system (x, y and z). The cross-sectional shape of the object is drawn on the xy-plane. The object under investigation extends infinitely along the z-axis on both directions. Another model is the axisymmetric geometry system. This model treats the object as it would rotate around an axis by 360° [5]. For example, the right

angled isosceles triangle shown in Figure 4.6 is treated like a cone during the simulation. More objects can be accurately imitated when Quickfield uses the axisymmetric geometry model than the xy-plane coordinate geometry model. All the simulations in this study are conducted under the axisymmetric geometry model.

The induced charge within a enclosed surface is calculated using the line integral function, such as (4.1). The accuracy of the computation depends on the number of analytical nodes that covers the surface. The mesh spacing is set as default and 0.5 mm in Figure 4.6(a) and Figure 4.6(b) respectively. The corresponding induced charge on the inclined plane of the cone-shaped electrode is 1.610×10^{-9} C and 2.492×10^{-9} C. Smaller mesh spacing improves the accuracy of the simulation result since there are more analytical nodes to cover the same surface area. The degree of improvement in accuracy is greatly diminished while the time consumed to conduct the simulation is substantially lengthened if the mesh spacing is less than 0.5 mm. Therefore, all the simulations in this study set the mesh spacing at 0.5 mm.

The simulation result of the test rig on its own is shown in Figure 4.7. The field strength in the centre of the test rig and at locations immediately above the ground plane is approximately 10 kV/m. It closely imitates the quasi-uniform electric fields produce by the actual test rig. The simulation results could be trusted.

4.3.3 Optimal shape of the harvesting electrode

The harvesting electrode should ideally be able to induce large amount of charge while not causing any concern to the safe operation of the electricity grid. The objective of the investigative work is to find a shape that is best suited for the harvesting electrode.

The simulation parameters and the dimensions of the electrodes are listed in Table 4.1. The shapes that have been investigated are presented in Figure 4.8. They are circular plate, cone, frustum of cone and hemisphere. The radius or base radius of all the shapes is 5 cm. The height of the cone, frustum of cone and hemisphere is 5 cm. The height of the circular plate is considered to be too small to have any meaningful impact on the simulation result.

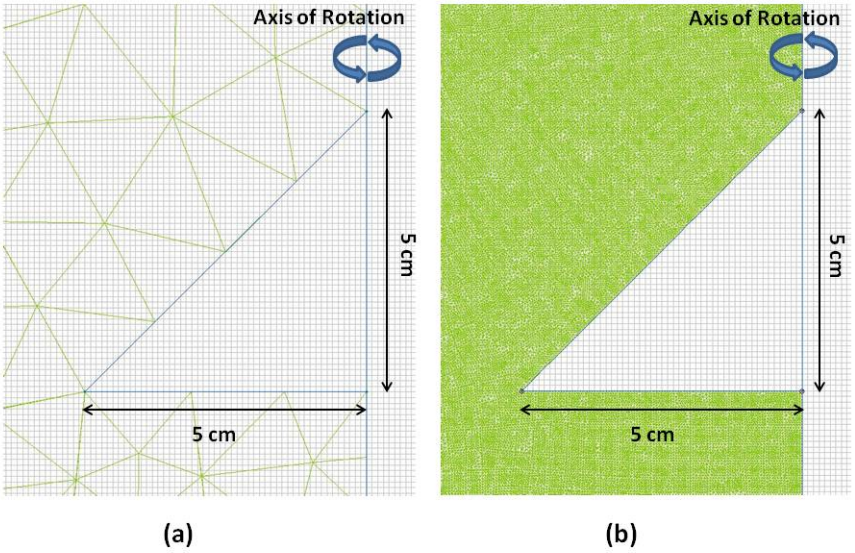

Figure 4.6: Analytical nodes on a cone-shaped electrode 5 cm in radius and 5 cm in height (a) Default mesh spacing, (b) Mesh spacing set at 0.5 mm.

Table 4.1: Simulation parameters and dimensions of the electrodes.

Simulation Parameters	
Geometry model	Axisymmetrical
Mesh spacing	0.5 mm
Nominal field strength	10 kV/m
Distance to ground	10 cm
Electrode Dimensions	
Height	5 cm
Radius / Base radius	5 cm

The graphic simulation results of the circular plate, cone, frustum of cone and hemispherical shaped electrodes are shown in Figure 4.9, 4.10, 4.11 and 4.12 respectively. All the electrodes are placed in the centre of the test rig and close to the ground plane.

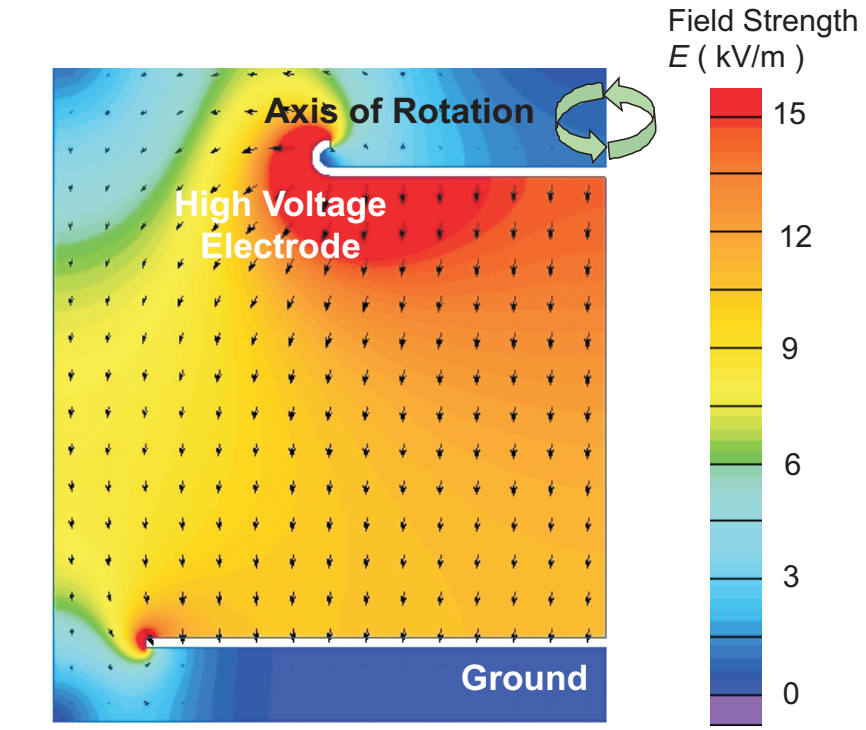

Figure 4.7: Simulation result of the test rig on its own.

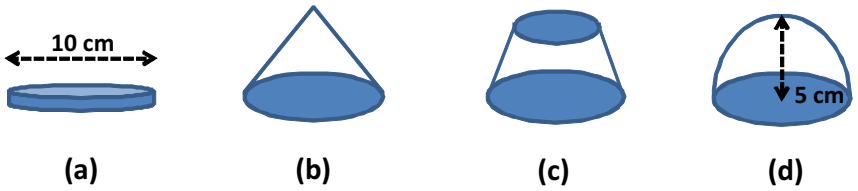

Figure 4.8: Shapes that have been investigated for the harvesting electrode: (a) Circular plate, (b) Cone, (c) Frustum of cone, (d) Hemisphere.

Charges are induced on the upward facing surface(s) of the electrode. The simulation results of all the electrodes that have been investigated are presented in Table 4.2. Visual comparison of these results is presented in Figure 4.13. The simulation results show that hemispherical shaped electrode has the biggest upward field facing surface area and induced the largest amount of charge.

Besides being able to induce the largest amount of charge among all the shapes that have been investigated, hemispherical electrode does not have any upward

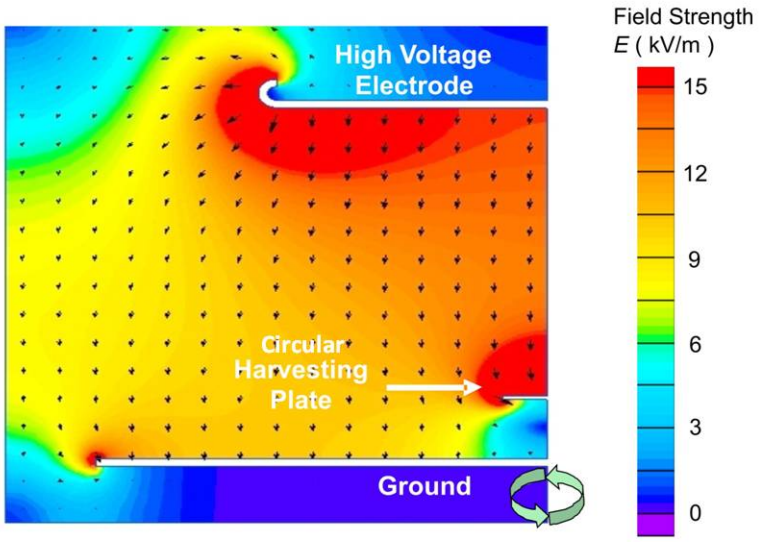

Figure 4.9: Simulation result of a circular plate shaped electrode inside the test rig.

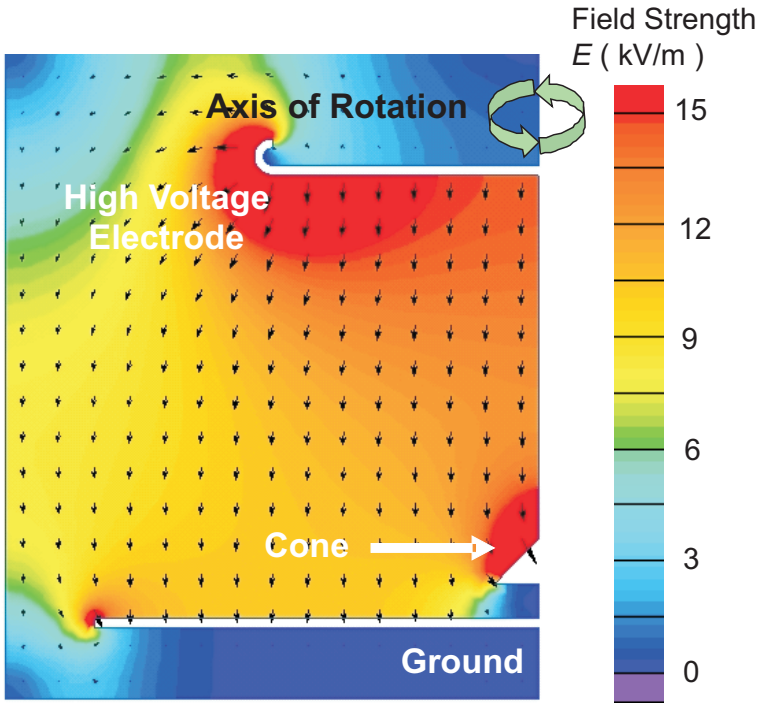

Figure 4.10: Simulation result of a cone shaped electrode inside the test rig.

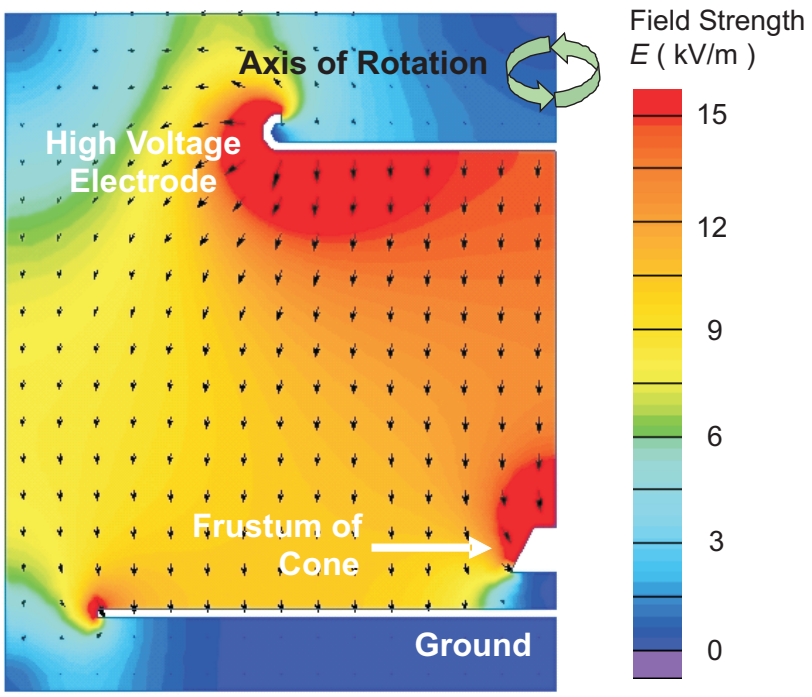

Figure 4.11: Simulation result of a frustum of cone shaped electrode inside the test rig (top plane radius = 2.5 cm, base plane radius = 5.0 cm).

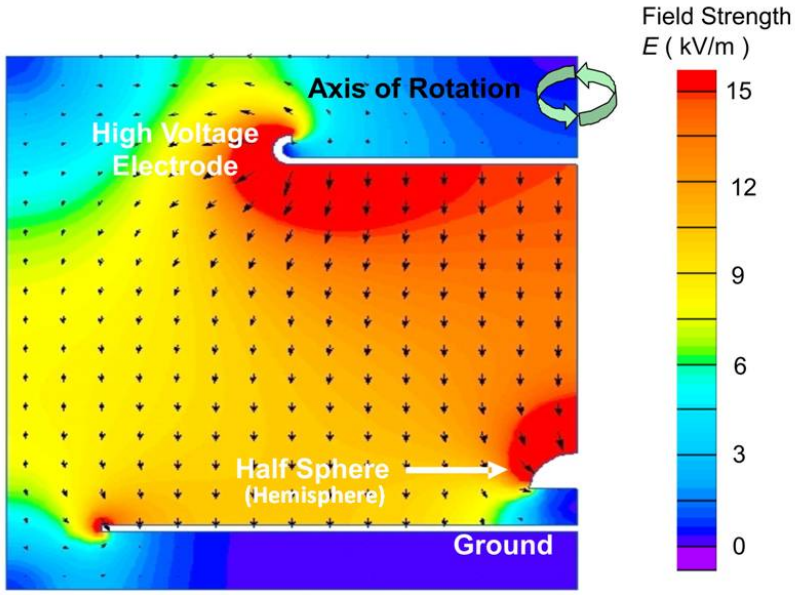

Figure 4.12: Simulation result of a hemispherical shaped electrode inside the test rig.

facing sharp edge. It reduces possibility of flash over or partial discharge from occurring when the harvesting device is deployed in substations. Hemisphere is considered to be the prefer shape for the harvesting electrode.

Table 4.2: Simulation results of all the electrodes that have been investigated.

Shape	Field strength above the electrode, kV/m	Upward facing area, cm^2	Induced charge on the field facing area, nC
Circular plate	21.512	94.248	2.911
Cone	46.316	111.070	2.492
Frustum of Cone	28.174	151.350	3.326
Hemisphere	36.386	157.080	3.549

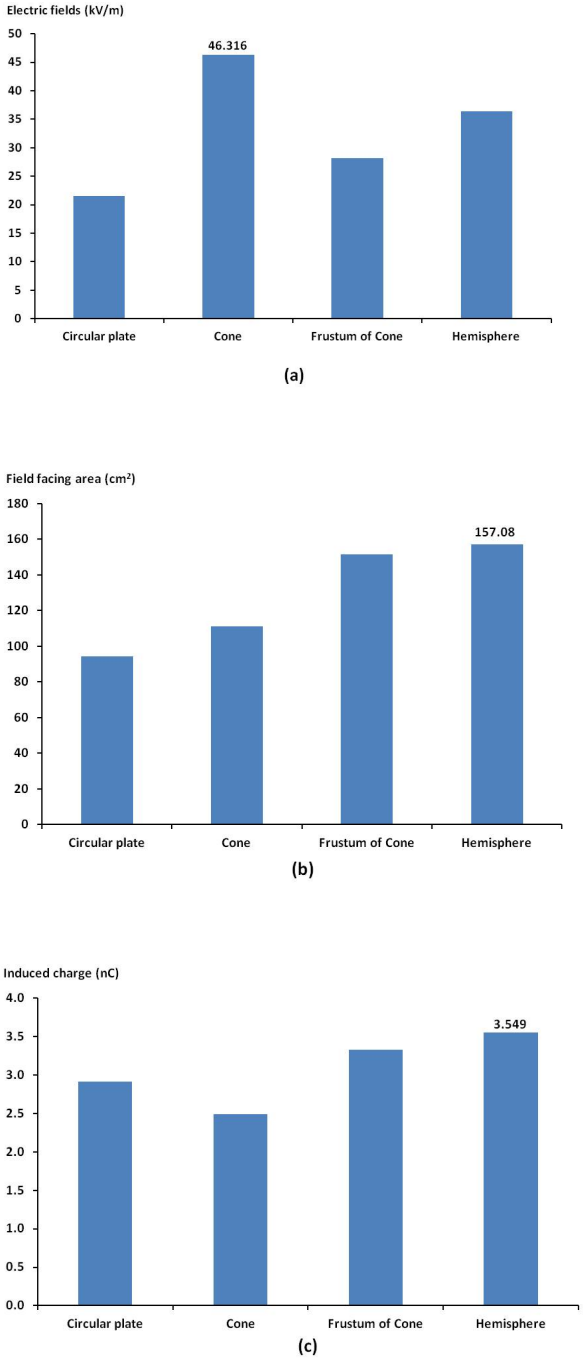

Figure 4.13: Comparison of the simulation results (a) Strength of the electric fields, (b) Upward field facing area, (c) Amount of charge induced on the field facing area.

4.3.4 Derivation of the induced charge formula for hemispherical electrode

Wireless sensors could be installed in different locations throughout a substation. Prospective harvesting devices are likely to 'follow the footstep' of the wireless sensors. It is beneficial to establish the relationship between the amount of charge induced on a hemispherical electrode and parameters that associate with the deployment of a harvesting device.

The amount of charge induced on a hemispherical electrode is influenced by the strength of the electric fields, the dimensions of the electrode and its distance to ground. The range and incremental step of these parameters are listed in Table 4.3. Figure 4.14 depicts a hemispherical electrode inside quasi-uniform electric fields.

The investigative work is conducted through simulation. The graphs presented in Figure 4.15 indicate that the amount of charge induced on a hemispherical electrode has a linear relationship with the strength of the electric fields. The linear nature of the relationship is not affected by the dimensions of the electrode nor its distance to ground.

The graphs shown in Figure 4.16 suggest that the amount of charge induced on a hemispherical electrode also has a linear relationship with its distance to the ground. The gradient depends on the dimensions of the electrode. The strength of the electric fields is kept at 10 kV/m during the investigation. This will be taken into consideration when the deriving the formula.

The graphs displayed in Figure 4.17 show the amount of charge induced on a hemispherical electrode is likely to have a second order polynomial relationship with its dimensions. The coefficients are heavily influenced by the distance

Table 4.3: Range and incremental step of the simulation parameters.

Parameters	**Symbol**	**Investigation range**	**Incremental step**
Electric fields, kV/m	E	0 – 20	1
Distance to ground, cm	d	1 – 10	1
Hemisphere radius, cm	r	0 – 10	1

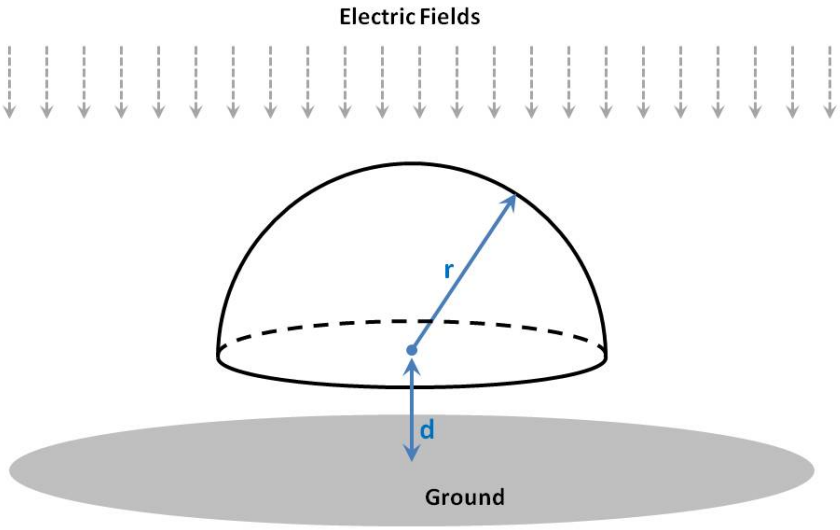

Figure 4.14: Hemispherical electrode inside electric fields.

between the electrode and ground.

The formula that derives the amount of charge induced on a hemispherical electrode is proposed as:

$$Q_i = (P_1 r^2 + P_2 r + P_3 + P_4 d) \times \frac{E}{10} \tag{4.2}$$

where

Q_i is the amount of induced charge, C

E is the strength of the electric fields, kVm^{-1}

r is the height and radius of the hemispherical electrode, cm

d is the distance between the electrode and ground, cm

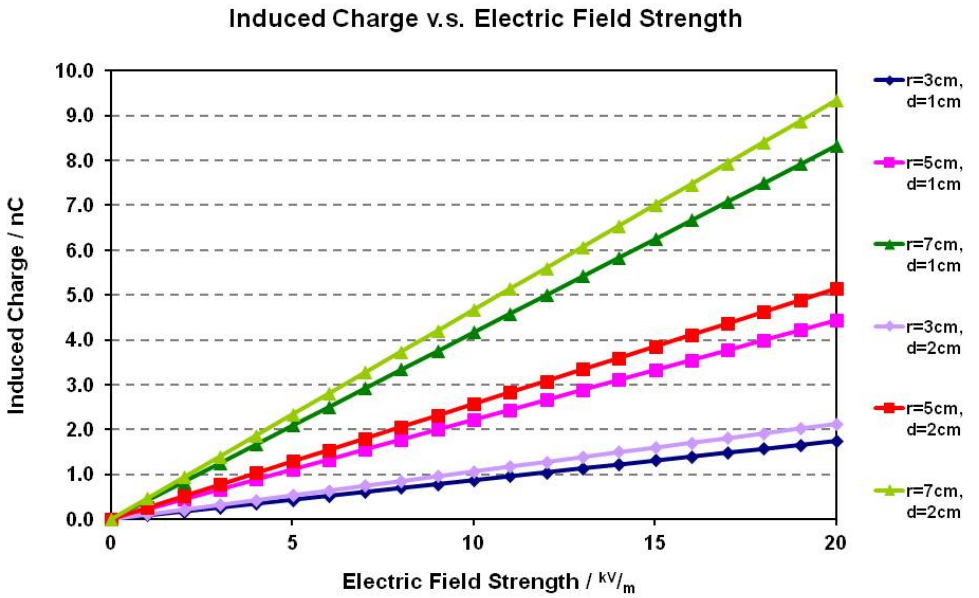

Figure 4.15: Amount of the induced charge against field strength.

Coefficients P_1, P_2, P_3 and P_4 are derived from simulation results, of which:

$$P_1 = 1 \times 10^{-12}d + 8 \times 10^{-11} \tag{4.3a}$$

$$P_2 = 1 \times 10^{-12}d^2 + 7 \times 10^{-11}d - 1 \times 10^{-11} \tag{4.3b}$$

$$P_3 = 2 \times 10^{-12}d - 1 \times 10^{-11} \tag{4.3c}$$

$$P_4 = 2 \times 10^{-12}r^2 + 5 \times 10^{-11}r + 3 \times 10^{-11} \tag{4.3d}$$

The formula that can be used to estimate the amount of charge induced on a hemispherical electrode is obtained by substituting the coefficients from (4.3) into (4.2):

$$Q_i = \frac{E}{10} \times [8 \times 10^{-11}r^2 + 3.2 \times 10^{-11}d + rd(3 \times 10^{-12}r + 1 \times 10^{-12}d + 1.2 \times 10^{-10}) - 1 \times 10^{-11}(r+1)] \tag{4.4}$$

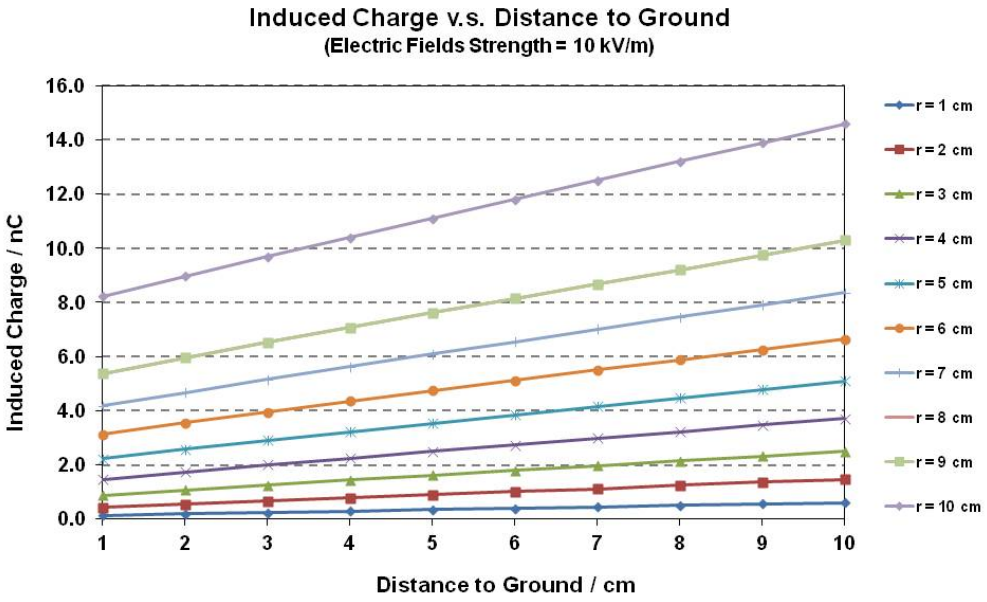

Figure 4.16: Amount of the induced charge against the electrode's distance to ground.

where

Q_i is the amount of induced charge, C

E is the strength of the electric fields, kVm^{-1}

r is the height and radius of the hemispherical electrode, cm

d is the distance between the electrode and ground, cm

The validity of (4.4) relies on the parameters keep staying within the range specified in Table 4.3.

Expanding the area for charge induction is undoubtedly beneficial from the energy harvesting point of view. This could be achieved by placing a conductor tube underneath the high voltage transmission lines [6]. Incorporating energy harvesting and wireless energy transfer could be a way forward [7]. However, there are still plenty of hurdles to overcome before these two technologies can be

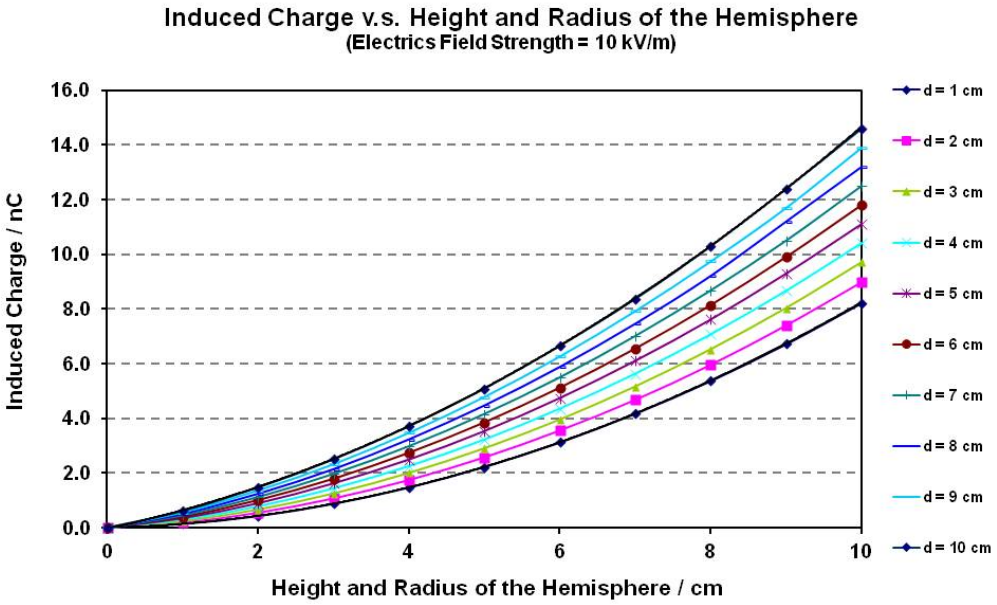

Figure 4.17: Amount of the induced charge against the dimensions of the electrode.

applied together. Keeping the harvesting device and the application load together reduces the transfer loss.

4.4 Summary

This chapter explained how charge is induced on an electrode when it is under the influence of electric fields. Electrodes of different shapes have been investigated: circular plate, cone, frustum of cone and hemisphere. Hemispherical electrode is found to be able to induce the largest amount of charge, which is approximately 7% more than the second most efficient shape – frustum of cone, if the radius and/or height of the electrodes are identical. In addition, a formula has been derived to estimate the amount of charge that can be induced on a hemispherical electrode. It was derived when the maximum radius of the electrode is 10 cm and the maximum distance between the electrode and the ground is also 10 cm. Nev-

ertheless, it could still predict the amount of charge induced on a hemispherical electrode with a high degree of accuracy when the parameters are outside these boundaries.

Inducing charge on the electrode is only the first step of the harvesting process. The induced charge needs to be transferred from the harvesting electrode to the energy storage. To achieve high efficiency, it is crucial to minimise the transfer loss. The following chapter will discuss how to efficiently transfer the induced charge from the harvesting electrode to the energy storage.

Bibliography

[1] H. Chisholm (editor). The Works of John Canton, *Encyclopædia Britannica (11th edition)*, Cambridge University Press, 1911.

[2] A. Pedersen, G. Crichton and I. McAllister. Partial Discharge Detection: Theoretical and Practical Aspects, *IEE Proc.-Sci. Meas. Technol.*, Vol. 142, No. 1, January 1995.

[3] A. Pedersen, G. Crichton and I. McAllister. The Functional Relation Between Partial Discharges and Induced Charge, *IEEE Transactions on Dielectrics and Electrical Insulation*, Vol. 2, No. 4, August 1995.

[4] J. Kraus and D. Fleisch. *Electromagnetics with Applications, 5th edition*, 1999, WCB/McGraw-Hill, ISBN 0-07-116429-4.

[5] E. Mazin, S. Dubitsky and V. Podnos. *Quickfield 6.3 Users' Guide*, Jan 2017, CreatSpace Independent Publishing Platform, ISBN-10 1542615690.

[6] S. Kang et al. Electric Field Energy Harvesting Under Actual Three-Phase 765 kV power transmission Lines for Wireless Sensor Node, *IET Electronics Letters*, Vol. 53, No. 16, pp. 1135 - 1136, August 2017.

[7] M. Hajikhani and F. Labeau. *Proc. IEEE International Conference on Communication Systems (ICCS)*, 6 pages, Shenzhen, China, December 2016.

Chapter 5

Charge transfer arrangements

5.1 Introduction

The previous chapter explained how charge is induced on a conductor that is under the influence of electric fields. Putting two conductors at different equipotential positions will produce a potential difference between them. These two conductors in effect form a capacitive component in the circuit. The impedance of a capacitive component is obtained from:

$$Z_c = \frac{1}{j\omega C} \tag{5.1}$$

where

Z_c is the impedance of a capacitive component, Ω
ω is the angular frequency where $\omega = 2\pi f$, rad/s
C is the object's capacitance, F

The impedance of a capacitive component, as shown in (5.1), is inversely proportional to the frequency of the electrical signal. Electricity grids all are operated at either 50 or 60 Hz. The impedance of a capacitive component would be in the region of a few hundred mega ohms if it is operated under mains frequency.

The loading effect, which is caused by the high output impedance, will prevent substantial proportion of the energy to be transferred from the energy source to the load. The most straight forward way to mitigate the loading effect is to

Table 5.1: Dimensions of an experimental harvesting device.

Radius of the hemispherical electrode	9 cm
The gap between the hemispherical electrode and the bottom plate	11 cm
Overall height of the device	20 cm

match the input impedance of the load with the output impedance of the source. However, the additional impedance that needs to be introduced will dominate the overall impedance of the load. The application component would only receive a small proportion of the energy delivered by the source. The amount of energy that can be delivered by the source is likely to be very modest in the first instance. Therefore, impedance matching is not suitable in this case.

The technical difficulty encountered in this study is similar to the challenge other researchers in the field of energy harvesting have been facing, where a relatively large voltage is generated across an energy source with very high impedance [1, 2]. The amount of charge that can be induced on an electrode is fixed. It would be highly beneficial to find an efficient way to transfer the induced charge from the source to the load without altering their impedance profiles.

An experimental harvesting device has been made for testing different charge transfer arrangements. It has a hemispherical-shaped top electrode. The dimensions of the experimental harvesting device are listed in Table 5.1. Figure 5.1 shows the experimental harvesting device sits in the centre of the test rig. The Quickfield simulation results presented in Table 5.2 show that 12.96 nC and 25.93 nC of charge are expected to be induced on the hemispherical electrode when the strength of the electric fields is 10 kV/m and 20 kV/m respectively. The performance of several charge transfer arrangements are presented in this chapter.

5.2 Linear conversion

The block diagram of the linear conversion arrangement is shown in Figure 5.2. The harvesting device is connected to a full wave bridge rectifier, which converts AC into DC. A capacitor stores the output of the bridge rectifier.

The relationship between the amount of charge stored on a capacitor, the

capacitance of the capacitor and the voltage across the capacitor is presented by (5.2). The amount of energy accumulated on a capacitor, as suggested by (5.3), is proportional to capacitance of the capacitor and the square of the voltage across

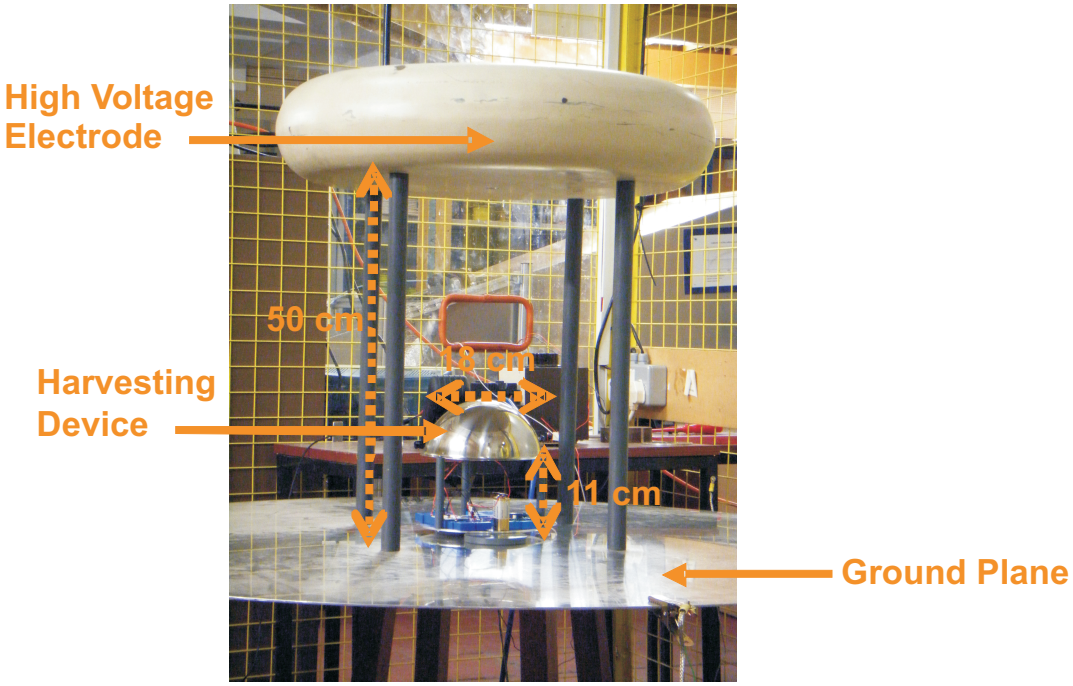

Figure 5.1: An experimental harvesting device sits in the centre of the test rig.

Table 5.2: Quickfield simulation results of the amount of charge induced on the experimental harvesting device.

Electric fields	Amount of charge induced on the hemispherical electrode
10 kV/m	12.96 nC
20 kV/m	25.93 nC

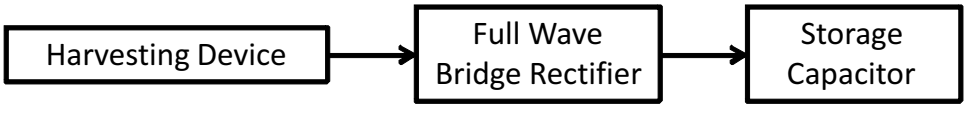

Figure 5.2: Constituent part of the harvesting device that adopts the linear conversion arrangement.

the capacitor. Increasing the voltage across the storage capacitor has a bigger impact on the amount of energy accumulated on the capacitor than rising the capacitance of the capacitor.

$$Q = CV \tag{5.2}$$

$$W = \frac{1}{2}QV = \frac{1}{2}CV^2 \tag{5.3}$$

where

Q is the amount of charge stored on the capacitor, C

C is the capacitance of the capacitor, F

V is the voltage across the capacitor, V

W is the amount of energy stored by the capacitor, J

The circuit shown in Figure 5.3 imitates a harvesting device that has adopted linear conversion sits in the centre of the test rig. The electric fields generated by the test rig are represented by V_1, which is a voltage source in Figure 5.3. The high voltage electrode of the test rig and the hemispherical upper electrode of the harvesting device are in effect formed a capacitive component. This component is represented by capacitor C_1. The harvesting device itself is represented by C_2. The storage capacitor of the harvesting device is represented by C_L.

The ideal storage capacitor, according to (5.3), should be large enough to storage most of the incoming charge while small enough to let the voltage across it to rise up accordingly. To search for a suitable C_L, capacitors ranging from 2.2 μF to 2200 μF have been installed into the harvesting device and experiments were conducted.

The high voltage electrode is energised to 10 kV. The strength of the electric fields in the centre of the test rig is 20 kV/m. The experimental results are shown in Table 5.3. The 2.2 μF capacitor can be charged up swiftly but it seems to reach saturation only after 2 minutes of operation. The voltage across the 2.2 μF capacitor is unable to rise up further even if test rig is continued to be energised. It is too small to store any more incoming charge. On the other end

of the spectrum, it is likely to take a very long time, i.e. more than an hour, to charge up a 2200 μF capacitor. Using either a 22 μF or 220 μF capacitor as the storage capacitor seems to be more sensible.

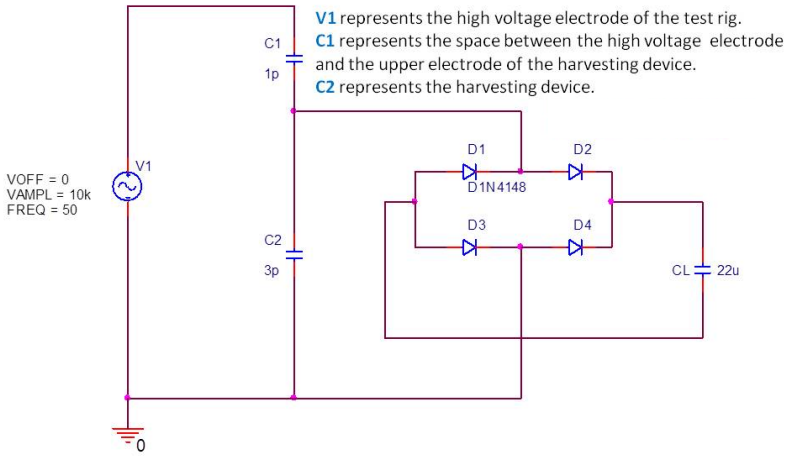

Figure 5.3: Representation of a harvesting device that has adopted linear conversion sits in the centre of the test rig.

Table 5.3: Voltage across different capacitors after the test rig has been energised.

Capacitor value, μF	DC voltage rating, V	Voltage across the capacitor after energisation, V					
		0.5 min	1 min	2 min	3 min	4 min	5 min
2.2	40	19.10	23.98	25.84	25.97	26.03	26.05
22	40	3.82	7.08	12.47	16.56	19.63	21.90
220	35	0.36	0.73	1.36	1.94	2.53	3.09
2200	35	0.26	0.39	0.57	0.69	0.78	0.86

Table 5.4: Energy accumulated on 22 μF and 220 μF capacitors.

Capacitor value, μF	Energy stored on the capacitor after energisation, mJ					
	0.5 min	1 min	2 min	3 min	4 min	5 min
22	0.16	0.55	1.71	3.02	4.24	5.28
220	0.014	0.059	0.20	0.41	0.70	1.05

The amount of energy accumulated on 22 μF and 220 μF capacitors are shown in Table 5.4. They are obtained by putting the respective results presented in Table 5.3 into (5.3). The amount of energy stored on a 22 μF capacitor is a few times of the energy stored on a 220 μF capacitor. The results show that the most suitable candidate for C_L is a 22 μF capacitor or any capacitor of similar value.

5.3 Synchronised switching

5.3.1 Introduction

The loading effect caused by the high output impedance of the capacitive energy source makes the linear conversion arrangement highly inefficient. Separating the source and the load has the potential to mitigate the loading effect and allow the maximum possible amount of charge to be induced.

The amount of charge that has been induced on the top electrode of a harvesting device depends on the phase position of the mains voltage waveform. Maximum amount of charge is induced at the peaks and troughes of the waveform. In theory, it is advantageous to connect the source and the load at these moments to transfer the induced charge out of the electrode.

The connection and disconnection of the source and the load involve switching. A device that harvests energy from the magnetic fields has been using switching to reduce the non-saturation time of the magnetised core that surrounds the high voltage transmission line [3]. The timing of the switching operations doesn't need to be very precise. However, the switching operations proposed in this study need to synchronise with the peaks and troughes of the mains voltage waveform. The occurrence of the switching operations is time-critical. The investigation will focus on whether synchronisd switching could mitigate the loading effect and improve the transfer efficiency.

5.3.2 Imitation of synchronised switching

The circuit that imitates synchronised switching is shown in Figure 5.4. The switch between the source and the load is represented by S_1. The operation of S_1 is controlled by setting the parameters of V_2.

The application load is represented by R_L. Commercially available wireless sensor platforms typically have an impedance profile in the region of a few tens of ohms when it is transmitting data [4]. Therefore, the value of R_L is set to 10 Ω.

A short burst of current will flow through R_L immediately after S_1 closes. This is illustrated in Figure 5.5. The current generated from the charge transfer only exists for a very short period of time, i.e. a few order of magnitude shorter than one second. The switch only needs to close briefly to facilitate the charge transfer.

Simulations were carried out in PSpice. Synchronised switching operation is visualised in Figure 5.6. The voltage across R_L is shown in Figure 5.6(a). These pulses contain the induced charge transferred from the source. They are the Induced Charge Pulses (ICPs). The dash and solid lines in Figure 5.6(b) represent the supply voltage to the HV electrode and the voltage across C_2 respectively. The occurrence of all of the ICPs coincides with either the peaks or the troughes of the supply voltage to the HV electrode.

In order to make the comparison, an example of non-fully synchronised switching operation is presented in Figure 5.7. The switch is operating at 200 Hz in this case. A proportion of the ICPs are not synchronised with the peaks nor the troughes of the supply voltage. The amplitudes of the ICPs and the voltage across C_2 are considerably lower than the corresponding parameters shown in Figure 5.6. The lower amplitudes indicate smaller amount of charge is transferred in each switching operation.

The simulation results suggest that synchronising the switching operations with the peaks and troughes of the supply voltage is more efficient in transferring the induced charge than the linear conversion arrangement. The electricity grid in the U.K. operates at a frequency of 50 Hz. Each cycle has a peak and a trough. Therefore, it is most advantageous to operate the switch 100 times per second with each switching operation synchronises with either the peak or the trough of the 50 Hz waveform.

Switching operation consumes energy. Low consumption would be a highly desirable characteristic for any switch. Advances in micro electro mechanical systems (MEMS) technology have reduced the energy consumption of a switch to about 10-100 nJ per operation [5, 6, 7]. The calculation presented in Table 5.5

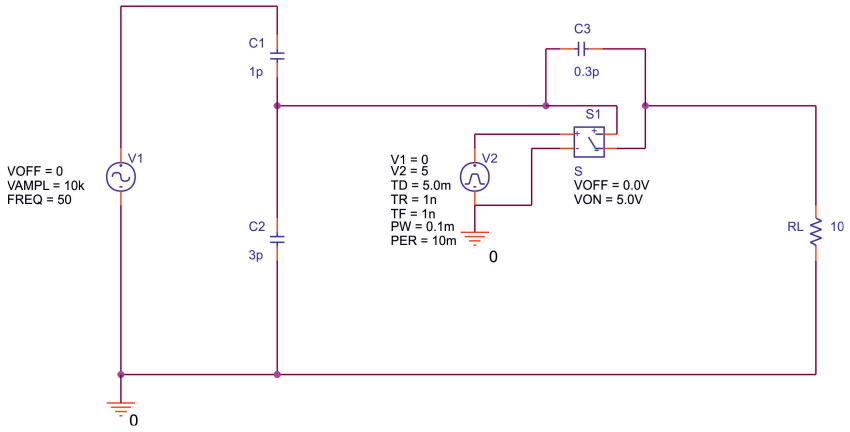

Figure 5.4: Simulation circuit that imitates synchronised switching.

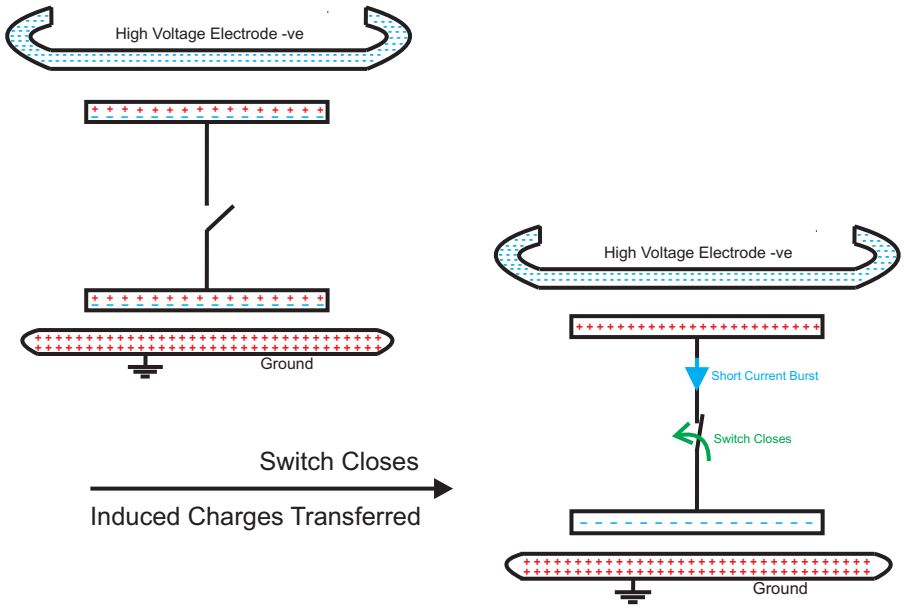

Figure 5.5: Illustration of charge induction and transfer during the negative half cycle.

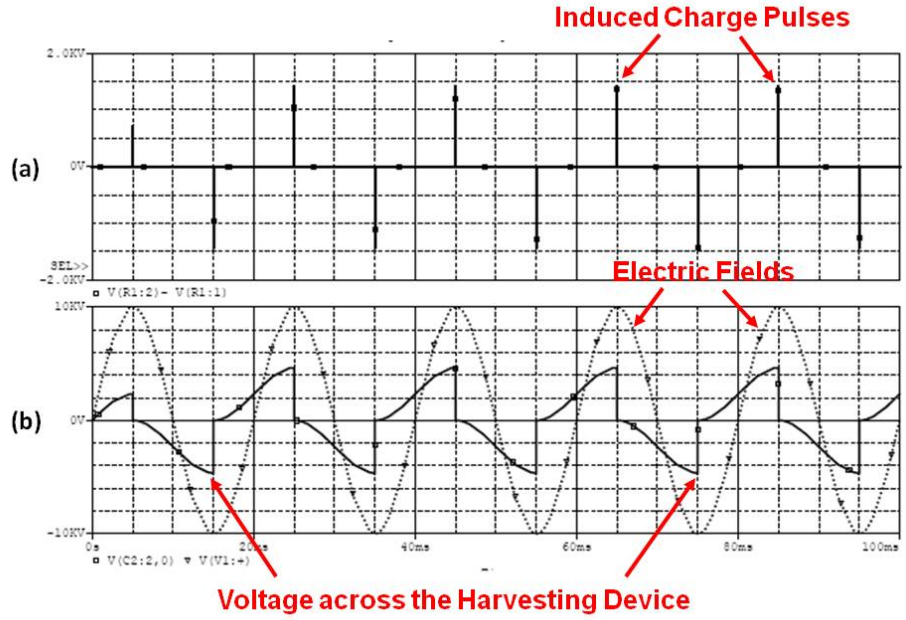

Figure 5.6: Voltages across (a) the resistive load, (b) the harvesting device when the switching operation is purposefully synchronised with the 50 Hz waveform.

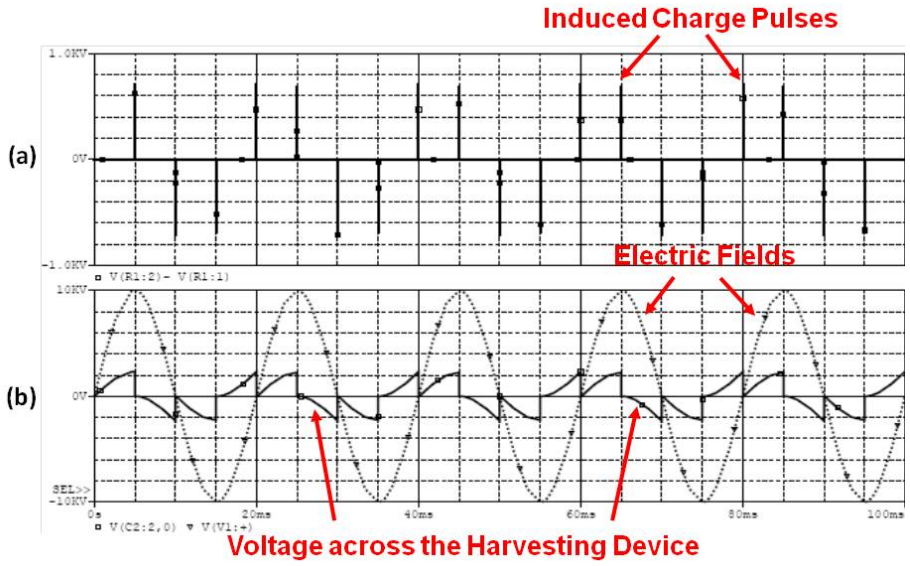

Figure 5.7: Voltages across (a) the resistive load, (b) the harvesting devices when the switch is operating at 200 Hz.

Table 5.5: Energy consumption of the synchronised switching arrangement.

Number of switching per second	100
Energy consumed by each switching operation	100 nJ
Energy consumed after 1 min of operation	0.6 mJ
Average power demand	10 μW

assumes the most unfavourable scenario. It shows that any harvesting device that intends to synchronise its switching operations to the peaks and troughes of the 50 Hz waveform has to be able to harness at least 0.6 mJ of energy per minute. Otherwise, it is not worth the effort.

5.3.3 Implementation of synchronised switching for experimental purpose

The simulation results presented in Section 5.3.2 suggest that synchronised switching could be more efficient than linear conversion arrangement. It is worthwhile to examine simulation outcome by experiment. A circuit needs to be built to facilitate the investigation on synchronised switching. The pulses it generates should appear in sync with the peaks and troughes of the mains voltage waveform. Since these pulses control the operation of the switch, they are named Switching Control Pulses (SCPs).

The block diagram of the proposed SCPs generation circuit is shown in Figure 5.9. It serves not only as the circuit design blueprint but also demonstrates the process of generating SCPs. The circuit design is presented in Figure 5.9.

Operational amplifier U_1 shifts the waveform of the mains voltage forward by 90^o. The peaks and troughes of the original waveform would correspond to the zero crossing points of the updated waveform. The main function of operational amplifier U_2 is to detect the zero crossing points on the updated waveform. The output of U_2 rises from 0 V to V_{cc} when the input signal passes 0 V with a positive gradient. The output of U_2 would remain at V_{cc} until the input signal passes 0 V with a negative gradient. The output of U_2 drops from V_{cc} to 0 V as soon as the input signal passes 0 V with a negative gradient. The output of U_2 would then remain at 0 V until the input signal passes 0 V with a positive gradient again.

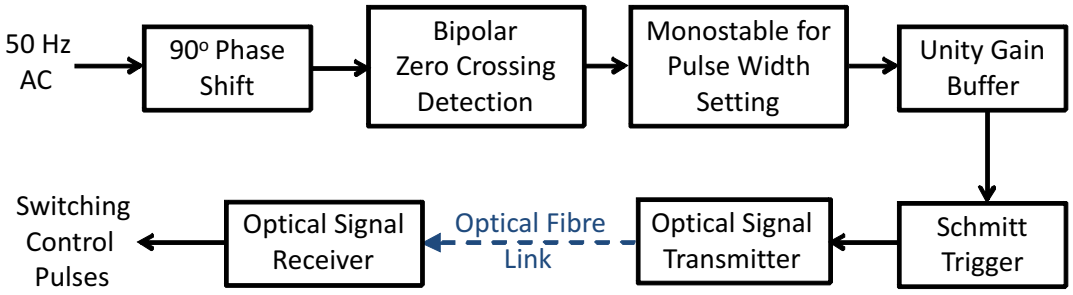

Figure 5.8: Constituent parts of the SCP generation circuit.

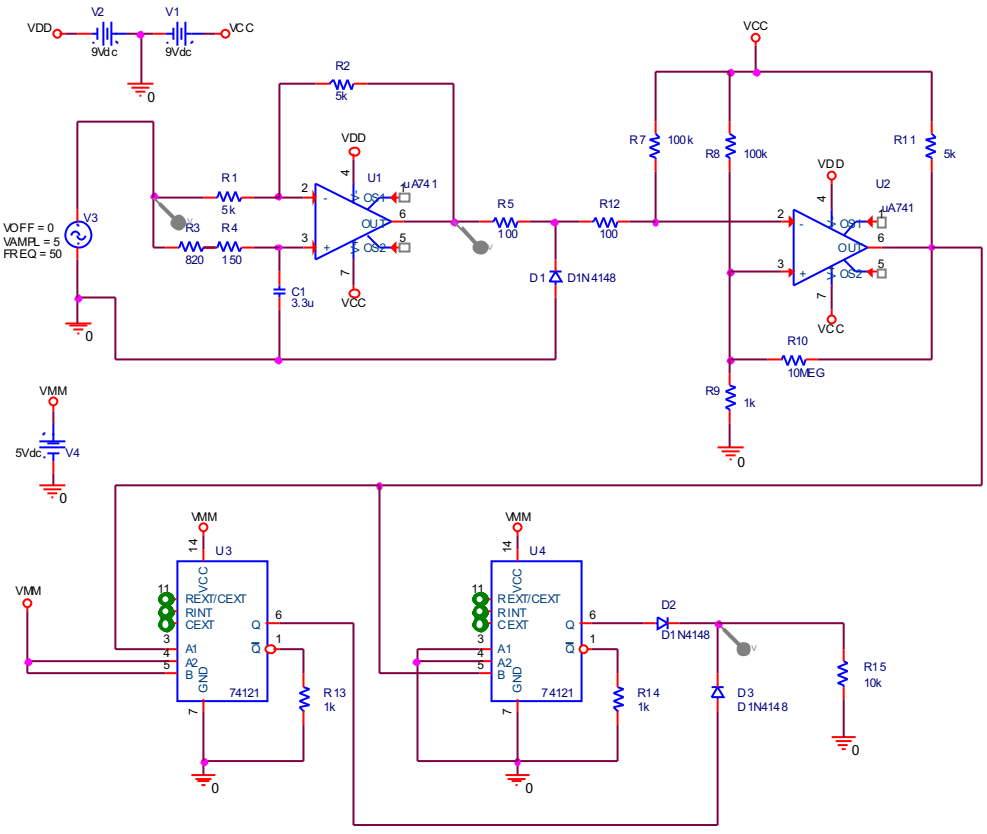

Figure 5.9: Diagram of the SCP generation circuit.

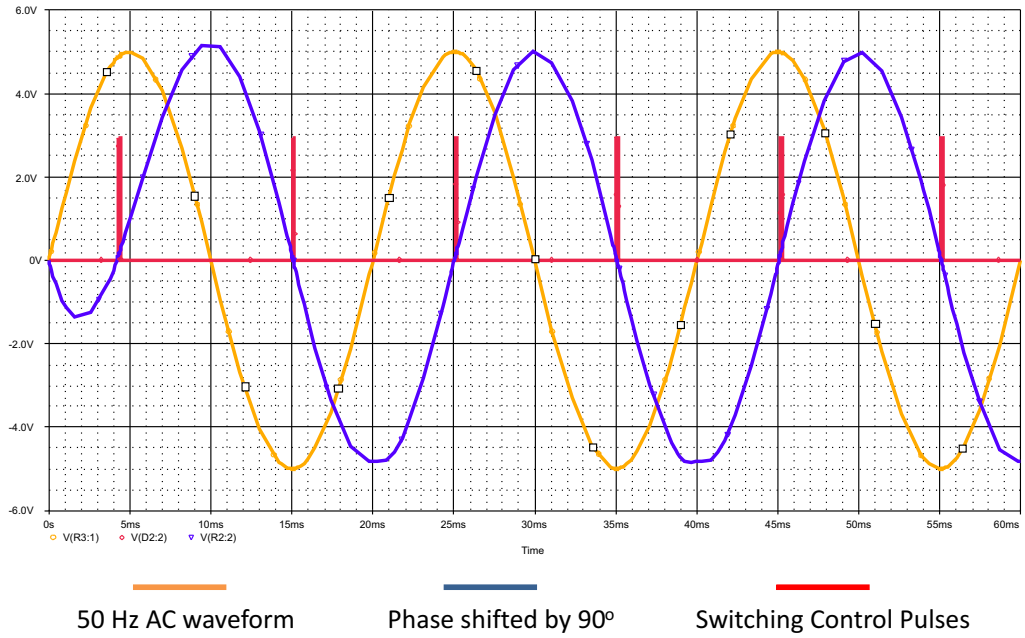

Figure 5.10: Simulation result of the SCP generation circuit.

The resultant output of U_2 is effectively a square wave.

The output of U_2 is fed into two separate monostable vibrators. Monostable vibrator U_3 generates a pulse-shaped output every time it encounters a fast falling transition ($V_{cc} \rightarrow 0$ V) from the input. Monostable vibrator U_4 generates a pulse-shaped output every time it encounters a rapid rising transition (0 V $\rightarrow V_{cc}$) from the input. The width of the pulses is determined by the external resistors that connects to the monostable vibrators, which are R_{13} and R_{14} respectively. The width of the pulses is set to 0.1 ms in this study. The outputs of U_3 and U_4 are combined together before being transmitted to the switch.

The simulation result of the SCP generation circuit is presented in Figure 5.10. The occurrence of all the SCPs are coincided with either the peaks or the troughes of the mains voltage waveform.

The circuit that has been built for generating SCP is shown in Figure 5.11. To avoid the signal being distorted by other components in the circuit, the combined output of the monostable vibrators passes through a unity gain buffer. The output of the unit gain buffer is fed into a Schmitt trigger to reduce the noise level of the signal. The output of the Schmitt trigger is transmitted via an optical fibre link (Broadcom HFBR-2528Z) to the switch of the harvesting device. The

experimental setup for generating synchronised SCP is shown in Figure 5.12.

The harvesting device shown in Figure 5.1 is surrounded by quasi-uniform electric fields when the test rig is energised. Having a piece of copper wire cut across the centre of the test rig is more than likely to distort the electric fields. Optical fibre does not contain any metal. It is unlikely to have any substantial impact on the electric fields. Therefore, an optical fibre link is used to transmit the SCPs to the switch.

An oscilloscope is used to capture the output of the SCP generation circuit, which is shown in Figure 5.13. The waveforms presented in Figure 5.13 match with the corresponding waveforms shown in Figure 5.10. The circuit presented in Figure 5.11 is able to generate the required output. The design objective has been met.

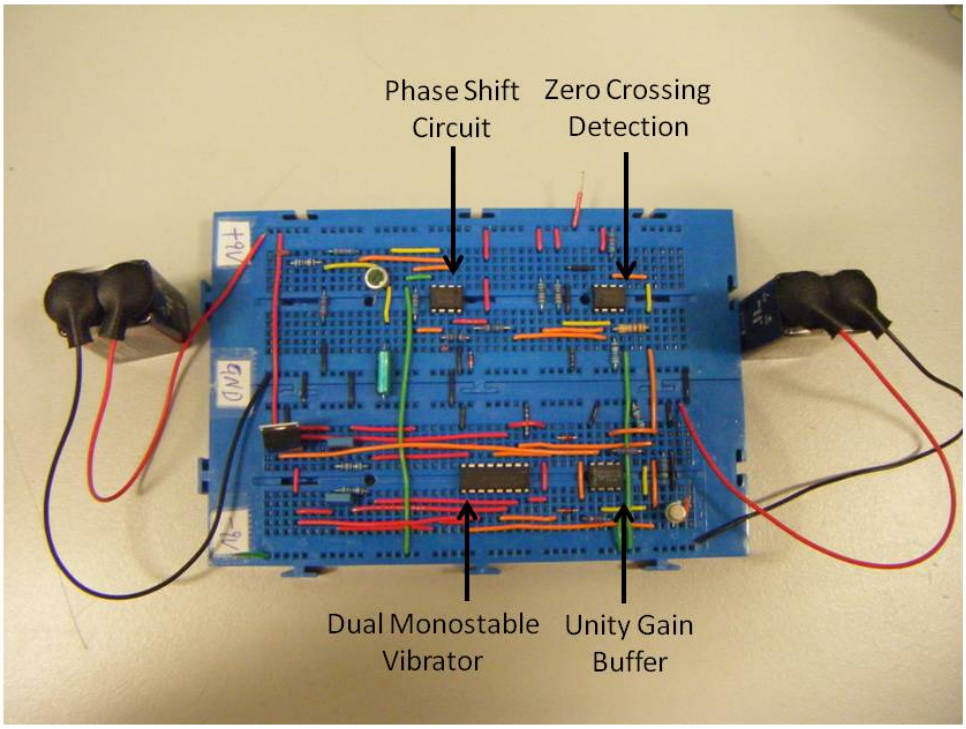

Figure 5.11: SCP generation circuit on breadboards.

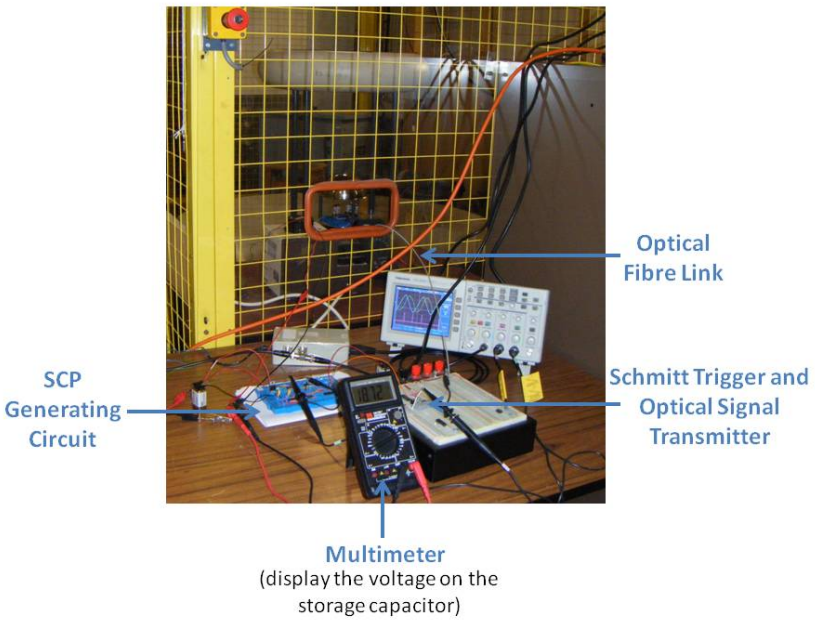

Figure 5.12: Experimental setup of the SCP generation and transmission.

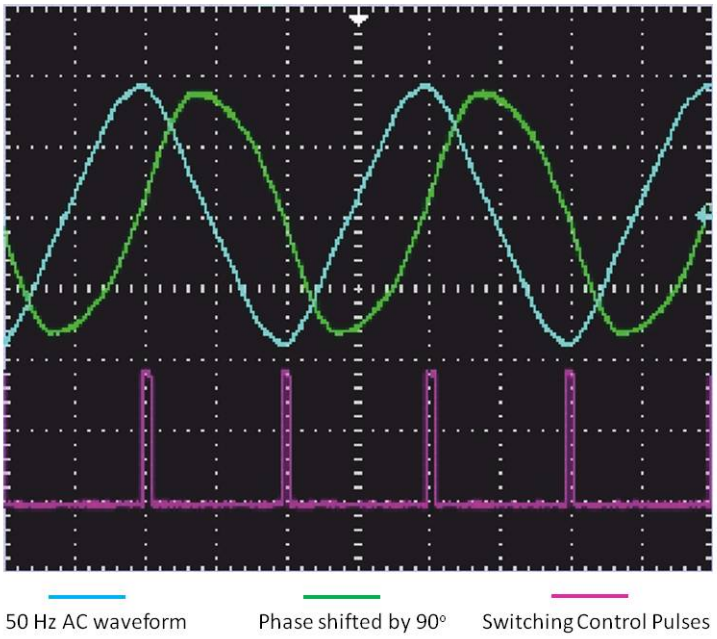

Figure 5.13: Original and phase shifted 50 Hz signals (top), switching control pulses (bottom).

5.3.4 Further optimisation of synchronised switching

Application loads, such as wireless sensors, require the DC power input to be stable. Most of the harvesting devices will produce output continuously as long as energy is available in the ambient environment. Wireless sensors typically consume most of their overall energy demand only when they are fully active, albeit in a short period of time. It is apparent that a fast reacting energy storage component, such as a capacitor, is needed to store the output energy from the harvesting device temporarily. However, it is not a good practice to charge up a capacitor through short pulses.

The most straight forward way to lengthen the pulse width is to put a large resistor next to the monostable vibrator. But it will shorten the duration for charge induction to take place and reduce the amplitude of the ICP. The voltage on the storage capacitor is unlikely to get as high as it could be.

Another approach to mitigate the disadvantage of short pulses is to smooth out the rapid transition edges. This could be achieved by placing an inductor between the switch and the rectification circuit. The voltage across the inductor will rise up to resist any further increase of the voltage itself when the inductor encounters the rising edge of a pulse. Equally, the voltage across the inductor will reverse its polarity to resist any further decrease of the voltage when the inductor encounters the falling edge of a pulse. The rate of change of the current flow is decreased. The current that charges up the storage capacitor is flowing in a more gradual manner.

A study called this method Synchronised Switching Harvesting on Inductor (SSHI) [8]. Considerable improvement in efficiency has been reported when SSHI was adopted by a vibration harvesting device based on piezoelectric materials [9]. It is worthwhile to investigate whether SSHI is able to further improve the harvesting device.

The block diagram of a harvesting device that has adopted SSHI as the charge transfer arrangement is shown in Figure 5.14. Circuit diagrams that represent the experimental setups of synchronised switching and SSHI are shown in Figure 5.15 and Figure 5.16 respectively. Inductors ranging from 10 μH to 100 mH have been tested. The simulation results suggest that putting a 22 mH inductor between the switch and the rectification circuit is most beneficial. The voltage on the storage

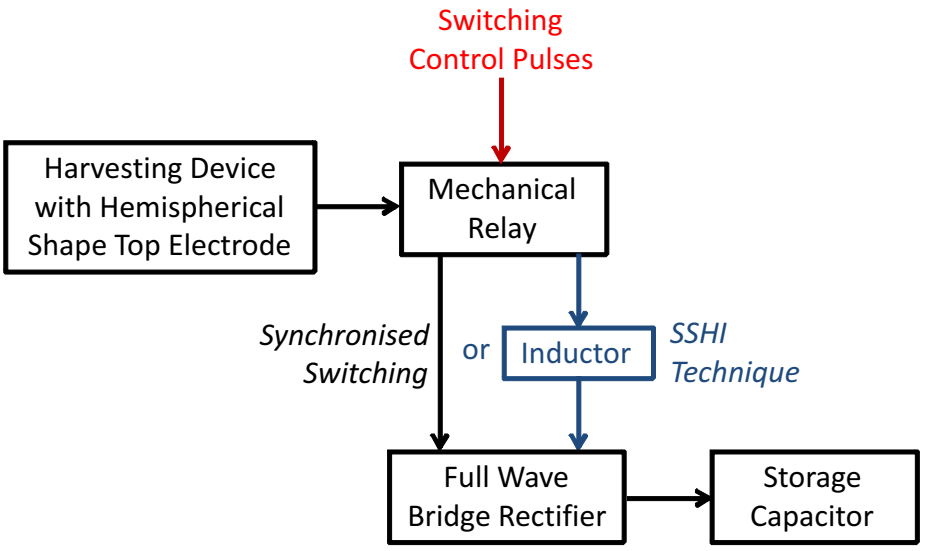

Figure 5.14: Constituent parts of the harvesting device that adopts synchronised switching and SSHI.

Table 5.6: Major components used in the experimental harvesting device.

Component	Manufacturer, Part Number and Important Parameter(s)
Mechanical Relay	Meder CRF05-1A, f_{max}= 5 kHz (operating time 0.1 ms)
Inductor	Coilcraft PCH-27-226, 22 mH
Storage Capacitor	Vishay CTS13226X9040C2P, Tantalum 22 μF, DC rating 40 V

capacitor rises up faster and get to a higher level.

Some of the components used in the experimental harvesting device are shown in Table 5.6. Different charge transfer arrangements have been examined. Table 5.7 shows how the storage capacitor is faring under 10 kV/m electric fields. Harvesting device that has adopted the SSHI arrangement is able to charge the capacitor up higher and faster than devices that have adopted other arrangements.

The net amount of energy harvested, of which the energy consumed by the switching operations has been taken into account, are presented in Table 5.8. Simulation estimates are derived based on the results presented in Table 5.2. This set of results acts as the benchmark measure. The harvesting device that has adopted synchronised switching consumes more energy than it is able to harness. It reinforces the argument that it is not a good practice to charge up a

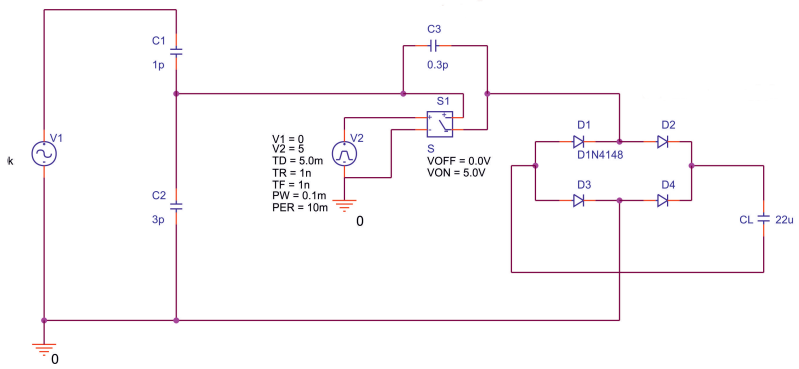

Figure 5.15: Representation of a harvesting device that has adopted synchronised switching sits in the centre of the test rig.

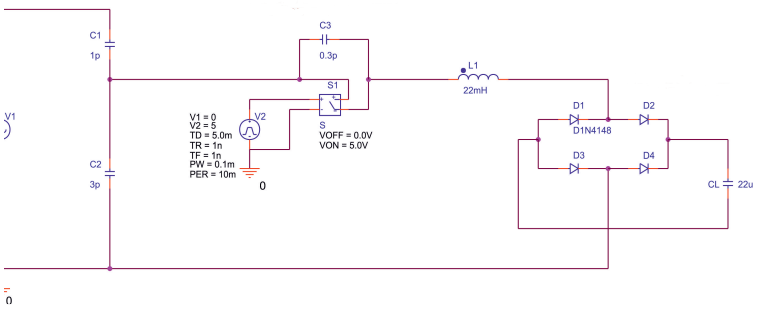

Figure 5.16: Representation of a harvesting device that has adopted SSHI sits in the centre of the test rig.

capacitor through short pulses.

The same experiments were repeated when the strength of the electric fields was increased to 20 kV/m. The results presented in Tables 5.9 and 5.10 show similar trends. The device that has adopted the SSHI arrangement is able to charge the storage capacitor up to its maximum rating after only 3 minutes of operation.

The experimental results presented in Tables 5.8 and 5.10 have been plotted in Figures 5.17 and 5.18 respectively. They confirm that SSHI is more efficient than other arrangements for transferring the induced charge from the harvesting electrode to the storage capacitor.

Table 5.7: Voltage on the 22 μF storage capacitor when the harvesting device is under 10 kV/m electric fields.

Charge Transfer Arrangement	Voltage across the 22 μF capacitor after charging begins, V					
	0.5 min	1 min	2 min	3 min	4 min	5 min
Linear Conversion	1.89	3.53	6.21	8.26	9.81	11.01
Synchronised Switching	2.85	4.86	7.83	9.91	11.41	12.53
SSHI with L=22mH	5.40	9.27	15.66	20.36	23.90	26.56

Table 5.8: Net amount of energy harvested under 10 kV/m electric fields.

Charge Transfer Arrangement	Net amount of energy harvested, mJ					
	0.5 min	1 min	2 min	3 min	4 min	5 min
Linear Conversion	0.04	0.14	0.42	0.75	1.06	1.33
Simulation Estimate	0.03	0.13	0.55	1.25	2.21	3.46
Synchronised Switching	-0.21	-0.34	-0.53	-0.72	-0.97	-1.27
SSHI with L=22mH	0.02	0.35	1.50	2.76	3.88	4.76

Table 5.9: Voltage on the 22 μF storage capacitor when the harvesting device is under 20 kV/m electric fields.

Charge Transfer Arrangement	Voltage on the 22 μF capacitor after charging begins, V					
	0.5 min	1 min	2 min	3 min	4 min	5 min
Linear Conversion	3.82	7.08	12.47	16.56	19.63	21.90
Synchronised Switching	4.74	8.15	13.49	17.43	20.30	22.40
SSHI with L=22mH	9.75	17.60	30.24	39.50	exceeds DC rating	

Table 5.10: Net amount of energy harvested under 20 kV/m electric fields.

Charge Transfer Arrangement	Energy stored on the 22 μF capacitor, mJ					
	0.5 min	1 min	2 min	3 min	4 min	5 min
Linear Conversion	0.16	0.55	1.71	3.02	4.24	5.28
Simulation Estimate	0.13	0.55	2.21	4.98	8.85	13.82
Synchronised Switching	-0.05	0.13	0.80	1.54	2.13	2.52
SSHI with L=22mH	0.75	2.81	8.86	15.36	Not Applicable	

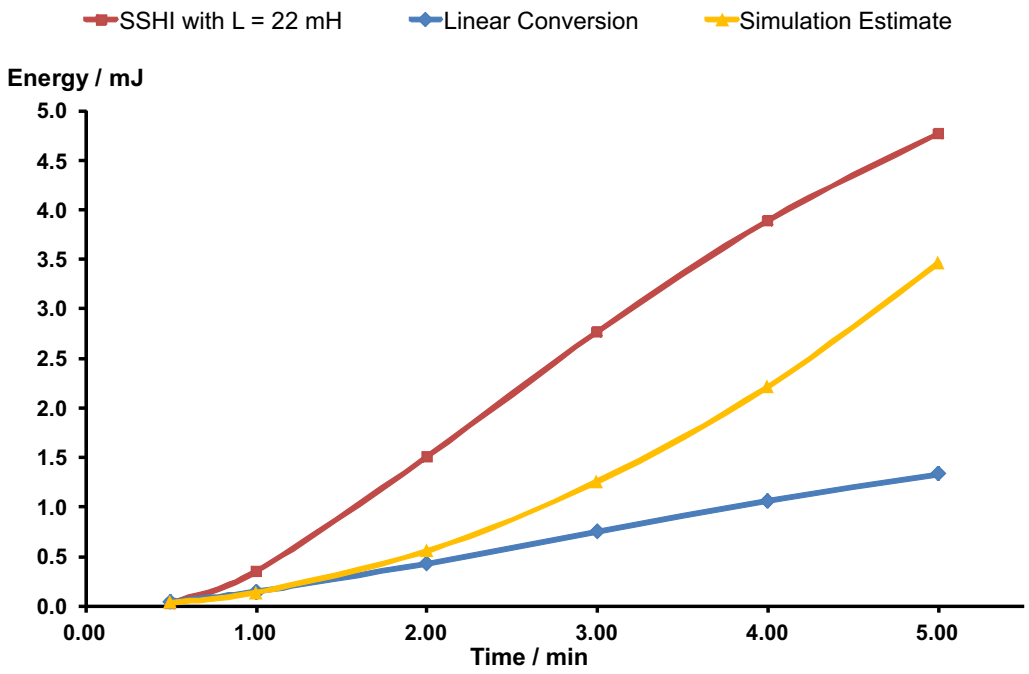

Figure 5.17: Net amount of energy harvested under 10 kV/m electric fields.

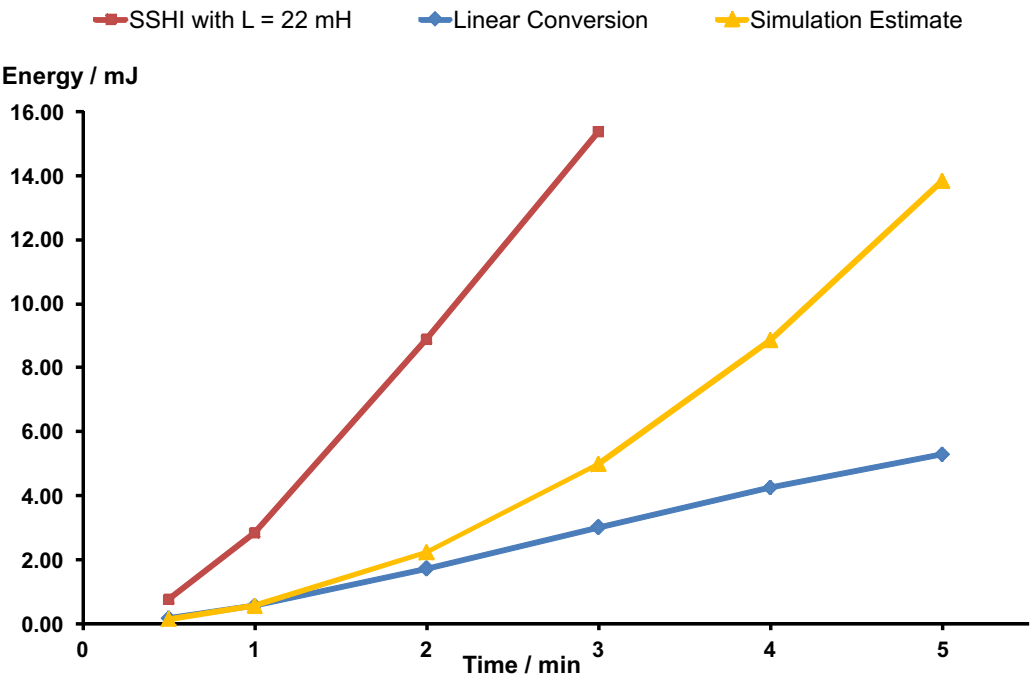

Figure 5.18: Net amount of energy harvested under 20 kV/m electric fields.

5.4 Summary

The most efficient charge transfer arrangement is found to be the Synchronised Harvesting Switching on Inductor (SSHI) technique. Investigation shows that 22 mH is the optimal value for the inductor. Each switching operation is synchronised with either the peaks or the troughs of the mains frequency. Assuming the average power consumption of the synchronised switching operation is 10 μW, the amount of energy transferred by the SSHI technique is approximately 3.6 times the amount transferred by linear conversion after 3 minutes of operation when the field strength is 10 kV/m. The efficiency of the SSHI technique increases further when the field strength is higher.

Although the most efficient charge transfer arrangement has been discovered, the average output power of the harvesting device is still too low to meet the demand of power hungry activities conducted by the sensor. In order to bridge this gap, the charging and discharging of the storage capacitor have to be managed. The next chapter is going to present the effort that has been made to design an energy buffer.

Bibliography

[1] N. Shenck and J. Paradiso. Energy Scavenging with Shoe-Mounted Piezoelectrics, *IEEE Mirco*, pp. 30-42, May-June 2001, IEEE.

[2] G. Szarka, B. Stark, and S. Burrow. Review of power conditioning for kinetic energy harvesting systems, *IEEE Transactions on Power Electronics*, pp. 803-815, Vol. 27, Issue 2, February 2012, IEEE.

[3] Y. Zhuang et al. An improved energy harvesting system on power transmission lines, *Proc. of Wireless Power Trasnfer Conference (WPTC)*, May 2017, Taiwan, IEEE.

[4] MICAz datasheet, Wireless Sensor Network, ACEINNA Inc, Massachusetts, USA.

[5] G. Rebeiz and J. Muldavin. RF MEMS switches and switch circuits, *IEEE Microwave Magazine*, pp. 59-71, December 2001, IEEE.

[6] E. Thielicke and E. Obermeier. A fast switching surface micromachined electrostatic relay, *Proc. of the 12th Internatioanl Conference on Solid State Sensors, Actuators and Microsystems*, pp. 899-902, June 2003.

[7] S. Jeong, D. Lee and W. Wang. Mathematical analysis and test of an electrostatically actuated micro-power replay, *Journal of Microsystems Technology*, pp. 635-645, Vol. 13, December 2006, Springer

[8] M. Lallart and D. Guyomar. Synchronized switch harvesting applied to self-powered smart systems: Piezoactive mircogenerators for autonomous wireless receivers, *Sensor and Actuators A*, pp. 263-272, Vol. 147, April 2008, Elsevier.

[9] M. Lallart and D. Guyomar. An optimized self-powered switching circuit for non-linear energy harvesting with low voltage output, *Smart Materials and Structures*, pp. 1-8, Vol. 17, May 2008, Institute of Physics (UK).

Chapter 6

The energy buffer

6.1 The function of energy buffer

The previous chapter explored how to transfer the induced charge onto the storage capacitor efficiently. It also touched on the challenge that the continuous power output of a harvesting device, which is represented by the dashed line in Figure 6.1, is usually too low to be of any practical use. The power consumption profile of an energy optimised wireless sensor is also shown in Figure 6.1. Modern wireless sensors consume as little as a few micro-ampere when they are in sleep mode. Power hungry activities, such as data acquisition and transmission, only last a short period if the amount of data needs to be handled is small. The highest consumption is a few tens of milliampere [1].

In order to bridge the gap, the storage capacitor should be allowed to accumulate sufficient amount of energy before the energy is discharged. In other words,

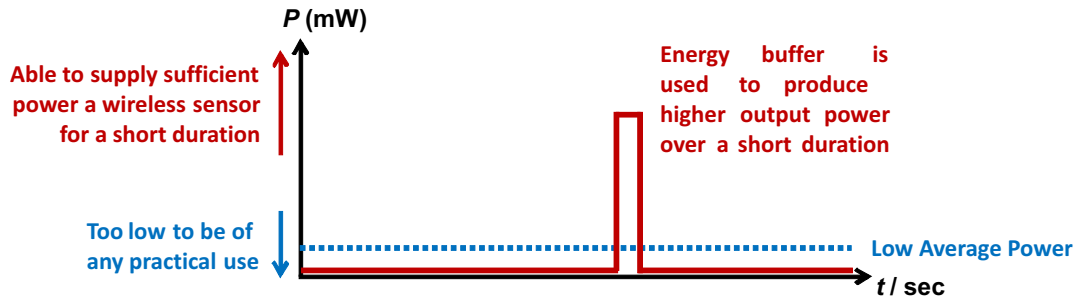

Figure 6.1: Power consumption profile of an energy optimised wireless sensor.

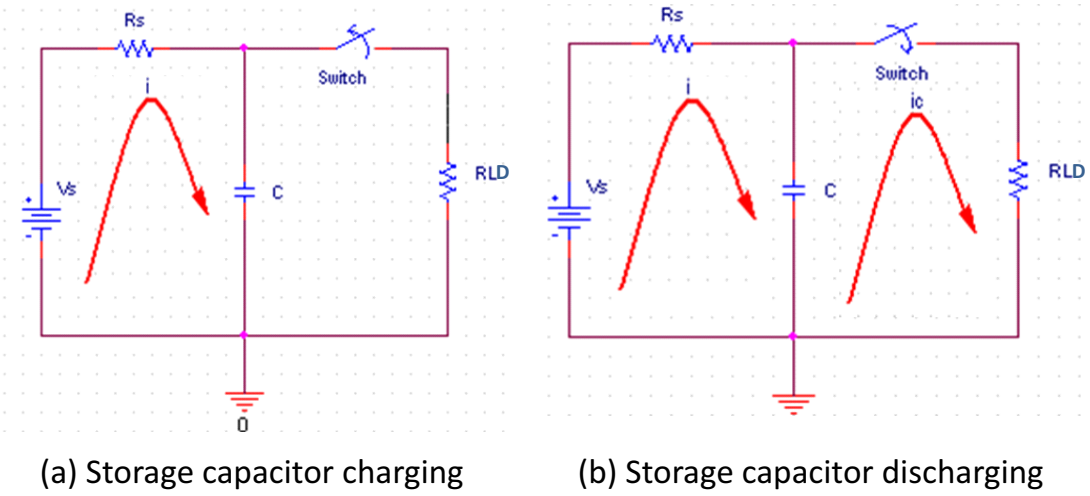

(a) Storage capacitor charging (b) Storage capacitor discharging

Figure 6.2: Interaction between the energy source (V_S, R_S), the storage capacitor (C) and the resistive application load (R_{LD}).

the charging and discharging of the storage capacitor need to be controlled.

The interactions between the energy source, the storage capacitor and the application load are illustrated in Figure 6.2. The most obvious parameter that can be used to control the operation of the switch is the voltage on the storage capacitor. The switch remains open when the storage capacitor is being charged up. It allows more energy to be accumulated onto the storage capacitor. The switch will close to release the stored energy when the voltage on the storage capacitor has risen up to a certain level. This would be the discharging trigger limit. The voltage on the storage capacitor will start to decrease once the stored energy is being released. The switch can be configured to open again when the voltage on the storage capacitor drops down to a particular level. This is likely to be the discharging completion limit. For the operation to be feasible, the discharging trigger voltage has to be higher than the discharging completion voltage.

The sole function of the proposed circuit is to control the accumulation and discharge of energy. It is appropriate to consider it as an energy buffer. This chapter is going to discuss the design and operation of the energy buffer.

6.2 Commercially available products

Energy buffers, also known as energy harvesting modules, are readily available on the market [2]. The operational characteristics of these products are presented in Table 6.1 and Figure 6.3.

The storage capacitor on these buffers can be charged up by either continuous or intermittent current. The voltage on the storage capacitor keeps increasing when more energy is being accumulated onto it. A proportion of the stored energy is released once the voltage on the storage capacitor rises up to the discharging trigger limit (V_H). Voltage on the storage capacitor will continue to decrease until it drops down to the discharging completion/termination limit (V_L). The voltage on the storage capacitor will stay at V_L, in other words the discharging stops, even if input power disappears.

Table 6.1: Operation cycle of the EH 300/301 units.

Voltage on the storage capacitor (V_{cap})	Time segment of the operation cycle
$0 \rightarrow V_H$	t_1
$V_H \rightarrow V_L$	t_2
remains at V_L	t_3
$V_L \rightarrow V_H$	t_4

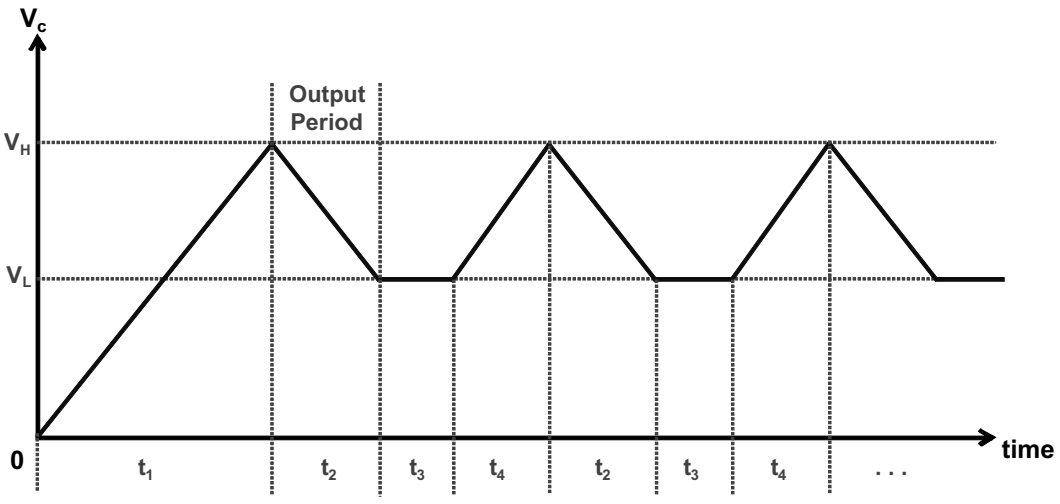

Figure 6.3: Illustration of the operation cycle of the EH 300/301 units.

Table 6.2: Technical parameters of the EH 300/301 units [2].

Harvesting Module	Capacitor (mF)	V_L (V)	V_H (V)	Output Energy (mJ)
EH 300	1.0	1.8	3.6	4.6
EH 301	1.0	3.1	5.2	8.3
EH 300A	6.6	1.8	3.6	30.0
EH 301A	6.6	3.1	5.2	55.0

The amount of energy released by each discharging equals to:

$$E = \frac{1}{2}C(V_H^2 - V_L^2) \tag{6.1}$$

The operation of the energy buffer depends solely on the voltage on the storage capacitor. The passive nature of the control mechanism helps to minimise the energy consumption.

The technical parameters are shown in Table 6.2. The discharging trigger limit and the discharging completion limit are set by the manufacturer. They cannot be changed. A generic energy buffer that would allow the voltage limits to be set according to individual application is highly desirable.

6.3 A generic energy buffer circuit

6.3.1 The proposed design

A generic energy buffer is envisaged to have the freedom to set its own voltage limits. The operational characteristics are similar to the commercially available products. The proposed design is explained in three stages.

The circuit diagram of the first stage is shown in Figure 6.4. The energy source and its output impedance are represented by V_S and R_S respectively. Resistors R_1, R_2 and R_3 are connected in series. The overall resistance of the resistors chain needs to be a few orders of magnitude larger than the application load in order to minimise the amount of current to be drained from the storage capacitor. The voltage at point A is intrinsically higher than the voltage at point B ($V_A > V_B$).

The circuit diagram of the second stage is shown in Figure 6.5. T_1 is a n-type transistor while T_2 is a p-type transistor. The base of T_1 connects to point B. T_1 would switch on as soon as V_B rises up to the base-emitter threshold voltage of T_1. The base of T_2 will then be connected to the ground. T_2 would switch on once the connection between its base and the ground is established. The storage capacitor begins to discharge after T_2 turns on.

Circuit diagram of the complete design is shown in Figure 6.6. Both T_3 and T_4 are n-type transistors. The operation of T_2 is jointly determined by the states of T_1 and T_4. T_2 stays on if either T_1 or T_4 is on. T_1 will turn off once V_B falls below its base-emitter threshold voltage. Meanwhile, feedback current is being drawn from point O and sent to the collector of T_3. The operation of T_4 is controlled by the state of T_3. The storage capacitor continues to discharge and T_2 stays on until V_A falls below the combined base-emitter voltage of T_3 and T_4. The states of each transistor at different phases of the operation cycle are shown in Table 6.3.

It is very difficult to make a direct measurement of the current that flows through the application load. A small resistance R_4 is added to the circuit in this instance. The output current that flows through the application load is obtained by measuring the voltage across R_4.

Resistors R_{T1}, R_{T3} and R_{T4} are used for limiting the current that flows down the respective branches of the circuit. To ensure majority of the energy released from the storage capacitor is delivered to the application load, R_{T3} needs to be substantially larger than R_{LD}.

The discharging trigger limit (V_H) and the discharging completion limit (V_L) can be altered by adjusting the ratio(s) of the resistors chain. Their values could be configured to suit individual application requirement(s).

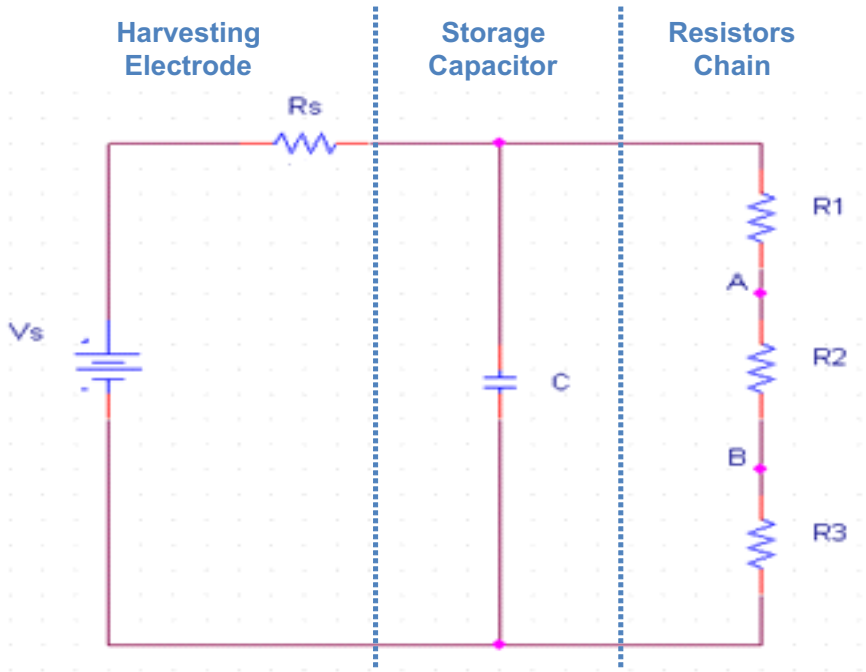

Figure 6.4: The proposed design of an energy buffer circuit - Step 1.

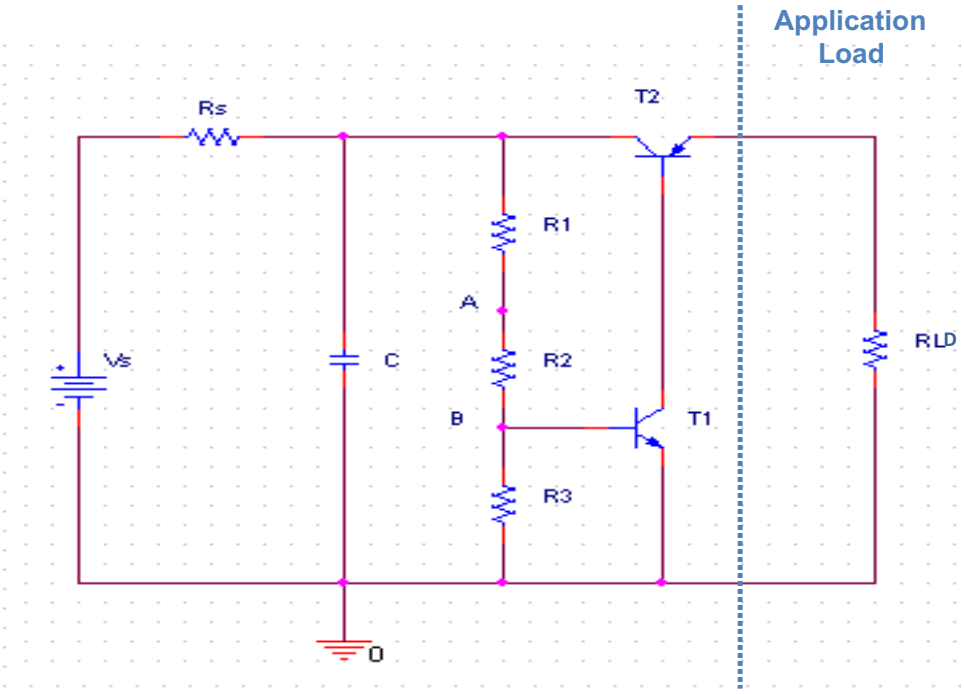

Figure 6.5: The proposed design of an energy buffer circuit - Step 2.

Table 6.3: Operation cycle of the proposed energy buffer.

Time	V_{cap}	T_1	T_2	T_3	T_4	V_A	V_B	V_O	V_D
t_1	$0 \uparrow V_H$	OFF	OFF	OFF*	OFF	$\uparrow 2V_{th}$	$\leq V_{th}$	0	—
t_1/t_2	V_H	ON	ON	ON	ON	$> 2V_{th}$	$= V_{th}$	V_{cap}	0
t_2	$V_H \downarrow V_L$	OFF	ON	ON	ON	$\geq 2V_{th}$	$< V_{th}$	V_{cap}	0
t_2/t_3	V_L	OFF	OFF	OFF	OFF	$< 2V_{th}$	$< V_{th}$	0	—
t_3	V_L	OFF	OFF	OFF	OFF	$< 2V_{th}$	$< V_{th}$	0	—
t_3/t_4	V_L	OFF	OFF	OFF	OFF	$< 2V_{th}$	$< V_{th}$	0	—
t_4	$V_L \uparrow V_H$	OFF	OFF	OFF*	OFF	$\uparrow 2V_{th}$	$\leq V_{th}$	0	—
t_4/t_2	V_H	ON	ON	ON	ON	$> 2V_{th}$	$= V_{th}$	V_{cap}	0

where

- 'V_A' is the voltage at point A, similar notation applies to other points in the circuit diagram.

- 't_1/t_2' represents the moment of transition from t_1 to t_2. Simialr notation applies to other transition moments.

- 'ON' means the transistor in concern is switched on.

- 'OFF' means the transistor in concern is switched off.

- 'OFF*' is specially reserved for T_3. T_3 remains off at the early stage of t_1 but it switches on towards the later stage of t_1. The same phenomenon also occurs during t_4.

- 'V_{th}' is the base-emitter threshold voltage of a n-type transistor.

- '$\uparrow 2V_{th}$' means V_A is rising up during the time intervals of t_1 and t_4 and the final voltage could be more than twice of V_{th}.

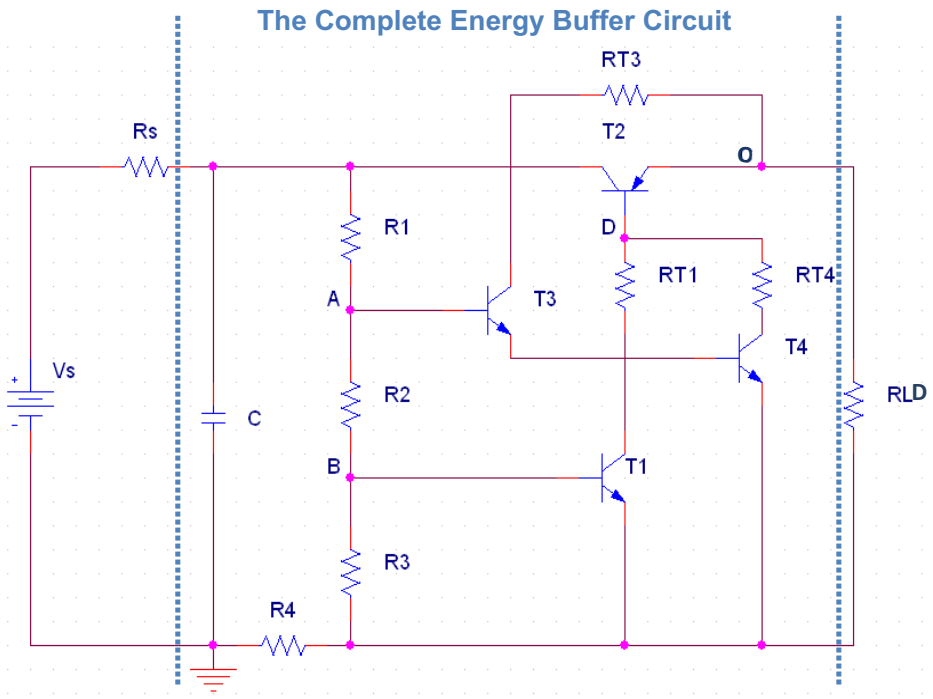

Figure 6.6: The complete design of the proposed energy buffer circuit (Step 3).

6.3.2 Evaluation of the proposed energy buffer through simulation

The simulation circuit of the proposed energy buffer design is shown in Figure 6.7. T_1, T_3 and T_4 are 2N2222 npn transistors. T_2 is a BC327 pnp transistor.

The simulation output waveforms are presented in Figure 6.8. These results suggest that the operation characteristics of the proposed energy buffer are very similar to those commercially available products. The blue solid curve represents the voltage on the storage capacitor (V_{cap}). The storage capacitor keeps charging up until its voltage reaches 3.7 V. The storage capacitor discharges afterwards and the voltage on the storage capacitor starts to drop. The storage capacitor keeps discharging until its voltage falls down to 1.9 V. The storage capacitor starts to charge up again from 1.9 V. The discharging trigger limit and the discharging completion limit are clearly identifiable. The red dashed curve represents the voltage on the application load (V_{LD}). Its existence confirms that current is flowing to the application load during the discharging period.

The current that flows out from the storage capacitor (I_{cap}) and the current

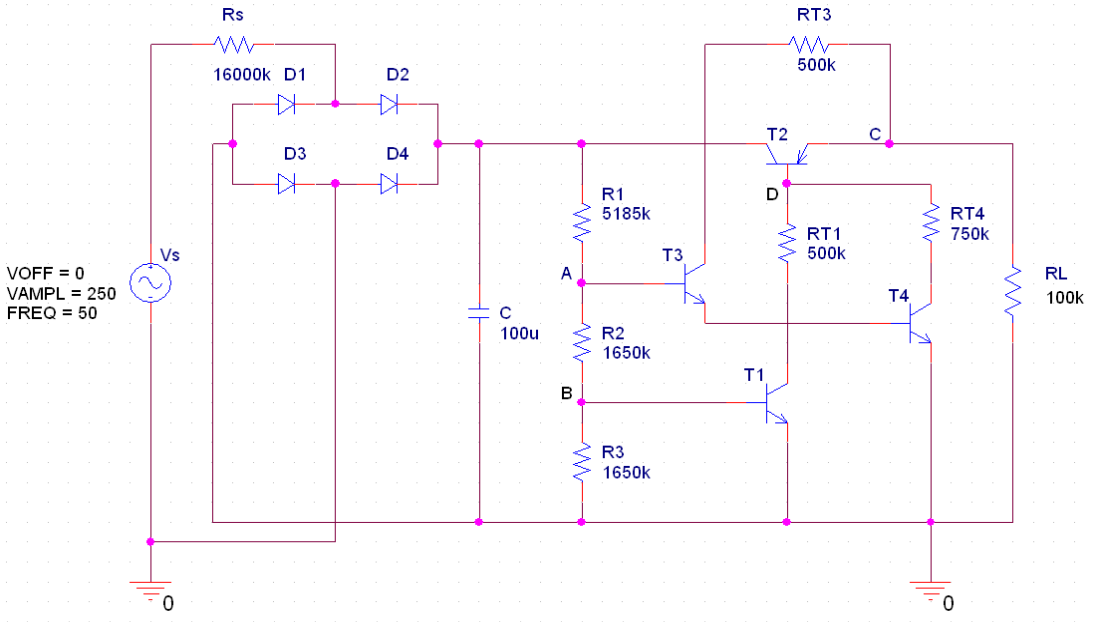

Figure 6.7: Simulation circuit of the proposed energy buffer.

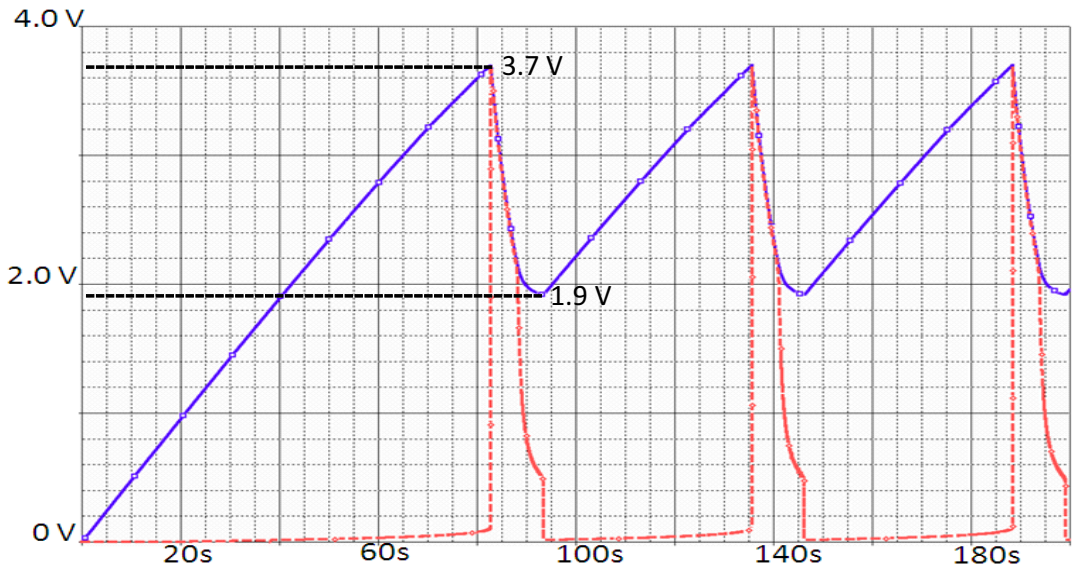

Figure 6.8: Simulation output waveforms of V_{cap} (blue solid curve) and V_{LD} (red dashed curve).

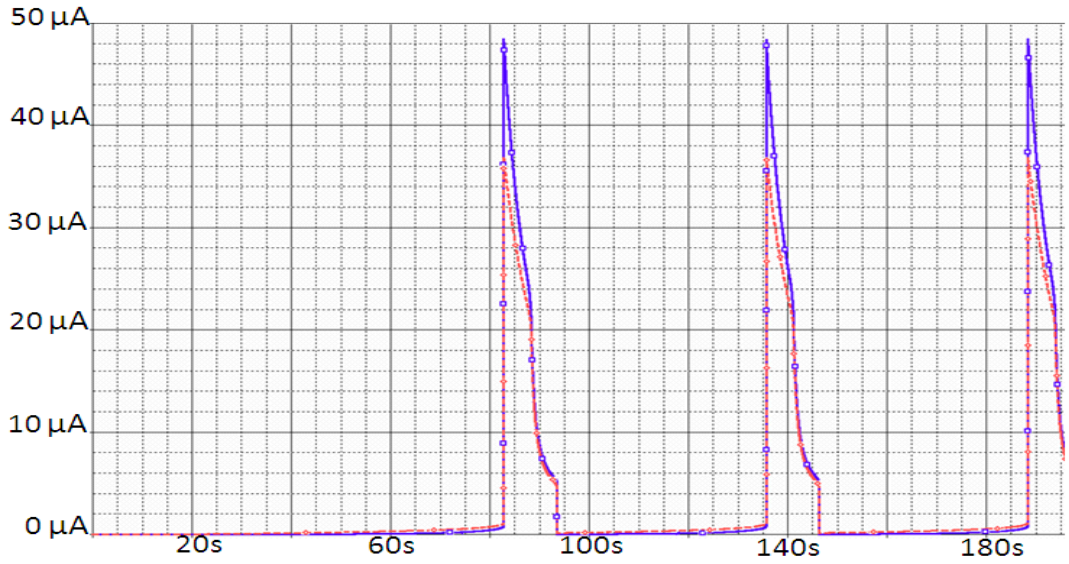

Figure 6.9: The waveforms of I_{cap} (blue solid curve) and I_{LD} (red dashed curve).

that flows through the application load (I_{LD}) are represented by the blue solid curve and the red dashed curve respectively in Figure 6.9. The high degree of overlapping among these two curves indicates that majority of the output energy from the storage capacitor is delivered to the application load.

The amount of energy discharged by the storage capacitor and the amount of energy received by the application load have been derived using the approximate numerical integration method. Multiple data points are sampled from a continuous curve. The sampling interval is Δt. The discrepancy between the sampled data and the actual curve depends on the size of Δt. Small Δt creates small discrepancy and vice versa. The mathematical representation of the approximate numerical integration method in this case is presented by:

$$E = \int_{t_2}^{t_3} V(t)I(t) \approx \sum_{i=0}^{n} P_i \Delta t \tag{6.2}$$

where

$V(t)$ is the voltage function of time

$I(t)$ is the current function of time

P_i is the power at each data sampling point

Δt is the data sampling interval

The simulation outputs of the voltages and currents during the discharging period are shown in Figure 6.10 and Figure 6.11 respectively. The discharging period of the storage capacitor, as marked out in Figure 6.10, lasts 10.6 seconds. Each voltage/current dataset would have at least 106 data points if the sampling interval is 0.1 second (100 ms). Energy is obtained by substituting the corresponding voltage and current datasets into (6.2). The amount of energy discharged from the storage capacitor is approximately 0.696 mJ. The amount of energy received by the application load is estimated to be 0.475 mJ. The overall efficiency of the proposed energy buffer is about 68.2%.

6.3.3 Performance of the proposed energy buffer in laboratory testing

The application load of the energy harvesting device is most likely to be a wireless sensor. Modern wireless sensors, such as MICAz, operate 3 V. MICAz consumes 17.4 mA of current when it is transmitting data at maximum strength [3]. The equivalent application load is in the range of a few hundred Ohms during the discharging period. It is essential to test the performance of the proposed energy buffer design under the circumstance it will typically encounter. Therefore, the application load (R_L) was set to 100 Ω in the laboratory test.

The reduction of the application load impedance will affect the operation of the entire buffer circuit. The resistance in the resistor chains need to be adjusted to keep V_H and V_L constant. The original and updated resistance in the resistors chain are shown in Table 6.4.

Table 6.4: Original and updated component values that keeping V_H and V_L at 3.7 V and 1.9 V respectively.

R_{LD}	C	R_1	R_2	R_3
100 kΩ	68 μF	6 MΩ	2 MΩ	1.5 MΩ
100 Ω	68 μF	2.7 MΩ	2.7 MΩ	3.9 MΩ

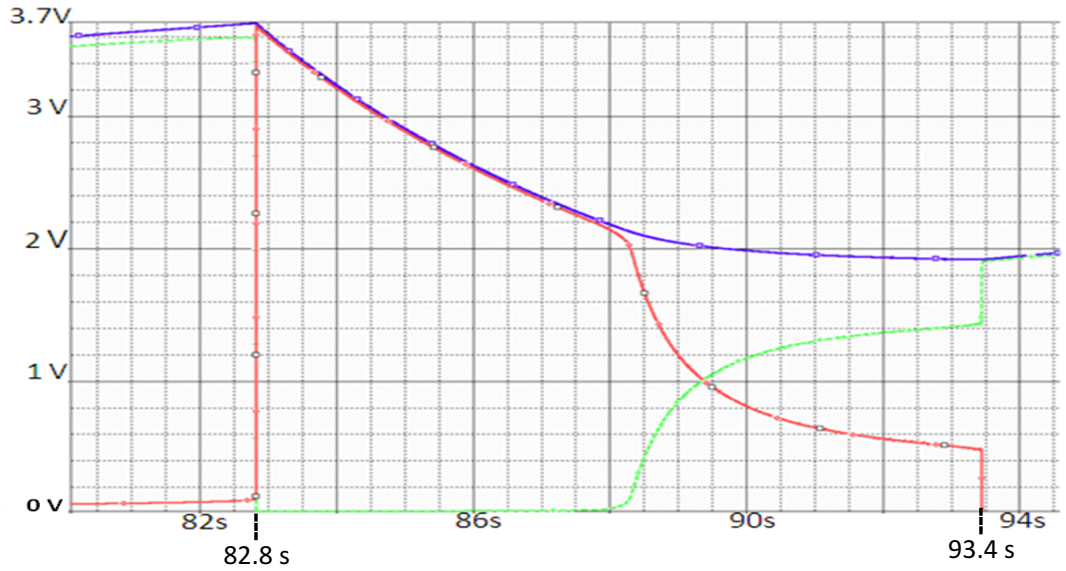

Figure 6.10: Simulation outputs of V_{cap} (blue solid curve), V_{LD} (red solid curve) and V_{cap} - V_{LD} (green dashed curve) during the discharging period.

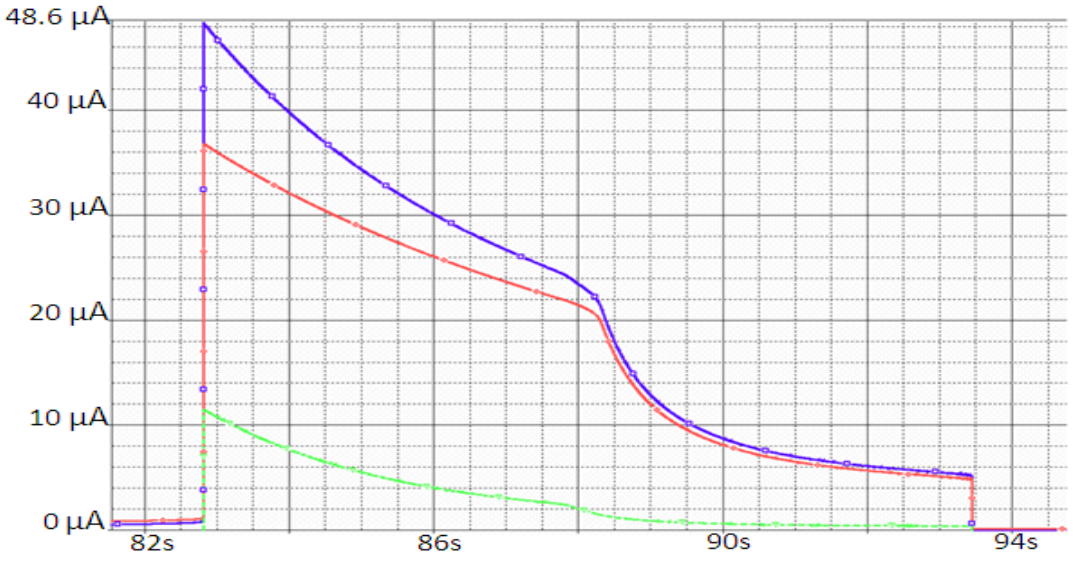

Figure 6.11: Simulation outputs of I_{T2} (blue solid curve), I_{LD} (red solid curve) and I_{T2} - I_{LD} (green dashed curve) during the discharging period.

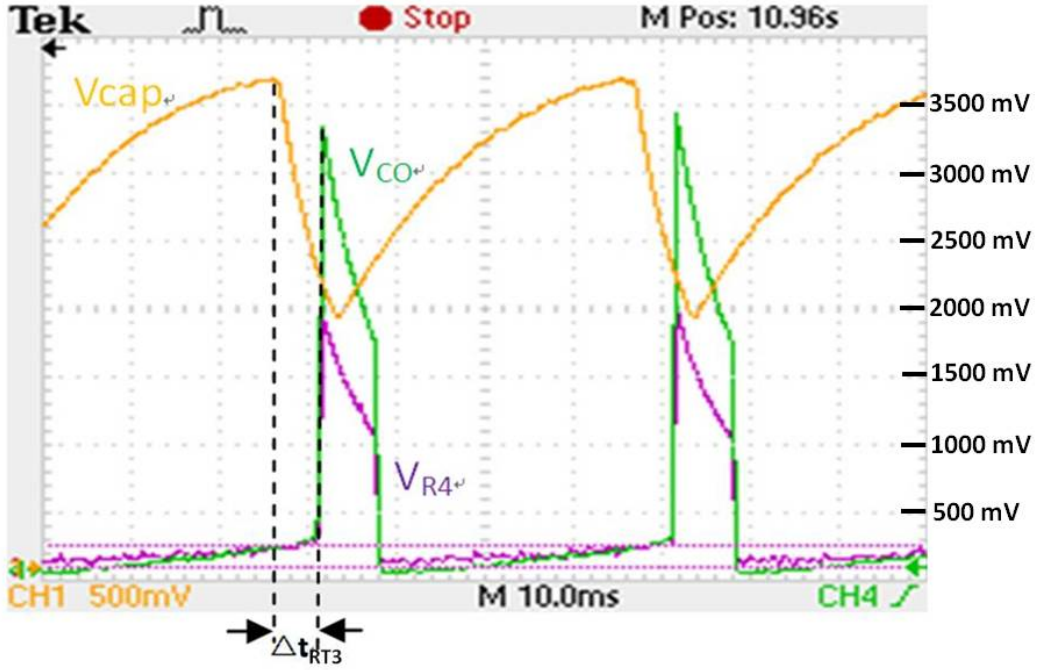

Figure 6.12: Laboratory test results of the energy buffer circuit during the discharging period (R_{LD} = 100 Ω and C = 68 μF): V_{cap} (yellow curve), V_{CO} (green curve) and V_{R4} (purple curve).

A DC power supply is used as the energy source in order to reduce the time it takes to charge up the storage capacitor. The voltage waveforms during the discharging period are shown in Figure 6.12. The voltage across the application load is represented by a green curve (V_{CO}). The voltage across resistor R_4 in Figure 6.6 is represented by a purple curve. Energy is being delivered to the application load. But there is a 5 ms delay (Δt_{RT3}) after T_2 has been switched on. The time delay could be reduced by lowering the overall resistance on the feedback path. However, it would increase the energy consumption and consequently make energy buffer circuit less efficient.

Larger capacitor is able to store and discharge more energy. Capacitors of different types and different sizes, including supercapacitors, have been tested. The smallest supercapacitor currently available on the market is 6800 μF [3]. The self-discharging rate of supercapacitor is much lower than other types of capacitors. This property is especially beneficial if the output from the energy

Table 6.5: Laboratory test performance of the proposed energy buffer.

Storage Capacitor	Discharging Output	Buffer Efficiency	Energy Received
68 μF Electrolytic	0.11 mJ	80%	0.09 mJ
68 μF Tantalum	0.11 mJ	80%	0.09 mJ
680 μF Electrolytic	1.1 mJ	86%	0.95 mJ
680 μF Tantalum	1.1 mJ	87%	0.96 mJ
6800 μF Supercapacitor	11 mJ	87%	9.57 mJ
6800 μF Tantalum	11 mJ	87%	9.57 mJ

source is intermittent. The performance of the energy buffer circuit with different storage capacitors are presented in Table 6.5.

The results suggest the efficiency of the energy buffer is at least 80%. If a MICAz wireless sensor is consuming 17.4 of current, the amount of energy released by a single discharge from a 6800 μF capacitor is able to sustain the MICAs to transmit data for approximately 146 ms. The sensor is able to transmit 3.65 kB of data during the discharging period.

6.3.4 Device integration and possible improvements

Testing the fully assembled experimental harvesting device

The proposed energy buffer circuit performs as expected in stand alone test. Additional tests have been carried out after the energy buffer is integrated into the harvesting device. The application load of the fully assembled experimental harvesting device has a green Light Emitting Diode (LED). The LED gives a visual indication every time the storage capacitor discharges energy.

The full wave bridge rectifier is replaced with a voltage doubler. The circuit diagram of a typical voltage doubler is shown in Figure 6.13. It is not only able to carry out the the AC to DC conversion but also provide a higher output voltage than full wave bridge rectifier. Although the output voltage is increased, the total amount of charge transferred onto the storage capacitor remains the same.

The fully assembled experimental harvesting device is put to the test in the centre of the high voltage test rig. The setup is shown in Figure 6.14. The exper-

imental harvesting device has a 68 μF storage capacitor and a 100 kΩ resistance load. The voltage waveform of the storage capacitor is shown in Figure 6.15.

The storage capacitor starts to discharge energy when the its voltage rises up to 3.32 V. The discharging of energy will continue until the voltage on the storage capacitor falls down to 1.9 V. The discharging period lasts approximately 4 seconds. This figure is obtained by measuring the LED illumination duration. The fully assembled experimental harvesting device behaves as expected.

Improvement opportunities

The components on the feedback path could affect the output of the energy buffer. To eliminate the influence of the feedback circuit to the application load, a diode with low forward bias could be placed between point O and the application load. The anode of the diode connects to point O while the cathode connects to the application load.

Metal oxide semiconductor field effect transistors (MOSFETs) consume less energy than their bipolar counterparts. The efficiency of the energy buffer could be further improved by using MOSFETs instead of bipolar transistors.

A low voltage power switch, which has similar functionality as the energy buffer, is shown in Figure 6.16 [5]. It shares some similarities with the proposed

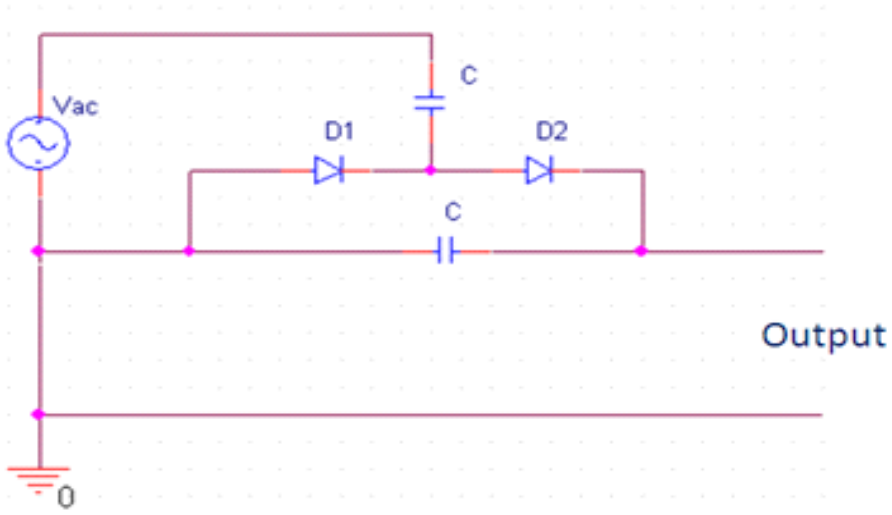

Figure 6.13: Circuit diagram of a typical voltage doubler [4].

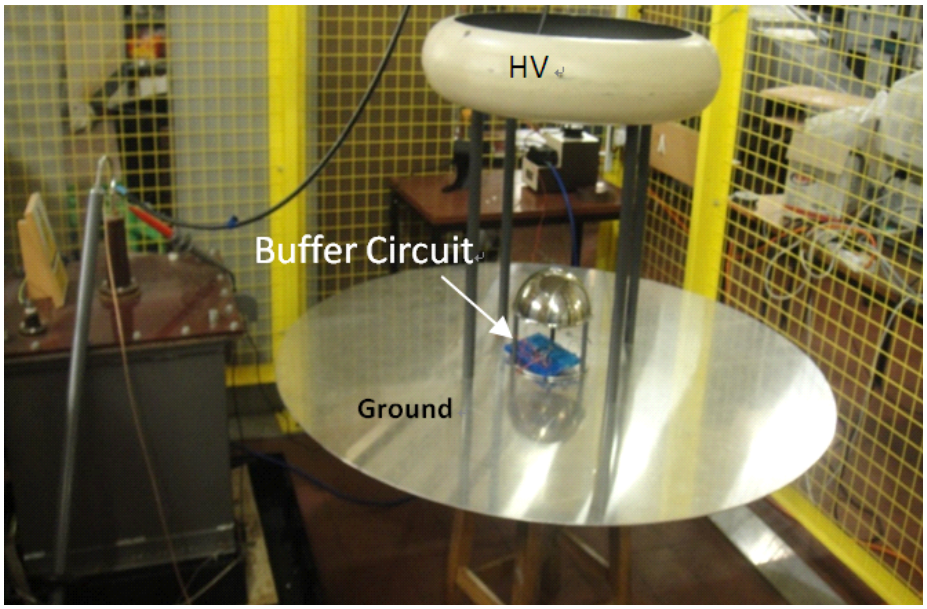

Figure 6.14: The fully assembled harvesting device sits in the centre of the high voltage test rig.

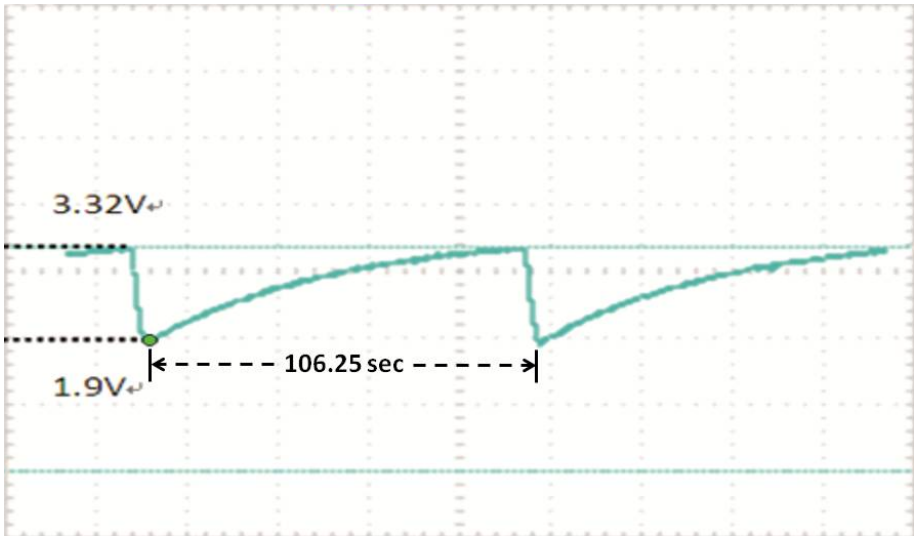

Figure 6.15: Voltage waveform of the 68 μF storage capacitor when the strength of the electric fields around the harvesting device is 30 kV/m.

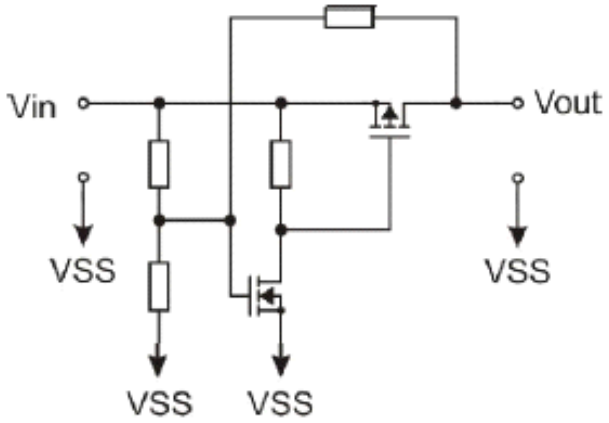

Figure 6.16: Circuit diagram of a 'low voltage power switch' [5].

energy buffer design in this study, but there is still distinguishable difference between the two circuits. The proposed energy buffer is able to adjust the voltage limits while the low voltage power switch shown in Figure 6.16 has no control over the discharging completion limit. The circuit shown in Figure 6.16 also suggests that transistor T_2 in the proposed design may need to swap the connections to its terminals. A conducting channel does exists inside transistor T_2 but maybe not in a state that entirely fits the intended purpose.

6.4 Summary

Both the simulation and laboratory test results indicate the fundamental principle of the proposed energy buffer design is sound. Energy can be accumulated onto the storage capacitor until the voltage across the storage capacitor reaches up to 3.32 V. This is followed by energy discharging. The discharging will not stop until the the voltage across the storage capacitor drops down to 1.9 V. The energy buffer is able to transfer at least 80% of the energy discharged from the storage capacitor to the application load. A relevant study on the energy buffer of harvesting device supports the design philosophy of the proposed energy buffer [5]. It is worthwhile to keep improving the existing design.

To prove harvesting energy from the electric fields is feasible, a demonstration unit has been assembled. The assembly and deployment of the demonstration

unit will be presented in the next chapter.

Bibliography

[1] MICAz datasheet, Wireless Sensor Network, ACEINNA Inc, Massachusetts, USA.

[2] Energy Harvesting Modules Datasheet, Advance Linear Device Inc, California, USA.

[3] 6800 μF Supercapacitor Datasheet, Manufacturer Part No.BZ01KB682ZSB, AVX, South Carolina, USA.

[4] P. Favrat, D. Philippe and M. Declercq. A high-efficiency CMOS voltage doubler, *IEEE Journal of Solid-state Circuits*, Vol.33, No.3, pp. 410-416, 1998, IEEE.

[5] P. Woias. Micro Energy Harvesting - From Basic Research to Practical Application, *Keynote Speech at the Energy Harvesting Network Dissemination Event*, London, UK, March 2012.

Chapter 7

Harvesting application demonstration

7.1 Introduction

The novelty of this study can be demonstrated by harvesting energy from electric fields and supplying the energy to application load(s). A demonstration unit, refer to as the 'demo unit' hereinafter, has been assembled using off-the-shelf components.

7.2 Transient surge protection

The energy harvesting device is eventually going to operate in air-insulated high voltage substations. Transient surge, also know as voltage spike, is one of the most common hazards the harvesting device will encounter. Transient surge can be caused by many events, such as lighting strikes or tripping of circuit breakers. It is often accompanied with a sharp rise of the electric fields. The harvesting device could be damaged by transient surge.

A gas discharging tube (GDT), as shown in Figure 7.1, is installed in parallel with the harvesting circuit to protect it from transient surge. The technical specifications claim it can withstand impulse current of up to 10 kA and impulse voltage of up to 3.5 kV [1]. Transient surge experiment has been conducted to examine the effectiveness of the GDT.

The experimental setup is shown in Figure 7.2. The harvesting device sits in the centre of the test rig. The HV electrode of the test rig is connected to a Marx generator, which is able to generate electrical impulses in the magnitude of hundreds of kilovolts. The strength of the electric fields generated in the centre of the test rig will go through impulse-like rapid change in strength during the test.

Besides connecting to the HV electrode of the test rig, the Marx generator has a separate output connection to a 10:1 resistor chain. The voltage on the smaller part of the resistor chain is measured by a high voltage probe. The high voltage probe further divides the magnitude of its measurand by a factor of 1000. Therefore, the output of the high voltage probe is 1/10,000 of output voltage of the Marx generator.

An oscilloscope is used to measure the output of the high voltage probe. The impulse shown in Figure 7.3 is recorded by the oscilloscope. The output of the Marx generator reaches -158 kV in about 200 ns. The rate of change is approximately 790×10^9 V/s. This is comparable to the transient surge caused by lighting strikes or faults in the grid. Transient surge can occur at any point in the 50 Hz cycle. Damage could be inflicted by impulse of either polarity.

The Marx generator sends out a few impulses which are similar to the one shown in Figure 7.3. These impulses have been applied onto the high voltage electrode while the harvesting device is sitting in the centre of the test rig. The electric fields in the centre of the test rig go through rapid magnitude change a few times.

The performance of the harvesting device prior to and after the impulse test is presented in Table 7.1. Both sets of results are very close to each other. It is reasonable to conclude that no damage has been inflicted on the harvesting device. The GDT is installed in the demo unit to provide protection from transient surge.

7.3 The demo unit

7.3.1 Design and assembly of the demo unit

The demo unit was assembled using off-the-shelf components for ease of manufacturing. It is housed, as shown in Figure 7.4, inside an electrical grade polycarbon-

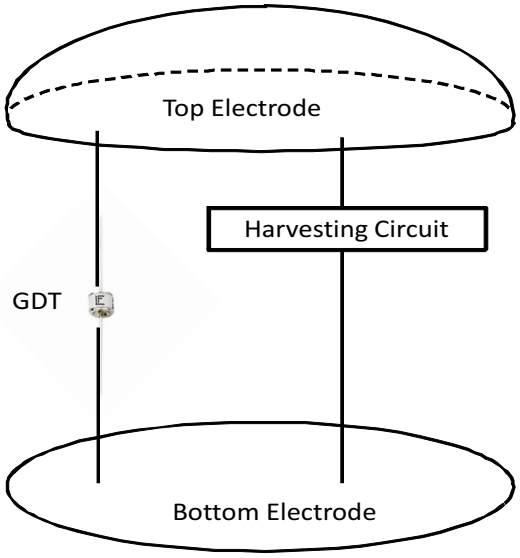

Figure 7.1: A GDT is connected in parallel with the harvesting circuit to provide protection from transient surge.

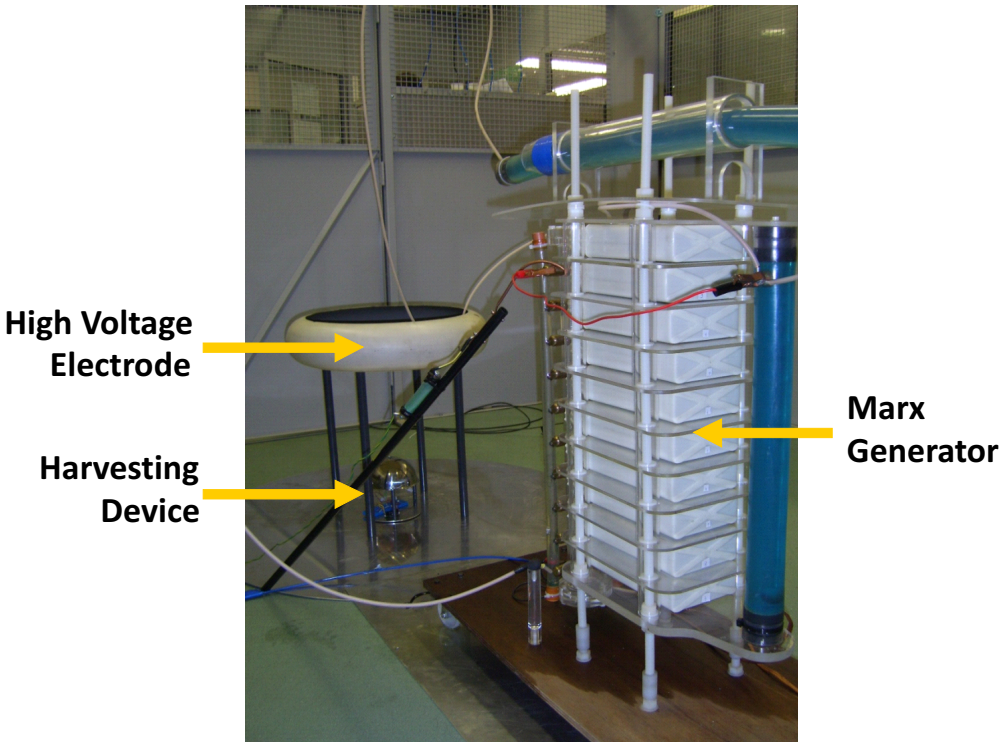

Figure 7.2: Transient surge experimental setup.

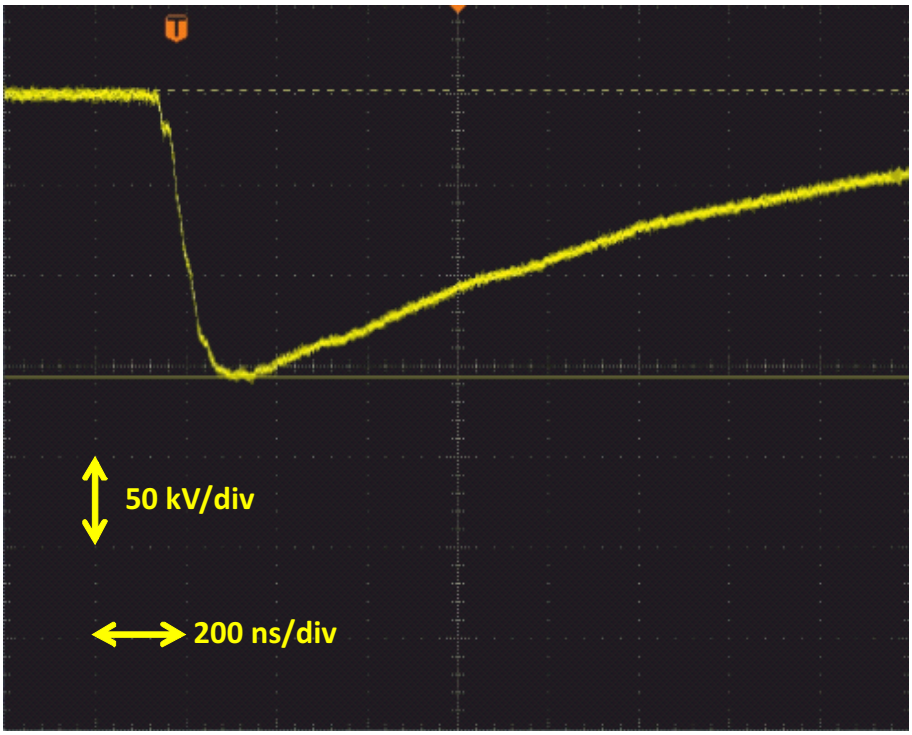

Figure 7.3: Impulse-like output of the Marx generator.

Table 7.1: Performance of the harvesting device before and after the transient surge experiment.

Electric Fields Strength	Time to charge up EH 300A from V_L to V_H	
	Before the impulse test	After the impulse test
20 kV/m	40 min 13 sec	39 min 28 sec
30 kV/m	26 min 53 sec	26 min 01 sec
40 kV/m	20 min 02 sec	19 min 22 sec
50 kV/m	16 min 13 sec	15 min 22 sec
60 kV/m	13 min 50 sec	12 min 48 sec
70 kV/m	11 min 45 sec	11 min 01 sec
80 kV/m	10 min 53 sec	9 min 55 sec
LED illumination period $\approx$ 22 sec		

ate enclosure. A rectangular plane electrode was used rather than a hemispherical electrode.

Rectangular electrode can only interact with the component of the electric fields that is perpendicular to the electrode itself. But it compensates this disadvantage with a large surface area. The surface area of the rectangular electrode is about 0.12 m^2 while the surface area of the hemispherical electrode is 0.05 m^2 [2].

The block diagram of the demo unit is shown in Figure 7.5. The rectangular dashed line box represents the polycarbonate enclosure. The circuit diagram of the demo unit is presented in Figure 7.6. The energy buffer is an EH 301A module. It can store the largest amount of energy among its peers [3]. The output of the EH 301A module is fed into a linear voltage regulator. The output of the linear voltage regulator is influenced by the ratio of the resistors chain:

$$V_O = V_{ref} * (1 + \frac{R_2}{R_1}) + I_{ADJ} * R_2 \tag{7.1}$$

where

V_O is the output voltage of the regulator, V

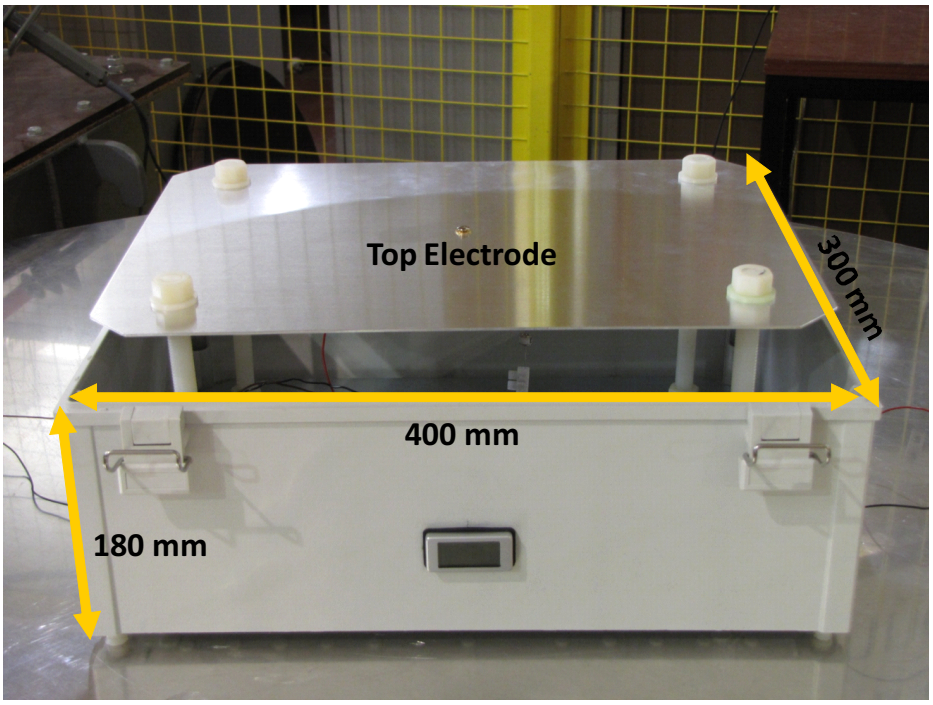

Figure 7.4: Close-up view of the demo unit.

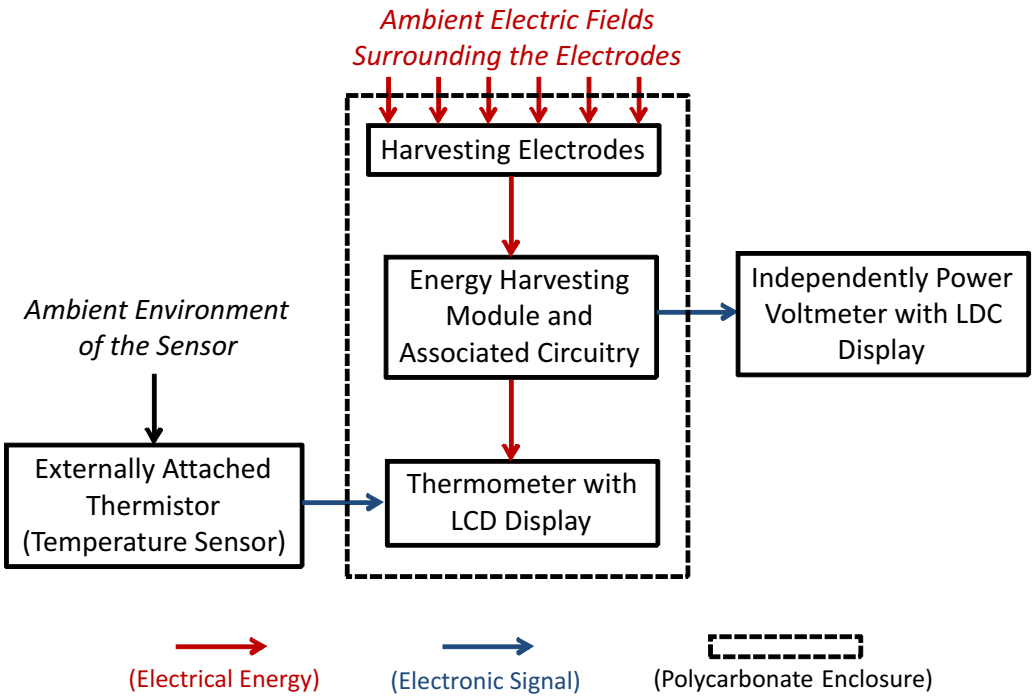

Figure 7.5: Constituent parts of the demo unit with the rectangular dashed line box represents the polycarbonate enclosure.

V_{ref} is the reference voltage between the output pin and the adjust pin of the regulator, typically $V_{REF} = 1.25$ V [4]

R_1 is the resistor between the output pin and the adjustment pin of the voltage regulator, Ω

R_2 is the resistor between the adjustment pin of the voltage regulator and ground, Ω

I_{ADJ} is the current flows out of the adjustment pin of the voltage regulator, typically $I_{ADJ} = 55\mu$A [4]

The voltage across the application load is kept constant at approximately 4 V during the entire discharging period. The circuit connections inside the enclosure are shown in Figure 7.7.

A temperature sensor in the form of a screw threaded thermistor is connected to the demo unit. This thermistor can be attached onto many surfaces with ease. Figure 7.8 shows the thermistor is firmly screwed onto a circular metallic plate.

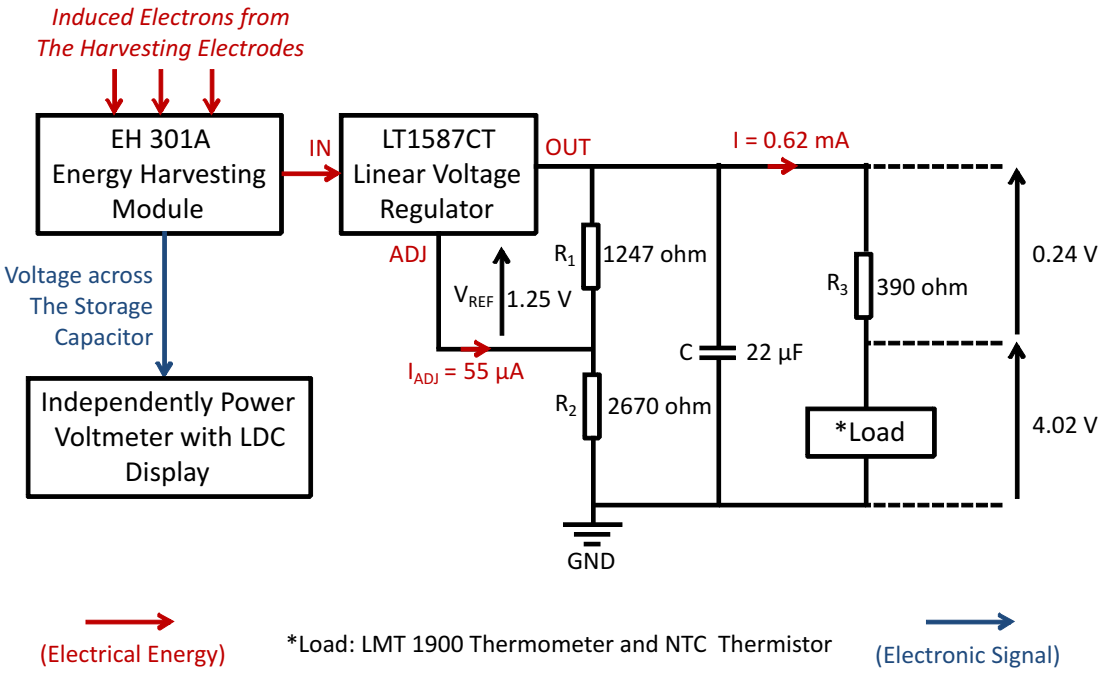

Figure 7.6: Circuit diagram of the demo unit.

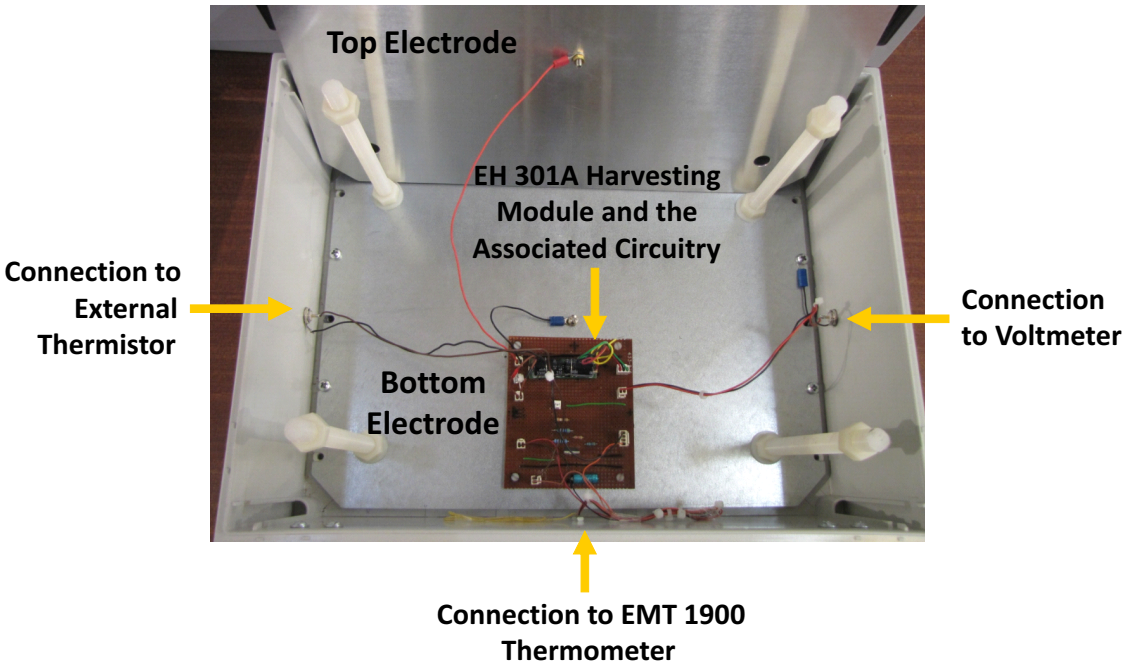

Figure 7.7: Connections inside the polycarbonate enclosure.

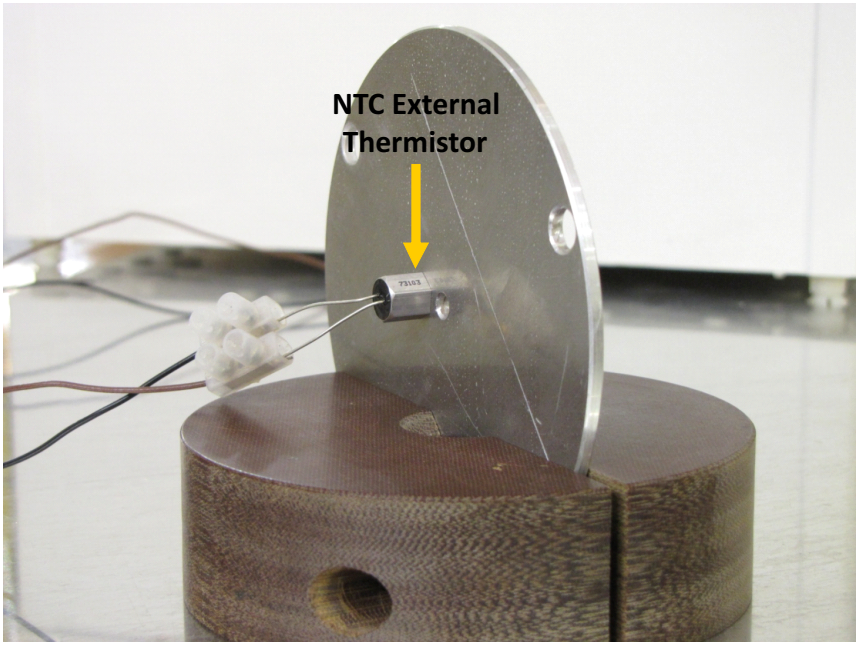

Figure 7.8: Close up view of the thermistor screwed onto a circular metallic plate.

Any temperature change on this plate could be detected by the thermistor. The operation range of the thermistor is between -25 °C and 105 °C [5]. It doesn't need to consume any energy.

The fully assembled demo unit is shown in Figure 7.9. It has an EMT 1900 thermometer fitted onto one of the walls of the polycarbonate enclosure. This thermometer has a liquid crystal display (LCD) screen to display the temperature data either from the internal sensor or the external sensor [6]. It is the application load of the circuit shown in Figure 7.6. The internal sensor of the EMT 1900 thermometer is disabled in this exercise. Its LCD screen will displaying the data from the external thermistor during the discharging period.

The voltage on the storage capacitor of the EH 301A module is measured by an independently powered voltmeter. This voltmeter has extra bright display panel to assist with reading data under challenging conditions [7]. Knowing the voltage on the storage capacitor helps to predict the timing of the energy discharge.

7.3.2 Performance in the laboratory

The experimental setup for testing the demo unit in the in the laboratory is shown in Figure 7.9. The strength of the electric fields increases from 20 kV/m to 80 kV/m.

The results are presented in Table 7.2 and plotted in Figure 7.10. They suggest the time it takes to charge up the storage capacitor and the strength of the electric fields have a linear relationship.

The LCD screen displays the temperature data for about 14 seconds when the module discharges its stored energy. According to Figure 7.6, 0.62 mA of current was flowing through the application load during the discharging period. The amount of energy received by the thermometer in each discharging event is estimated to be 35 mJ.

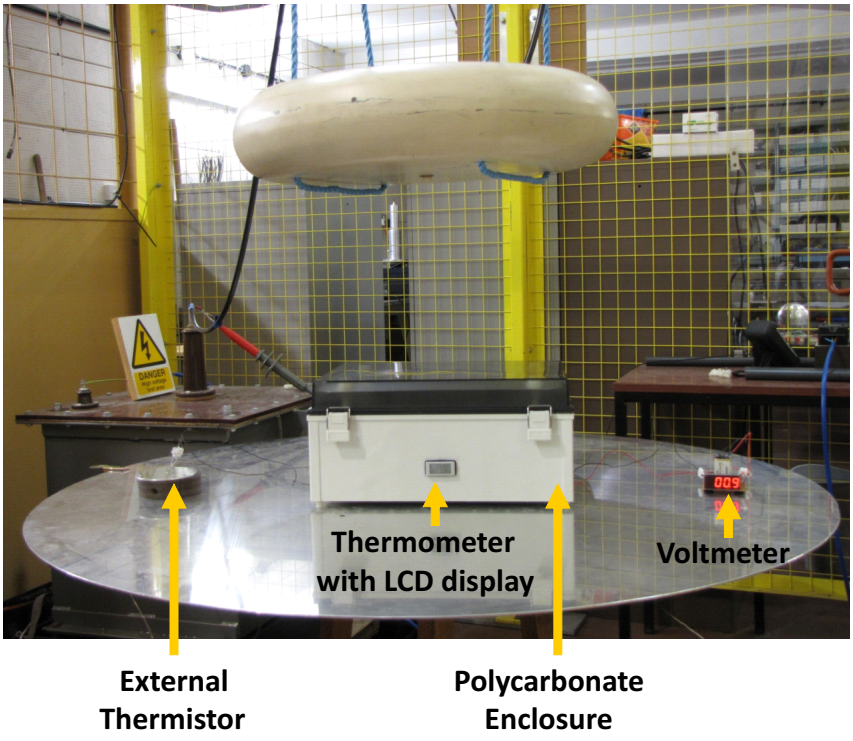

Figure 7.9: Demo unit sits in the centre of the high voltage test rig.

Table 7.2: Performance of the demo unit in the laboratory.

Strength of the electric fields (kV/m)	Length of time for the EH 301A module to be charged up from V_L to V_H (X *min* Y *sec*)
20	49 min 57 sec
30	32 min 42 sec
40	24 min 17 sec
50	19 min 00 sec
60	16 min 17 sec
70	14 min 57 sec
80	12 min 33 sec

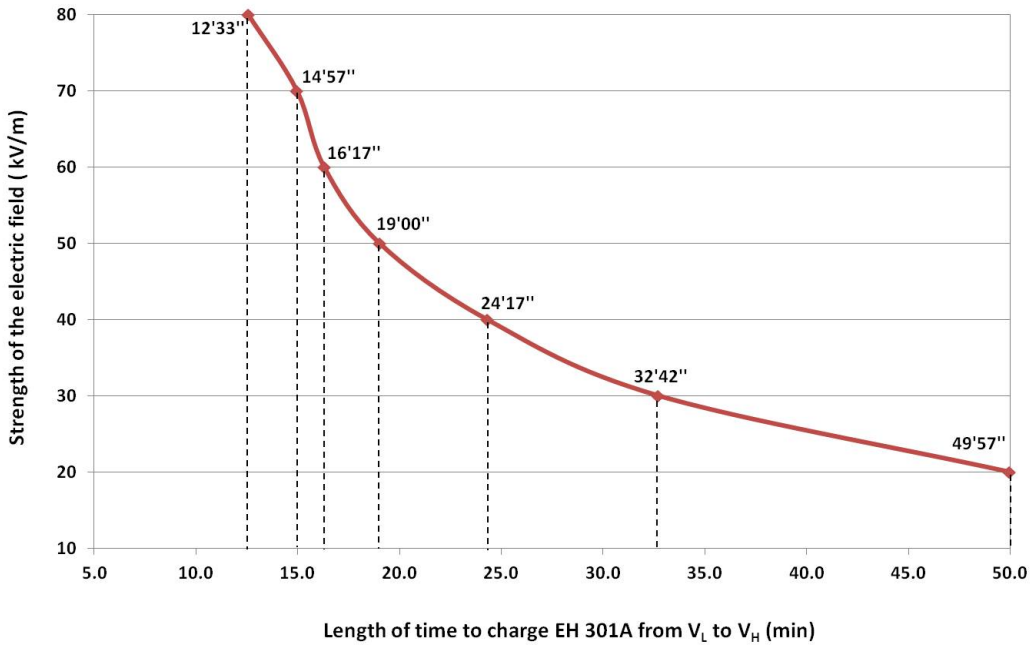

Figure 7.10: Performance of the demo unit in the laboratory.

7.4 Demonstration of harvesting energy in an air-insulated substation

7.4.1 Overview of the substation

The site test was conducted in West George Street substation. It is a 275/33 kV indoor air-insulated substation. This substation is located in the central business district of Glasgow. The external surroundings of the substation is shown in Figure 7.11. The internal view of the substation is shown in Figure 7.12. It is more compact than 400 kV air-insulated substations but the general layout is similar.

The field survey was conducted using the circular field sensor developed in this study. The setup is shown in Figure 7.13. The output of the circular field sensor is measured by a battery-powered oscilloscope.

The survey results presented in Chapter 3 helps to identify locations with strong electric fields. Two of these locations are shown in Figure 7.14. They are on top of the concrete support structure of 275 kV disconnectors, roughly one third of the way between two adjacent phases. Electric fields at these locations are approximately 23 kV/m.

7.4.2 Performance of the demo unit

The setup of the demo unit in the substation is shown in Figure 7.15. Gaining access to the demo unit is easier than anticipated. The independently powered voltmeter is replaced by a typical digital multimeter. Digital multimeters generally make more accurate measurement than stand alone voltmeters.

The demo unit was placed in a few locations in the substation. One of these locations, as shown in Figure 7.16, is on top of the concrete support structure of 275 kV disconnectors. This location is between the yellow and red phases, one third of the way from the yellow phase and two third of the way from the red phase. It takes approximately 45 minutes to charge up the storage capacitor of the EH 301A module from the discharging completion limit (V_L) to the discharging trigger limit (V_H). This is similar to the test result obtained in the laboratory.

Temperature data from an external thermistor, as shown in Figure 7.17, was

Figure 7.11: External view of the West George Street indoor substation.

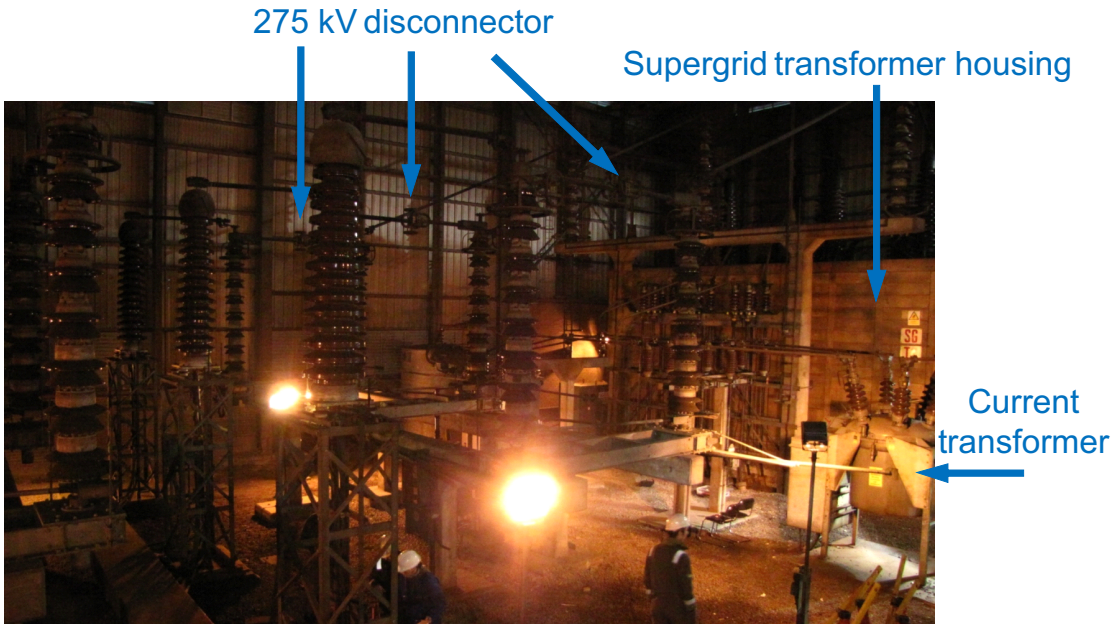

Figure 7.12: Internal view of the West George Street indoor substation.

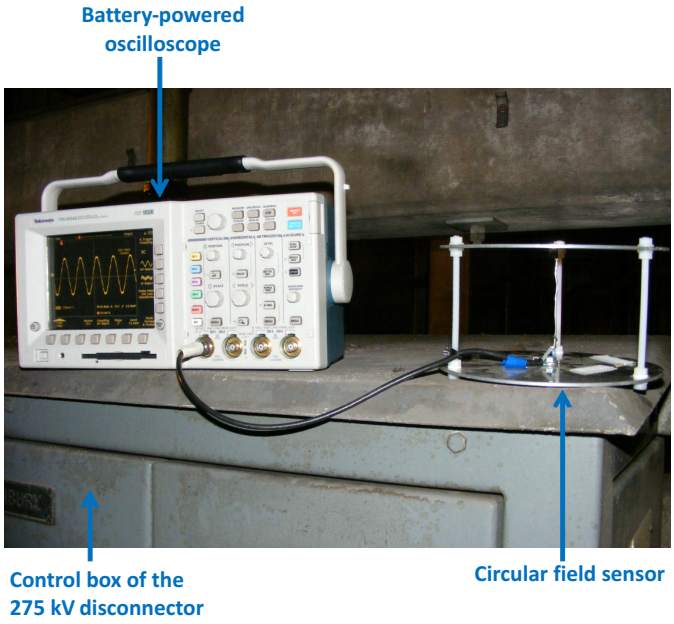

Figure 7.13: Substation field survey setup.

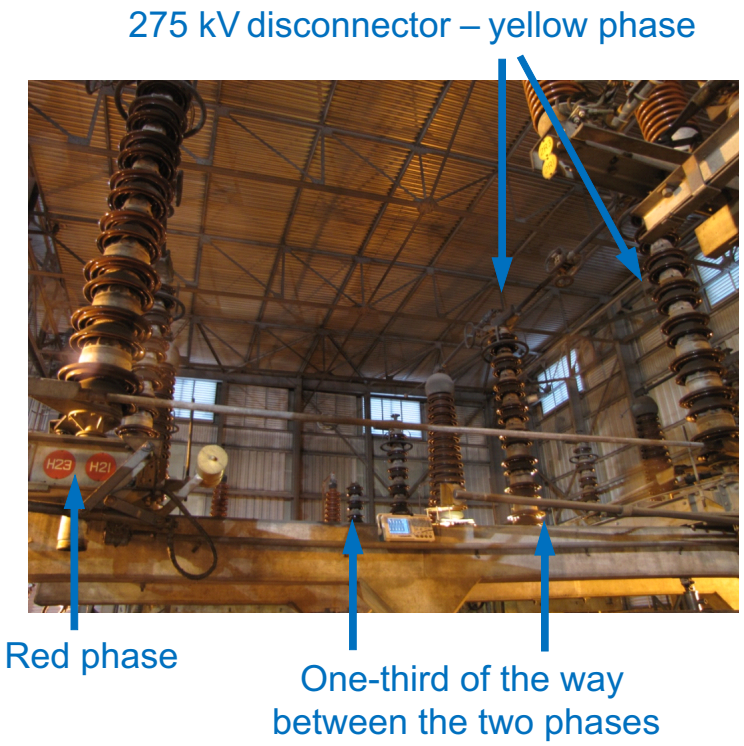

Figure 7.14: Measuring the electrical fields on top of the concrete support structure of 275 kV disconnectors.

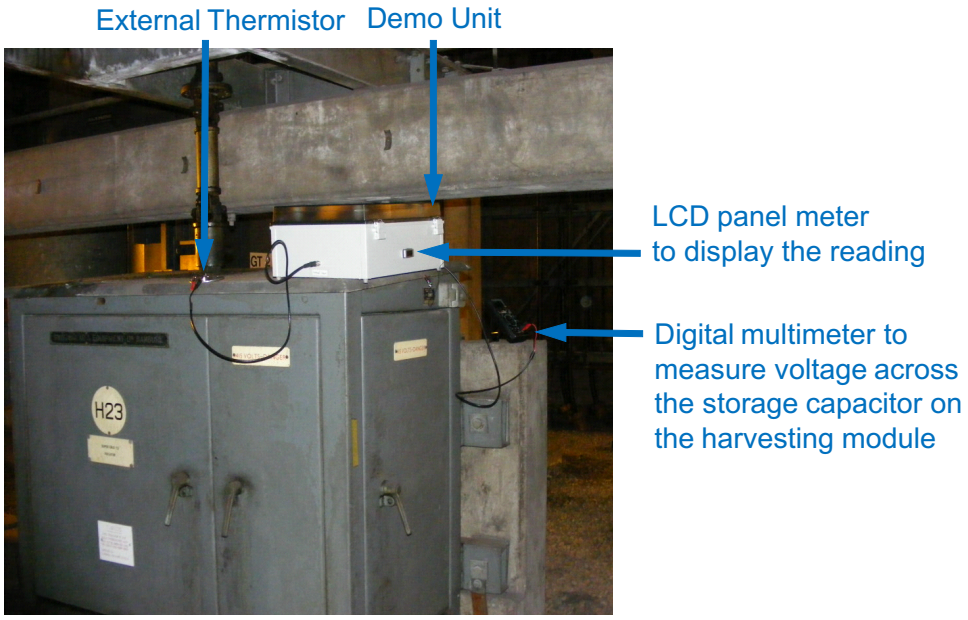

Figure 7.15: Setup of the demo unit in the substation.

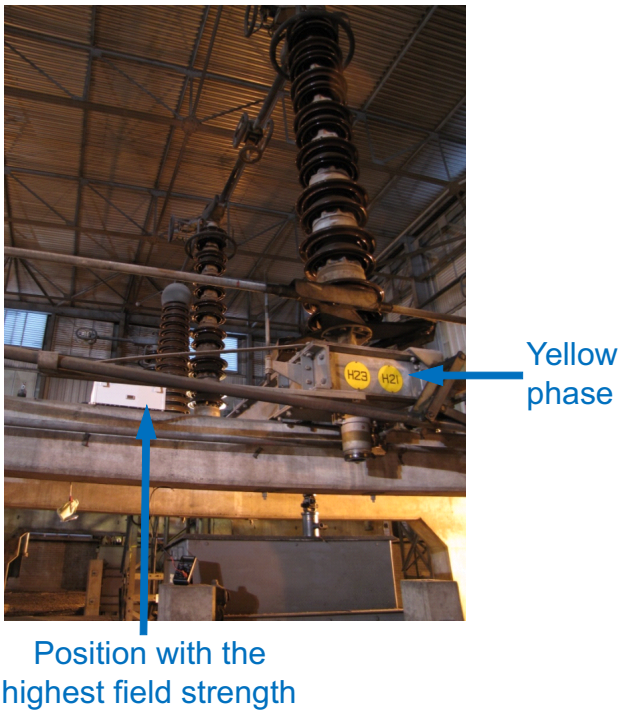

Figure 7.16: The demo unit sits in one of the locations that has the strongest field strength underneath 275 kV disconnectors.

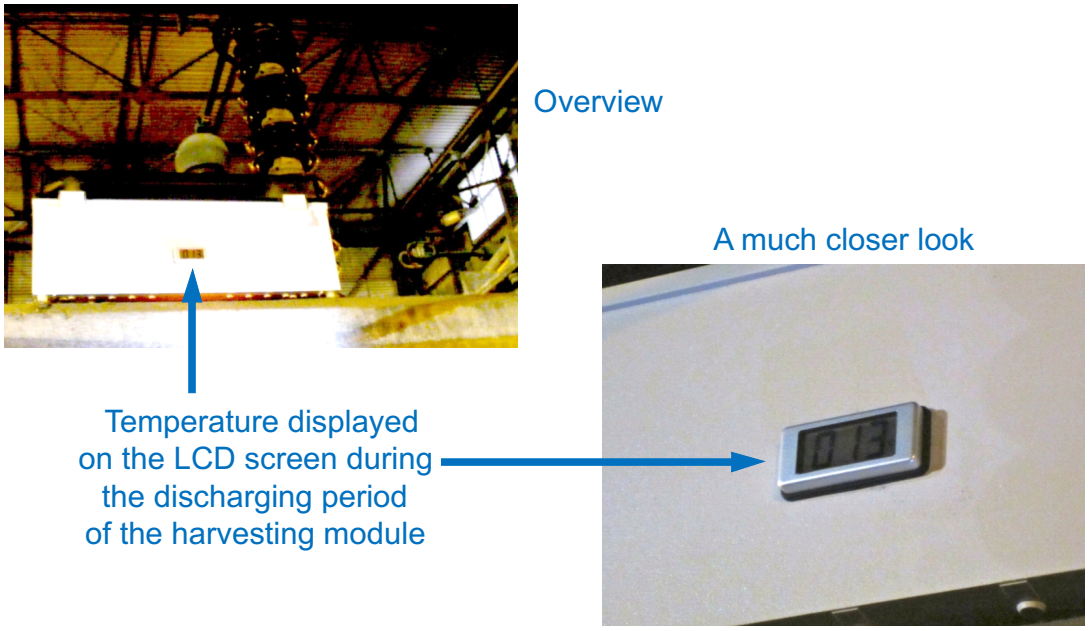

Figure 7.17: Temperature data from the external thermistor (13 °C) being displayed on the LCD screen.

displayed on the LCD panel for about 14 seconds when energy is being discharged from the storage capacitor of the EH 301A module.

The demo unit performs as expected when it was deployed in the substation. It is capable of harvesting energy from the surrounding electric fields and discharging energy to the application load. Although the site test can only be conducted in unrestricted area of the substation, the linear relationship between the performance of the demo unit and the strength of the electric fields makes it straight forward to estimate the the performance of the demo unit in restricted area of the substation.

The site test confirms that harvesting energy from the electric fields inside air-insulated substations has the potential to solve the problem of limited battery capacity.

7.4.3 Efficiency estimate

The demo unit has a plane-shaped harvesting electrode. According to the simulation result shown in Table 4.2, approximately 0.031 nC of charge can be induced

on every square centimeter of the plane-shaped harvesting electrode when the field strength is 10 kV/m. The graphs in Figure 4.15 establish that the amount of induced charge on an electrode is proportional to the field strength. The demo unit was placed in a location shown in Figure 7.16. The measured field strength at this location is 23 kV/m. It is reasonable to assume 0.713 nC of charge would be induced on every square centimeter of the harvesting electrode. The harvesting electrode of the demo unit has a surface area of almost 1200 cm^2. Therefore, 855.6 nC of charge could be induced on its surface.

Synchronised switching harvesting on inductor has proven to be the most efficient charge transfer technique. It is able to transfer the entire amount of induced charge twice during each mains frequency cycle. The maximum amount of induced charge that could be transferred from the harvesting electrode to the storage capacitor, in theory, is 115.506 mC after 45 minutes of operation. The overall size of the storage capacitor bank on the EH 301A module is 6.6 mF [3]. Disregarding the voltage limit of the storage capacitor, the amount of energy that could be accumulated on the storage capacitor at this point is approximately 1010 mJ. According to Table 5.5, 1 minute of switching operation consumes about 0.6 mJ of energy. The net amount of energy would be 983 mJ.

The maximum amount of energy that can actually be stored on the harvesting module is slightly above 89 mJ. The demo unit uses linear circuit to transfer the induced charge from the harvesting electrode to the storage capacitor. The efficiency of the linear conversion arrangement is about 9%. Since the efficiency of linear conversion is approximately 9% of the theoretical maximum, therefore the SSHI technique is estimated to be 10 times more efficient than the linear conversion arrangement. The amount of energy received by the application load of the demo unit is 35 mJ. The overall efficiency of the demo unit is approximately 3.5%.

Such a low percentage figure suggests the demo unit is not very efficient. However, wireless sensors are likely to be installed in hard-to-reach locations in many prospective applications. The overall cost of supplying energy to these sensors, such as through battery maintenance, could be prohibitively high. Harvesting energy from the ambient environment ensures the continuous operation of these sensors. Otherwise, the sensors will stop working after their batteries have been depleted. The availability of energy is paramount, it trumps everything else in

these scenarios.

Bibliography

[1] Gas Discharging Tubes AC and CG3 Datasheet, Manufacturer Part No. CG32.5L, Littelfuse, Illinois, USA.

[2] CABPC403018T Polycarbonate Enclosure Datasheet, Manufacturer Part No. CABPC403018T, Fibox, Stockton-on-Tees, UK.

[3] Energy Harvesting Modules, Advance Linear Device, Inc. Available [Online] http://www.aldinc.com/ald_energyharvesting.php, accessed at November 2017.

[4] LT1587CT Adjustable Linear Voltage Regulator Datasheet, Manufacturer Part No. LT1585CT-3.3, Linear Technology Corporation, California, USA.

[5] NTCASCWE3 NTC Thermistors/Screw Threaded Sensors Datasheet, Vishay Intertechnology, Pennsylvania, USA.

[6] EMT 1900 Single Hole Mounting Thermometer Datasheet, Lascar Electronics Ltd, Wiltshire, UK.

[7] DMS-30DR-2-R-C Stand Alone Voltmeter, Murata Power Solutions, Massachusetts, USA.

Chapter 8

Conclusion

8.1 Major findings

Major findings discovered from this study are summarised below:

- There are numerous readily accessible locations inside air-insulated substations which the strength of the electric fields is above 20 kV/m. A simple harvesting device is able to scavenge a few tens of millijoules of energy at these locations within an hour.

- Energy buffer plays a pivotal role in the operation of the harvesting device. Initial test of the purposefully designed buffer circuit shows promising signs. The overall efficiency of the circuit is approximately 68 %, it is worthwhile to pursue further improvements.

- Hemispherical electrode has no sharp edge and therefore minimises partial discharge from occurring. It is able to induce the largest amount of charge among all the shapes that have been investigated if the radius and/or height of the electrodes are identical. It can induce approximately 7% more charges than frustum of cone, the second most efficient shape.

- A harvesting device that using the SSHI technique has the potential to transfer as much as 10 times the amount of induced charge than a harvesting device, identical in dimension, using the linear conversion arrangement.

8.2 Advantages of harvesting energy from electric fields

Both the operation voltage and frequency of an electricity grid are rigorously controlled. They fluctuate very little during normal operation. The strength of the electric fields at a given location inside an air-insulated substation does not vary over time. Except during an outage, the energy contained within electric fields is always available to be harvested.

The field surveys conducted in this study show that the strength of electric fields in many locations is in the region of a few tens of kilovolt per meter (kV/m). These locations are in the unrestricted area of a substation. They are outside the statutory safety clearance range. Gaining access to these locations doesn't require outage. Installing harvesting devices in these locations has little impact to the normal operation of the grid.

8.3 Harvesting efficiency improvement

This study has found that, for a given set of dimensions, hemispherical shaped electrode has the maximum surface area among all the shapes that have been investigated. It is able to interact with electric fields in all directions and induced the maximum amount of charge. In addition, hemispherical shaped electrode does not have any sharp stress-rising edges. It greatly reduces the risk of flash over and/or partial discharging from occurring.

Any energy source that is based on electrostatic induction principle would have output impedance in the region of a few hundred mega ohms if it is operated under mains frequency.

The loading effect caused by the high output impedance will prevent a substantial proportion of the energy to be delivered to the load. Separating the source and the load allows charge induction to take place unvexed on the harvesting electrode. Maximum possible amount of charge would be induced on the electrode at the peaks and troughs of the mains supply voltage. Each switching operation that establishes the connection between the source and the load, however brief, consumes energy. Synchronising the switching operations with the

peaks and troughes of the mains supply voltage is able to transfer the maximum amount of induced from the harvesting electrode minimise the total amount of energy consumed by the switching operations.

Fast switching generates short pulses. Inductor has the ability to smooth out these pulses. It has been proven that placing an inductor before the storage capacitor could mitigate the disadvantage of short pulses and improve the harvesting efficiency further.

8.4 Energy storage and discharge

Modern wireless sensors consume little energy when they are in idle or sleep mode. Energy intensive activity typically lasts a few tens of milliseconds but the power demand is much higher than the average output of a harvesting device.

An energy buffer circuit has been designed to manage the accumulation and discharging of energy on the storage capacitor of a harvesting device. It will not allow any energy to be discharged until the amount of energy on the storage capacitor has reached a certain level. The amount of energy released each time is only a proportion of the energy stored on the capacitor. The energy buffer presented in this study is able to meet the design objective but there is room for improvement.

Chapter 9

Future Work

A major hurdle that prevents the large scale installation of wireless condition monitoring sensors in the electricity grid is the high cost of battery maintenance. This study has demonstrated that harvesting energy from the electric fields has the potential to reduce or even eliminate the cost of battery maintenance. Although harvesting energy from electric fields has been demonstrated, more work needs to be done to make the concept into practical application.

9.1 Survey the electric fields inside the statutory safety clearance range

The field surveys presented this study have only been conducted in locations outside the statutory safety clearance space. Judging from the existing survey results, it is certain that there are many locations inside the statutory safety clearance area would have field strength in the region of a few tens of kilovolts per meter or even higher. These locations are favourable for harvesting energy from the electric fields. However, gaining access to these locations is highly problematic. Planning an outage is very troublesome for the grid operator. Instead of conducting physical surveys, the investigation can be carried out by simulation. A large amount of computing power would be required if the simulation model become more complex. Nevertheless, it is still highly beneficial to identify suitable harvesting opportunities inside the statutory safety clearance range.

9.2 Energy-efficient synchronised switching

This study has proven that synchronising the charge transfer with the peaks and troughs of the mains voltage frequency would improve the harvesting efficiency by as much as 10 times. The synchronisation control circuit presented in this study is only designed for validating concept. Switching operations consume energy. To fully justify the use of synchronised switching, the amount of energy consumed by the switching operations has to be less than the amount of additional energy it helps to harvest.

Advances in technology are continuously reducing the energy consumption of electronic components. Designing a circuit that is able to implement energy-efficient synchronised switching is feasible and worthwhile to be pursued.

9.3 Improve the energy buffer circuit

The energy buffer presented in this study has an efficiency of approximately 68%. The design can be further improved. Improvement opportunities include, but are not exclusive to, rearranging the connection of the p-type transistor on the charge transfer path, putting a diode between the energy buffer output and the application load and replacing as much components as possible with MOSFETs.

These improvements, once fully implemented, would help the energy buffer to consume less energy and run stably. Larger proportion of the harvested energy can be delivered to the application load.

9.4 Demonstrate energy harvesting under challenging weather conditions

The site test in this study was conducted in an indoor air-insulated substation. The demonstration unit is sheltered from natural elements, such as rain and snow. Harvesting devices installed at outdoor substations are more than likely to encounter server weather conditions. The high permittivity of water may affect the electric fields. To examine the impact of severe weather conditions on the harvesting operation, it would be highly beneficial to test the demo unit in an

outdoor substation for a long period of time, especially during the winter months.